Technical University of Denmark

DTU

Nonlinear Fourier transform for dual-polarization optical communication system

Gaiarin, Simone

Publication date:
2018

Document Version
Publisher's PDF, also known as Version of record

Link back to DTU Orbit

DTU Library
Technical Information Center of Denmark

DTU Fotonik
Department of Photonics Engineering

Nonlinear Fourier transform for dual-polarization optical communication systems

Simone Gaiarin

Kongens Lyngby 2018

Abstract

New services and applications are causing an exponential increase in the internet traffic. In a few years, the current fiber-optic communication system infrastructure will not be able to meet this demand because fiber nonlinearity dramatically limits the information transmission rate. Eigenvalue communication is considered an emerging paradigm in fiber-optic communications that could potentially overcome these limitations. It relies on a mathematical technique called "inverse scattering transform" or "nonlinear Fourier transform (NFT)" to exploit the "hidden" linearity of the nonlinear Schrödinger equation as the master model for signal propagation in an optical fiber. One of the rapidly evolving NFT-based communication techniques is called nonlinear frequency division multiplexing (NFDM). Being still in its infancy, NFDM systems still have some practical limitations. One of these limitations is the lack of polarization division multiplexing.

This thesis addresses this problem by introducing the novel concept of dual-polarization NFDM. First, the structure of a single polarization NFDM system using the discrete nonlinear spectrum is described. The particular design aspects of this system are then discussed in details. Afterwards, the theoretical tools that define the NFT for the Manakov system, which describes the evolution of a dual polarization signal in a single-mode fiber, are presented. Using these tools the discrete NFDM system is extended to the dual polarization case. Finally, the results of the first experimental transmission of a dual polarization NFDM system are presented. A transmission of up to $373.5\,\mathrm{km}$ with bit error rate smaller than the hard-decision forward error correction threshold has been achieved.

The results presented demonstrate that dual-polarization NFT can work in practice and that it enables an increased spectral efficiency in NFT-based communication systems, which are currently based on single polarization channels.

Resumé

Nye services og applikationer bevirker en eksponentiel stigning i internet trafikken. Inden for få år vil den nuværende infrastruktur af optisk kommunikations systemer ikke kunne imødegå dette behov idet ikke-linearitet i fiberen vil lægge en afgørende begrænsning på den sendte informationsmængden. Egenværdi kommunikation bliver betragtet som et kommende paradigme skift som potentielt kan overvinde disse begrænsninger. Egenværdi kommunikation baseres på den matematiske disciplin inverteret sprednings transformation også kaldet den ikke-lineære Fourier transformation (NFT) der udnytter den skjulte linearitet i den ikke-lineære Schrödinger ligning der er den primære model som beskriver signal udbredelse i en optisk fiber. En af de hastigt opstået NFT baserede kommunikations teknikker er den ikke-lineære frekvens sammenfletning (NFDM). Denne teknik er stadigvæk i sin spæde start og NFDM er stadigvæk udfordret af nogle praktiske begrænsninger. En af disse begrænsninger er den manglende mulighed for polarisations sammenfletning.

Denne afhandling adresserer dette problem ved at introducere et nyudviklet dobbelt polarisation NFDM. First bliver strukturen af et NFDM system baseret på det diskrete ikke-lineære spektrum beskrevet. Særegne design aspekter af dette system bliver derefter detaljeret diskuteret. Efterfølgende bliver de teoretiske værktøj der beskriver Manakov NFT systemer som inkluderer udbredelsen af signaler repræsenteret i begge polarisationer præsenteret. Ved at benytte disse værktøjer kan det diskrete NFDM system blive udvidet til at inkludere dobbelt polarisations udbredelse. Afslutningsvis bliver de første eksperimentelle resultater af transmission af dobbelt polarisation NFDM signaler præsenteret. Transmission op til 373.5 km med bit fejlrate under harddecision fremadrettet fejlkorrektions tærsklen er blevet demonstreret.

De opnåede resultater understreger at dobbelt polarisations NFT kan benyttes i praksis og således kan øge spektraltætheden i NFT baseret kommunikations systemer, der på nuværende tidspunkt benytter enkelt polarisations kanaler.

Preface

The work presented in this thesis was carried out as a part of my Ph.D. project in the period November 1$^{\text{st}}$, 2014 to February 15$^{\text{th}}$, 2018. The work took place at DTU Fotonik (Technical University of Denmark, Department of Photonics Engineering). The following visiting stays were also part of the Ph.D. project: one month at University College London, London, UK; two months at VPI Photonics GmbH, Berlin, Germany; two months at RISE Acreo, Kista, Sweden.

Acknowledgements

First I would like to thank my supervisor Darko Zibar for his guidance and for giving me the opportunity to pursue this Ph.D.

I would like to thank my examiners Prof. Sergei Turitsyn (Aston University, UK), Prof. Sander Wahls (Delft University, Netherlands) and Prof. Jesper Mørk (DTU Fotonik, Denmark) for taking the time to read and evaluate this thesis.

I would like to thank the Technical University of Denmark and the H2020 Marie Skłodowska-Curie Actions (MSCA) grant number 608099 for the support to this Ph.D. project, which allowed me to participate in several international conferences and multiple external research stays.

I also would like to thank the people I had the pleasure of meeting during my three external research stays: Prof. Polina Bayvel and Prof. Seb Savory for welcoming me at University College London, and Alex and Nikita for helping me bootstrap my research on the nonlinear Fourier transform. Dr. Andre Richter and Dr. Hadrien Louchet for the visit at VPI Photonics, and Nuno for his great support while I was learning the VPI simulation software. Prof. Sergei Popov and Prof. Gunnar Jacobsen for hosting me in Acreo, and Oskars and Xiaodan for the great help they gave me and for boosting my motivation during the middle phase of my Ph.D.

I would like to thank all the present and past colleagues of the High-Speed Optical Communication Group at DTU Fotonik for the fun of these years. Thanks to the DSP cowboys Rasmus, Jűlio, and Edson for sharing with me not only the office but also this Ph.D. journey that made us grew together. Davide Bacco deserves a special thanks for being a real friend, and also because he constantly motivated me during the writing of the thesis. Franceso Da Ros undoubtedly deserves all my gratitude for being a reference point and for the exceptional advices he gave me, which helped me throughout my whole Ph.D., and togheter with Edson for teaching me the wonders of the optical lab. Thanks also to Molly for being a mentor at the beginning of my Ph.D., and Robert for the amusing time together during the long days spent in the lab.

Thanks to Anders for the help with the translations in Danish, and to Lisbeth for the many moments of great fun and for our morning coffee chats.

Thanks to all the ICONE people, and in particular to my friends Auro, Giuseppe, Francesca, Asif, Jaime, Adytia, Tu, Ksenia, Marti, Aleksandrs, Faruk, Hugo, Hou-Man, and Oskars who made this Ph.D. a special experience and with whom I shared many moments of fun. A special thanks goes to Auro for the stimulating discussions, for his contagious enthusiasm for the scientific research that affected me positively, and for his contribution in the realization of a core part of the work in this thesis.

Thanks to my friends Marie and Gianluca, who first welcomed me in Denmark, for the evenings passed at your place, which warmed my spirit in the dark Danish winters. Thanks also to the luxorandi for entertaining me remotely.

Many thanks to my family for their support and affection, and to all the "Di Quinzio in the world" for being my enlarged family (and for the weather updates throughout Italy). Finally, a special thanks to my girlfriend Chiara, who always loves and supports me, and who had the patience to live apart for three years to let me pursue this Ph.D.

Some like to understand what they believe in.
Others like to believe in what they understand.

\- Stanisław Lec

Ph.D. Publications

The following publications have resulted from this Ph.D. project.

Articles in peer-reviewed journals

[J1] **S. Gaiarin**, A. M. Perego, E. Porto da Silva, F. Da Ros, and D. Zibar, "Dual polarization nonlinear Fourier transform-based optical communication system," *Optica*, vol. 5, no. 3, 2018.

[J2] O. Ozolins, X. Pang, M. I. Olmedo, A. Kakkar, A. Udalcovs, **S. Gaiarin**, J. R. Navarro, K. M. Engenhardt, T. Asyngier, R. Schatz, J. Li, F. Nordwall, U. Westergren, D. Zibar, S. Popov, and G. Jacobsen, "100 GHz externally modulated laser for optical interconnects," *Journal of Lightwave Technology*, vol. 35, no. 6, pp. 1174–1179, March 2017.

[J3] X. Pang, O. Ozolins, **S. Gaiarin**, A. Kakkar, J. R. Navarro, M. I. Olmedo, R. Schatz, A. Udalcovs, U. Westergren, D. Zibar, S. Popov, and G. Jacobsen, "Experimental study of 1.55-μm EML-based optical IM/DD PAM-4/8 short reach systems," *IEEE Photonics Technology Letters*, vol. 29, no. 6, pp. 523–526, 2017.

[J4] E. P. da Silva, R. Borkowski, S. Preußler, F. Schwartau, **S. Gaiarin**, M. I. Olmedo, A. Vedadi, M. Piels, M. Galili, P. Guan, S. Popov, C.-S. Brès, T. Schneider, L. K. Oxenløwe, and D. Zibar, "Combined optical and electrical spectrum shaping for high-baud-rate Nyquist-WDM transceivers," *IEEE Photonics Journal*, vol. 8, no. 1, pp. 1–11, 2016.

Contributions to international peer-reviewed conferences

[C1]   R. T. Jones, **S. Gaiarin**, M. P. Yanokov, and D. Zibar, "Noise robust receiver for eigenvalue communication systems," in *Proc. of the Optical Fiber Communications Conference and Exhibition (OFC)*, 2018, paper W2A.59.

[C2]   **S. Gaiarin**, A. M. Perego, E. Porto da Silva, F. Da Ros, and D. Zibar, "Experimental demonstration of dual polarization nonlinear frequency division multiplexed optical transmission system," in *Proc. of the European Conference on Optical Communications (ECOC)*, 2017, paper W.3.C.2.

[C3]   **S. Gaiarin**, F. Da Ros, M. P. Sørensen, and D. Zibar, "Tolerance of continuous NFT spectrum to the optical fiber channel impairments," in *Proc. of the Advanced Photonics Conference (SPPCom)*, 2016, paper SpM3E.5.

[C4]   **S. Gaiarin**, X. Pang, O. Ozolins, R. T. Jones, E. P. da Silva, R. Schatz, U. Westergren, S. Popov, G. Jacobsen, and D. Zibar, "High speed PAM-8 optical interconnects with digital equalization based on neural network," in *Proc. of the Asia Communications and Photonics Conference (ACP)*, Optical Society of America, 2016, paper AS1C.1.

[C5]   O. Ozolins, M. I. Olmedo, X. Pang, **S. Gaiarin**, A. Kakkar, A. Udalcovs, K. M. Engenhardt, T. Asyngier, R. Schatz, J. Li, F. Nordwall, U. Westergren, D. Zibar, S. Popov, Jacobsen, and Gunnar, "100 GHz EML for high speed optical interconnect applications," in *Proc. of the European Conference on Optical Communications (ECOC)*, 2016, paper M.2.C.4.

[C6]   X. Pang, O. Ozolins, **S. Gaiarin**, M. I. Olmedo, R. Schatz, U. Westergren, D. Zibar, S. Popov, and G. Jacobsen, "Evaluation of high-speed EML-based IM/DD links with PAM modulations and low-complexity equalization," in *Proc. of the European Conference on Optical Communication (ECOC)*, 2016, paper W.4.P1.SC5.54.

[C7]   S. Popov, X. Pang, O. Ozolins, M. I. Olmedo, A. Kakkar, **S. Gaiarin**, A. Udalcovs, R. Lin, R. Schatz, J. R. Navarro, A. Djupsjöbacka, D. Zibar, J. Chen, U. Westergren, and G. Jacobsen, "Ultra-broadband high-linear integrated transmitter for low complexity optical intercon-

nect applications," in *Proc. of the Asia Communications and Photonics Conference (ACP)*, 2016, paper AF4C.1.

Contents

Acronyms

ADC	analog-to-digital converter
ADM	add-drop multiplexer
ASE	amplified spontaneous emission
AKNS	Ablowitz-Kaup-Newell-Segur
AWG	arbitrary waveform generator
AWGN	additive white Gaussian noise
B2B	back-to-back
BER	bit error rate
BPD	balanced photodetector
BPS	blind phase search
DAC	digital-to-analog converter
DCF	dispersion-compensating fiber
DBP	digital back-propagation
DFT	discrete Fourier transform
DP-NFDM	dual-polarization nonlinear frequency division multiplexing
DSO	digital storage oscilloscope
DSP	digital signal processing
DT	Darboux transformation
EDC	electrical dispersion compensation

EDFA	erbium-doped fiber amplifier
ENOB	effective number of bits
FEC	forward error correction
FL	fiber laser
FWHM	full-width half-maximum
FWM	four-wave mixing
GLM	Gelfand-Levitan-Marchenko
GVD	group velocity dispersion
HD-FEC	hard-decision forward error correction
I	in-phase
INFT	inverse nonlinear Fourier transform
ISI	inter-symbol interference
IST	inverse scattering transform
IVP	initial value problem
LO	local oscillator
LPA	lossless path-averaged
MS	Manakov system
ML	maximum likelihood
MZM	Mach-Zehnder modulator
MZSP	Manakov-Zakharov-Shabat spectral problem
NFDM	nonlinear frequency division multiplexing
NFT	nonlinear Fourier transform
NIS	nonlinear inverse synthesis
NLSE	nonlinear Schrödinger equation

NMSE	normalized mean squared error
OBPF	optical band pass filter
OFDM	orthogonal frequency-division multiplexing
OPC	optical phase conjugation
OSNR	optical signal-to-noise ratio
PAPR	peak-to-average power ratio
PC	polarization controller
PDE	partial differential equation
PMD	polarization mode dispersion
ppm	parts-per-million
PSK	phase-shift keying
Q	quadrature
QAM	quadrature amplitude modulation
QPSK	quadrature phase-shift keying
SDM	space-division multiplexing
SMF	single-mode fiber
SNR	signal-to-noise ratio
S/P	serial-to-parallel
SPM	self-phase modulation
SSFM	split-step Fourier method
WDM	wavelength-division multiplexing
ZSP	Zakharov-Shabat spectral problem

List of frequently used symbols

$a(\lambda)$	Scattering coefficient
$\bar{a}(\lambda)$	Scattering coefficient
$b(\lambda)$	Scattering coefficient
$\bar{b}(\lambda)$	Scattering coefficient
$\widehat{b}(\widehat{\lambda})$	Eigenvalue and scattering coefficient estimated at the receiver
d	Bits per data frame (NFDM symbol)
k	Bits per eigenvalue
ℓ	Space coordinate
$q(t,z)$	Normalized complex envelope of the electric field
$\widetilde{q}(t)$	$q(t,0)$ modified by the DT
r_1, r_2	Radius of the constellations associated to the eigenvalues λ_1, λ_2
$\mathbf{r}$	Digital received NFDM-symbol
$\mathbf{s}$	Digital transmitted NFDM-symbol
t	Normalized time coordinate
u	$\phi^N(t,\lambda)$ propagated forward in the forward-backward method
v	Solution of the ZSP / MZSP
$\widetilde{v}$	Solution of the ZSP / MZSP modified by the DT

$\bar{v}$ Darboux transformation auxiliary solution

w $\phi^N(t, \lambda)$ propagated backward in the forward-backward method

z Normalized space coordinate

C_r Reference $b(\lambda_i)$

D Fiber dispersion parameter

$E(\tau, \ell)$ Complex envelope of the electric field

$E_{Rx}(\tau)$ Received optical waveform

$E_{Rx}(\tau_n)$ Received digital waveform

$E_{Tx}(\tau)$ Transmitted optical waveform

$E_{Tx}(\tau_n)$ Transmitted digital waveform

$\mathbf{G}_0$ Darboux transformation matrix

K Number of samples of the time domain signal $q(t)$

L Fiber link length

L_d Dispersion length

L_s Fiber span length

$\boldsymbol{L}$ Lax operator

$\mathcal{L}$ Nonlinear Schrödinger equation length normalization factor

M Constellation order

$\boldsymbol{M}$ Lax space-evolution matrix

N Number of eigenvalues

N_s Number of spans constituting a fiber link

P Nonlinear Schrödinger equation power normalization factor

P_{tx} Average power of the transmitted optical signal

$\boldsymbol{P}$ Lax time-evolution matrix

$Q_c(\lambda, z)$ Continuous spectral amplitude

$\widehat{Q}_c(\lambda)$ Continuous spectral amplitude estimated at the receiver

$Q_d(\lambda_i, z)$ Discrete spectral amplitude

R_s Symbol rate

T Total time duration of the transmitted signal $E_{Tx}(\tau)$

T_b Bit period

T_s Symbol period

T_0 Nonlinear Schrödinger equation time-normalization factor

V_π Mach-Zehnder modulator half-wave voltage

W Bandwidth containing 99% of the power of the signal

α Fiber-loss parameter

β_2 Fiber group velocity dispersion

γ Fiber nonlinear parameter

$\bar{\gamma}$ Fiber nonlinear parameter averaged over one span length

θ_e Relative angle between constellations for the two eigenvalues

θ_p Relative angle between constellations for the two polarizations

$\lambda \in \mathbb{C}$ Spectral parameter

$\lambda \in \mathbb{R}$ Nonlinear frequency (Real spectral parameter)

$\lambda_i \in \mathbb{C}^+$ Discrete eigenvalue (Complex spectral parameter)

$\widehat{\lambda}$ Spectral parameter estimated at the receiver

τ Time coordinate

$\phi^P(t, \lambda)$ Jost solution

$\bar{\phi}^P(t, \lambda)$ Jost solution

$\phi^N(t, \lambda)$ Jost solution

$\bar{\phi}^N(t, \lambda)$ Jost solution

$\psi(t, \lambda)$ MZSP solution in the trapezoidal method (after change of variables)

$\psi^P(t, \lambda)$ Jost solution in the trapezoidal method (after change of variables)

$\psi^N(t, \lambda)$ Jost solution in the trapezoidal method (after change of variables)

$\boldsymbol{\Theta}$ Darboux transformation auxiliary solution matrix

CHAPTER 1

Introduction

In the mid 90s the wide-spreading of the world wide web made the Internet go from being a technology used only by researchers and technology enthusiasts to become the commodity central to everyone's life we know today. This global network for exchanging information in real time radically changed the way we do business, access the news, and communicate among ourselves, thus shaping the modern information society. If at first it was only possible to access simple static web pages, in a matter of two decades a multitude of services such as e-mail, e-commerce, social networks, cloud computing, and video streaming services are provided via the Internet. In the near future the Internet is expected to become even more pervasive with the advent of the Internet of Things. This rapid increment of the number of bandwidth-demanding services, together with the increasing number of worldwide connected devices, will cause the global data traffic to grow at a compound annual growth rate of 24% in the period 2016-2021, making the global IP traffic reach 278 EB per month in 2021 [1].

This impressive amount of information flow is only possible thanks to the fiber-optic network that constitutes the core of the Internet. The enormous bandwidth of the optical fibers together with their low transmission losses makes it possible to transmit massive quantities of data over long distances, otherwise impossible with previously existing technologies such as coaxial cables or wireless systems.

The transmission throughput of the optical fibers has increased exponentially over the years from the 70s to the present days [2]. This was possible thanks to a refinement of the existing electrical and optical components constituting the optical transmission systems, and to the introduction of new disruptive technologies such as the erbium-doped fiber amplifier (EDFA) and the dispersion-compensating fiber (DCF) that enabled the deployment of long-haul direct-detected unregenerated wavelength-division multiplexing (WDM) systems. Once the information rate could not be increased anymore by using more bandwidth, due to the limited amplification window offered by the

EDFAs, the next direction was to increase the spectral efficiency, i.e., encoding more bits in the same bandwidth, by using advanced modulation formats [3]. Around the beginning of 2010, single-mode fiber (SMF) optical transmission systems using coherent detection, multi-level modulation formats, and digital signal processing (DSP) algorithms used to compensate for linear impairments such as chromatic dispersion and polarization mode dispersion (PMD), started to be deployed [4]. They constitute the current generation of optical transmission systems [5]. Unfortunately, not even these type of systems will be able to satisfy the continuous demand of a higher transmission rate in the near future.

The main problem of these systems is that they are based on technologies originally developed for a linear channel with additive white Gaussian noise (AWGN). The capacity of such a channel increases indefinitely with the bandwidth and launch power of the signal [6]. Given a fixed bandwidth, the transmission rate of the system can be increased by using symbol constellations with higher order. Larger constellations need larger power to maintain the signal-to-noise ratio (SNR) at a level that allows recovering the transmitted information. However, the fiber-optic channel is inherently nonlinear due to the Kerr effect [7]. The nonlinearity of the fiber causes a distortion of the signal, called nonlinear interference, proportional to the cube of the power of the signal itself [8], which contributes in decreasing the SNR at the receiver of current coherent optical transmission systems. The received SNR is dominated by the amplified spontaneous emission (ASE) noise of the amplifiers at low powers and by the nonlinear interference at high powers, so that an optimal launch power that maximize the transmission rate of the system exists in between these two power regimes [9–11]. This condition imposes a practical limit on the achievable transmission rate of the system.

The nonlinearity of the fiber is the current bottleneck on the performance of the currently deployed coherent optical systems, and for this reason a lot of effort has been put in trying to compensate this detrimental effect. To solve this problem the research community has tried to mitigate the impact of nonlinearity through a wealth of techniques in the digital and optical domain.

The reference method for nonlinearity mitigation in the digital domain is digital back-propagation (DBP) [12, 13]. DBP is a technique to compensate the deterministic effect of the fiber nonlinearity by propagating the received signal backward in a digital channel. This channel is modeled by the nonlinear Schrödinger equation (NLSE) and represents the nonlinear fiber-optic transmission channel. The main drawback of this method is its high complexity arising from the necessity of finely partitioning the fiber in small sections along

its length, and repeating the operations to solve the differential equation for each section. The complexity of this method scales with both the power of the signal and the transmission length, making it very unpractical for long haul systems. Moreover, to perform optimally, DBP needs to process the channel of interest together with all the interfering channels, thus imposing a high requirement on the electrical bandwidth of the receiver.

In order to avoid the need for large electrical bandwidth and high computational power, many optical nonlinearity compensation techniques have been proposed, such as optical phase conjugation (OPC) [14, 15], or phase-conjugated twin-waves transmission [16]. Although these techniques are particularly appealing because they can be applied to multiple channels of a WDM system at once, they come with their own specific problems, such as requirements on the link symmetry, and reduced spectral efficiency.

Alternatively to increase the transmission rate of the systems by increasing the launch power, with the necessity of compensating for the fiber nonlinearity effect, a different approach is to increase the data rate by using multi-core or multi-mode fibers. Using these fibers it is possible to encode more data in their multiple spatial degrees of freedom [17–19]. This umbrella of techniques is called space-division multiplexing (SDM). SDM would allow obtaining high data rates even when the system is operated in the linear power regime where the impact of the fiber nonlinearity is negligible. However, the adoption of SDM would require installing a completely new fiber infrastructure, which is very complex, time-consuming, and costly. Moreover, due to the complicated mode-coupling and inter-core cross-talk, in order to descramble the data, it is often required to use electronic DSP techniques that can have prohibitive computational power requirements [17].

The approaches presented so far treats the nonlinearity as an impairment of the system and try to mitigate its effect without considering the underlying problem that the transmission system is designed for a linear channel. An alternative approach is to account for the nonlinear nature of the channel and to design a system tailored for this channel.

The idea of including the nonlinear effect of the fiber into the design of an optical communication system was introduced with the soliton communication [20–22]. Indeed, by properly carving the envelope of the transmitted optical signal, it is possible to make the resulting pulse maintain its shape along the propagation in the nonlinear fiber thanks to a perfect balance between chromatic dispersion and Kerr nonlinearity. In this sense the two effects, considered a limit to the system when acting independently, become constitutive elements of the system.

From the idea of soliton communication, Hasegawa and Nyu [23] proposed the concept of *eigenvalue communication*, by noting that, associated to the solitons, there is a set of parameters, called eigenvalues, invariant during the transmission of the optical signal in the fiber. Soliton communication can be considered a particular case of eigenvalue communication where a single eigenvalue is used to carry information. In the general case, multiple eigenvalues can be modulated at once in order to encode more information bits per pulse.

Eigenvalue communication exploits the exact integrability of the NLSE through the inverse scattering transform (IST) [24], also-called nonlinear Fourier transform (NFT), as the master evolution equation of the electric field propagating in a SMF. The integrable NLSE accounts only for the first order dispersion and the nonlinear term, disregarding all other effects, such as attenuation, higher-order dispersion, Raman effect, and noise. For this reason, this model is only partially able to model the evolution of a signal in a real fiber-channel where these effects are present. Integrability of the NLSE was demonstrated by Zakharov and Shabat back in 1972 [25], when they found a spectral problem associated to the NLSE related to a set of ordinary linear differential equations. Following this approach, it is possible to identify a set of spectral parameters $\lambda \in \mathbb{C}$, and the so-called *scattering coefficients* associated to the spectral parameters. The nonlinear Fourier spectrum of a signal consists of a set of spectral parameters and the respective associated scattering coefficients $\{\lambda, S(\lambda)\}$. The spectral parameters belong either to a *discrete spectrum*, in which case are called eigenvaluez, or to a *continuous spectrum*, in which case are called nonlinear frequencies; the first describes the solitonic components of the signal, while the second is associated with dispersive waves.

The transmission of solitons, and thereby eigenvalue communication, lost the attention of the research community in the late 1990s due to effects such as soliton-to-soliton collisions, inter-channel cross-talk, and Gordon-Haus jitter [26] that made those type of systems not competitive with existing WDM systems. With the return of coherent detection, supported by the advanced DSP for signal modulation and demodulation, the situation is completely different now. The ability to manipulate signals in the digital domain at the transmitter and at the receiver is opening up new opportunities for equalization strategies. It also allows the modulation of not only the eigenvalues, but also the amplitude and the phase of the scattering coefficients associated to both the eigenvalues and the nonlinear frequencies, to enhance the overall spectral efficiency. This has resulted in a renewed interest in eigenvalue communication [27, 28], which, with various modifications, is now growing as a new paradigm in optical communications [29].

Some of the recent publications, re-proposed the modulation method based on the original eigenvalue communication idea proposed in [23] where only the position of the eigenvalues is modulated [27, 30–33]. Beside this technique, new methods of using the *nonlinear spectrum* have emerged. A first one, often called nonlinear frequency division multiplexing (NFDM) for its similarity with the classical orthogonal frequency-division multiplexing (OFDM), is based on the modulation of the amplitude and phase of the complex amplitudes associated to the nonlinear frequencies and the eigenvalues. This method can use the continuous spectrum [34–36], the discrete spectrum [37–41] or both together [42–44]. NFDM systems underwent a rapid progress, going from systems using only two eigenvalues and transmission rate of 4 Gbit/s [37] to systems using both continuous and discrete spectrum with throughput of 65 Gbit/s, and able to outperform OFDM in terms on nonlinearity tolerance [45]. The current record transmission rate for NFDM is of 125 GB/s with spectral efficiencies of 2.3 bit/s/Hz and transmission distance of almost 1000 km using the continuous spectrum [44].

An alternative modulation method, called nonlinear inverse synthesis (NIS), instead of encoding the data bits on the nonlinear spectrum directly, uses the NFT as an extra DSP layer on top of classical OFDM systems. This technique encodes the linear Fourier spectrum resulting from the OFDM modulation on the NFT continuous spectrum in order to transmit it over the fiber with a lower impact of the fiber nonlinearity [46–48]. Recent works using the NIS approach also showed impressive results, allowing to reach transoceanic transmission distances up to 7344 km [47].

Besides using the nonlinear spectrum as a carrier of information, the NFT can also be used only as a tool to remove the effect of nonlinearity on signals transmitted with classical modulation formats by using an approach similar to DBP. For this reason this method has been named NFT-DBP [49, 50]. Unfortunately, this approach presents some challenges, as the difficulty in locating an unknown number of discrete eigenvalues, that makes it difficult to use it in practical communication scenarios, especially in the power regime where the effect of nonlinearity is relevant.

Other recent research highlights have focused on building more practical NFT-based systems with the implementation of fast direct and inverse NFT algorithms with real-time implementation in mind [51], and with the investigation of the NFT with periodic boundaries conditions, which would allow to minimize the processing window of the signal at the receiver [52–54]. Theoretical works have been done to characterize the noise behavior on the nonlinear spectrum [55–58] and to estimate the capacity or bounds on the capacity for

NFT-based communication systems [59–63]. Finally, the NFT has recently also been used outside the communication scenario to perform identification of lasing regimes in mode-locked lasers [64].

1.1   Motivation and outline of contributions

This Ph.D. work is part of the Marie Curie initial training network project Allied Initiative for Training and Education in Coherent Optical Network (ICONE). The main goal of the project is the design of next-generation high capacity high order constellations coherent optical transmission systems using DSP, where fiber nonlinearities may then be a strongly limiting design factor.

Among the different directions undertook in ICONE to try to overcome the nonlinearity problem and increase the capacity of next-generation coherent system, this Ph.D. project has focused on NFT-based transmission techniques, given their potential of avoiding the nonlinear cross-talk among different transmission channels caused by the fiber nonlinearities.

During the past three years, this communication method underwent a rapid development, going from a mere proof of concept to be used in systems able to transmit hundreds of Gb/s of information. Nonetheless all the experimentally demonstrated systems remained limited in modulating only one polarization component of the transmitted light thus not exploiting the full capacity of the SMF. Only two theoretical works started exploring this topic very recently [65, 66].

The main contribution of this thesis is the presentation of a full mathematical framework for designing a dual-polarization NFT-based optical transmission system employing the discrete nonlinear spectrum and the first experimental demonstration of a dual-polarization NFDM system. The choice of investigating the use of the discrete spectrum is justified by the fact that this spectrum is associated to a signal whose power is in the nonlinear power regime. This regime is where NFT-based optical communication systems may possibly outperform standard linear coherent systems, which are instead limited by the fiber nonlinearities. The dual-polarization NFT enables using the second polarization supported by SMFs in order to potentially doubling the transmission rate, making a significant step forward in the evolution of eigenvalue communication. In addition this thesis provides an overview of the structure and on some of the design aspects of a discrete NFDM system.

1.2   Structure of the thesis

This thesis is divided into four chapters.

Chapter 2 provides the fundamental notions necessary to define an NFDM communication system. The structure of a coherent optical communication system, and the model of an ideal channel based on the NLSE are presented. Then the inverse scattering method based on this channel is introduced and the key concepts of nonlinear spectrum and linear evolution in the nonlinear domain are presented. Finally, a generalized channel model that takes into account fiber losses and noise is also presented together with a numerical investigation of the effects of these non-ideal conditions on the evolution of the nonlinear spectrum.

Chapter 3 provides a full description of an NFDM optical communication system employing the discrete nonlinear spectrum as information carrier. The design aspects characteristic of NFDM for the transmitter and the receiver are discussed based on the recent literature on the subject, and results from numerical simulations are shown to provide a better understanding of some particular problems of this type of systems.

Chapter 4 introduces the novel concept of dual-polarization nonlinear frequency division multiplexing (DP-NFDM) communication system. The mathematical framework that defines the dual-polarization NFT is presented, and the numerical methods to compute the direct and inverse transformation in the dual-polarization case are introduced for the case of discrete nonlinear spectrum. Then the structure of a DP-NFDM system is described in terms of DSP blocks and optical setup. Finally, the results of the first experimental demonstration of a DP-NFDM system are presented. Transmission over lumped amplification link up to $375.5\,\mathrm{km}$ have been achieved showing the applicability of the proposed system.

Chapter 5 summarize the results of the thesis, and it discusses some open challenges and future research directions for the NFT-based communication systems.

Nonlinear Fourier transform fundamentals

This chapter introduces the fundamental concepts required to define a nonlinear frequency division multiplexing (NFDM) system, with a particular focus on the channel models and the nonlinear Fourier transform (NFT) theory. Section 2.1 reviews the general structure of a coherent optical communication system, which constitutes the base of an NFDM system. Section 2.2 presents the evolution equation that provides the channel model upon which the NFT is defined and discusses the normalization of this equation. Section 2.3 first revises the Fourier method for solving linear partial differential equations (PDEs), which is then used to introduce the concept of inverse scattering method for solving the nonlinear Schrödinger equation (NLSE). Then the concept of auxiliary spectral problem is introduced together with the direct and inverse NFT arriving at the definition of nonlinear spectrum. The relation between the nonlinear spectrum and the time domain signal is then given for the special case of the fundamental soliton. Section 2.4 presents a generalized channel model that accounts for the fiber loss and the noise. Finally, in Section 2.5, the behavior of the NFT over this generalized channel is analyzed in terms of spectral distortion, and it is compared to that of the classical Fourier spectrum, which is used as a benchmark.

2.1 Coherent optical communication system

Modern fiber-optic communication systems employ modulation of amplitude and phase of the optical field, enabled by coherent detection, together with advanced digital signal processing (DSP) techniques to achieve unprecedented spectral efficiencies.

The flexibility of having access to the full field of the signal permits designing different type of modulation formats, from conventional linear ones, like
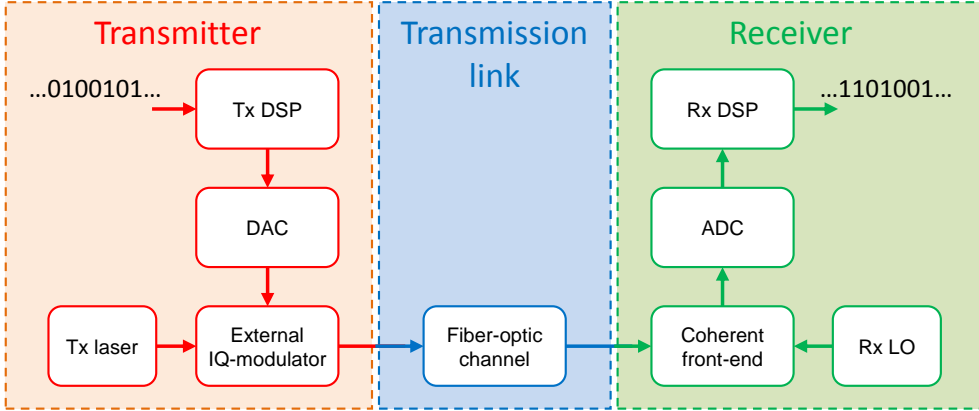
Figure 2.1: General structure of a coherent optical communication system.

phase-shift keying (PSK) and quadrature amplitude modulation (QAM), to more complex ones, as orthogonal frequency-division multiplexing (OFDM), and finally to NFT-based formats, such as nonlinear inverse synthesis (NIS) and NFDM.

The main components of a generic coherent optical transmission system, whose block diagram is illustrated in Figure 2.1, are now reviewed. At the transmitter the input data bits are processed by a DSP chain, whose tasks are: to encode the information bits to provide forward error correction (FEC), to map these bits to predefined symbols, and finally to produce a time-shaped digital waveform. This waveform is fed to a digital-to-analog converter (DAC), which converts it from the digital to the analog domain. The resulting electrical signal drives an optical modulator that shapes the electrical field of a laser. The modulation of the in-phase (I) and quadrature (Q) components of the optical signal are usually performed by an external IQ-modulator employing Mach-Zehnder interferometers. The modulated optical field is transmitted through the fiber-optic channel, which can be composed of several spans of optical fiber interleaved with optical amplifiers (usually erbium-doped fiber amplifier (EDFA) or Raman amplifiers). At the output of the fiber, the received signal is detected by a coherent receiver, which acquires both amplitude and phase of the optical signal and linearly translates them into an electrical waveform. The coherent detection requires an additional laser that acts as a local oscillator (LO) and that ideally should be phase and frequency locked to the signal carrier; in practical cases this not true, and the small frequency

offset between the LO and the signal carrier, and their initial phase differ-
ence need to be recovered by the receiver DSP. The analog electrical signal
is digitized by the analog-to-digital converter (ADC) and then processed by
the receiver DSP chain, which synchronizes the signal, mitigates the various
impairments added by the noisy optical-electrical channel, demodulates the
digital waveform, and finally decodes the data frame in order to retrieve the
information bits.

The structure of a coherent optical communication system described above
is very generic (for an in-depth description of it see [3, 7, 67]), and it represents
the basic skeleton of various systems, including the NFDM system. The fiber-
optic channel model will be presented in the next section, while the transmitter
and receiver DSP chains of a NFDM system will be described in detail in
Chapter 3.

2.2 Channel model

The principle of NFDM communication is intimately related to the fiber chan-
nel model given by the NLSE. Indeed, to transmit information over the fiber
channel avoiding the impact of the nonlinearity, it is necessary to generate a
signal that is matched to the NLSE representing the specific channel of the
system. In this section we present the integrable version of the NLSE and its
normalized version that will then be used in the following sections to define
the NFT.

2.2.1 Nonlinear Scrödinger equation

The evolution of the slowly-varying complex-valued envelope of the scalar
electric field $E(\tau, \ell)$ propagating in a single-mode fiber (SMF) is modeled by
the scalar NLSE [7]

$$\frac{\partial E(\tau, \ell)}{\partial \ell} = -i\frac{\beta_2}{2}\frac{\partial^2 E(\tau, \ell)}{\partial \tau^2} + i\gamma|E(\tau, \ell)|^2 E(\tau, \ell), \qquad (2.1)$$

where $0 \leq \ell \leq L$ is the space coordinate with L the fiber length, τ is the time
in the reference frame co-moving with the group velocity of the envelope, β_2
is the group velocity dispersion (GVD), and γ is the nonlinear parameter.

The particular form of the NLSE in (2.1) is integrable with the inverse
scattering method. However, this version of the NLSE disregards many effects
that are present in real SMFs, such as attenuation, higher-order dispersion,

and Raman effect, and also does not account for the noise. All these effects break the integrability of the NLSE and their impact on the applicability of the inverse scattering method needs to be investigated for each of them individually. The impact of the loss and the noise is investigated in Section 2.5.

2.2.2   Normalized nonlinear Schrödinger equation

In order to remove any dependency on the specific channel, i.e., the dependency on the particular values of the GVD and the nonlinear parameter, it is common to work with a normalized version of the NLSE when defining the NFT. The normalized NLSE is obtained from (2.1) by performing the change of variable

$$q = \frac{E}{\sqrt{P}}, \qquad t = \frac{\tau}{T_0}, \qquad z = -\frac{\ell}{\mathcal{L}}, \tag{2.2}$$

with $P = |\beta_2|/(\gamma T_0^2)$, $\mathcal{L} = 2T_0^2/|\beta_2|$ and T_0 is a free normalization parameter, leading to

$$i\frac{\partial q(t,z)}{\partial z} = \pm \frac{\partial^2 q(t,z)}{\partial t^2} + 2|q(t,z)|^2 q(t,z), \tag{2.3}$$

where z and t represent the normalized space and time variables. The factors P, T_0 and $\mathcal{L}$ have physical units of power, time, and length, respectively, leading to the unitless set of variables in (2.2).

The plus and minus signs in front of the dispersion term in (2.3) correspond to the cases of normal ($\beta_2 > 0$) and anomalous ($\beta_2 < 0$) dispersion regimes. In the rest of this thesis, only the anomalous dispersion regime is considered, since it corresponds to the dispersion regime of standard SMFs and the only one supporting (bright) solitons. For this case the normalized NLSE finally results in

$$i\frac{\partial q(t,z)}{\partial z} = \frac{\partial^2 q(t,z)}{\partial t^2} + 2|q(t,z)|^2 q(t,z). \tag{2.4}$$

The normalization of the NLSE is only a change of variables, and for this reason, there are several ways to normalize it. In the NFT context, it is important to always keep in mind the normalization used in a specific research work because different forms of the normalized NLSE lead to different forms of the NFT operators. This fact makes sometimes the comparison of different papers in the literature somewhat difficult, and the specific form of some algorithms incompatible with each other. The most common normalizations used in the literature are now presented.

This thesis adopts the normalized NLSE (2.4) used in one of the works that popularized the NFT in the recent years [28], and also also appearing in other works such as [32, 42, 68, 69]. We should note though, that the non-normalized NLSE used in [28] differs from (2.1) by a minus in the first term.

Another popular version of the normalized NLSE, which more resemble the structure of (2.1), is

$$i\frac{\partial q(t, z)}{\partial z} = -\frac{1}{2}\frac{\partial^2 q(t, z)}{\partial t^2} - |q(t, z)|^2 q(t, z), \tag{2.5}$$

and the corresponding change of variables is

$$q = \frac{E}{\sqrt{P}}, \qquad t = \frac{\tau}{T_0}, \qquad z = \frac{\ell}{\mathcal{L}}, \tag{2.6}$$

with $P = |\beta_2|/(\gamma T_0^2)$, $\mathcal{L} = T_0^2/|\beta_2|$ and T_0 is a free normalization parameter. Compared to this change of variable, the one in (2.2) has an additional minus and a factor 2 in the normalization of the space coordinate. Some of the works where this equation is used are [7, 23, 70–72].

Finally, there is another form of the normalized NLSE, which appears in [24, 73, 74], and that takes the form

$$i\frac{\partial q(t, z)}{\partial z} = -\frac{\partial^2 q(t, z)}{\partial t^2} - 2|q(t, z)|^2 q(t, z) \tag{2.7}$$

and can be obtained from (2.1) using the change of variable in (2.2) but replacing the change of variable $\ell \to z$ with $z = \ell/\mathcal{L}$.

In Table 2.1, Table 2.2, and Table 2.3 at the end of the chapter, a summary of the different forms of the normalized NLSE present in the literature is given, together with the corresponding change of variables.

2.3   Nonlinear Fourier Transform

The NLSE (2.4) belongs to a class of nonlinear PDEs that can be solved exactly, i.e., it is possible to find analytical solutions, by a mathematical method called inverse scattering transform (IST). This type of PDEs are said to be *integrable*. Explaining the concept of integrability is out of the scope of this thesis, so we refer the reader to the works [75, 76] that provide a thorough definition of integrability.

Similarly to the linear Fourier transform method, commonly used to solve initial value problems (IVPs) for linear PDEs, the IST can be used to solve IVPs for nonlinear PDEs such as the NLSE [24]. The parallelism between the two methods has driven some authors to rename the IST as NFT [28], which is the name currently used in the engineering community [29]. The name NFT is further justified by the fact that in the limit of very low power of the signal $q(t, z)$, it can be proven that the NFT asymptotically converge to the Fourier transform [24].

The Fourier method is reviewed in the next section. Given its similarity with the inverse scattering method, it can help the reader in the understanding of the second. The spectral problem and the formal definition of direct and inverse NFT are introduced right afterward.

2.3.1   The Fourier method for solving linear partial differential equations

The Fourier method is a technique used to solve linear PDEs, which is useful in those cases where the considered differential equation assumes a simpler form in the Fourier domain.

For example, if we consider the IVP for the evolution equation describing the propagation of a signal in a linear, lossless, dispersive medium [70]

$$\frac{\partial q(t, z)}{\partial z} = -i\frac{\partial^2 q(t, z)}{\partial t^2}, \qquad q(t, z_0) = q_0(t), \tag{2.8}$$

where $q_0(t)$ is a known solution at the position z_0, we have that in the Fourier domain the IVP takes the form

$$\frac{\partial}{\partial z}\mathcal{Q}(w, z) = iw^2\mathcal{Q}(w, z), \qquad \mathcal{Q}(w, z_0) = \mathcal{Q}_0(w), \tag{2.9}$$

where $\mathcal{Q}(w, z) = \mathfrak{F}\{q(t, z)\}$ is the Fourier transform of the signal $q(t, z)$, and $\mathcal{Q}_0(w)$ the Fourier transform of the know solution. By integrating (2.9) in the interval $[z_0, z]$ we obtain

$$\mathcal{Q}(w, z) = \exp\left(iw^2 z\right)\mathcal{Q}(w, z_0), \tag{2.10}$$

which is the explicit space evolution equation of the Fourier spectrum of $q(t, z)$.

To compute the solution of (2.8) at a point in space z_1, when a solution is known at the point z_0, we can use the following procedure (Figure 2.2):
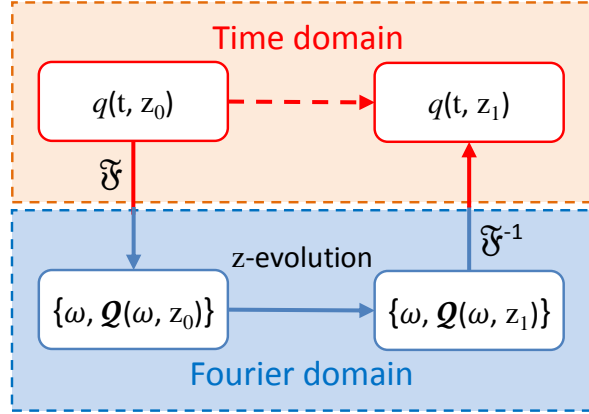
Figure 2.2: Scheme of the Fourier method for solving the IVP for linear PDEs.

1. compute the Fourier transform $\mathcal{Q}(w, z_0)$ of $q(t, z_0)$;

2. compute the evolution of $\mathcal{Q}(w, z_0)$ from the position z_0 to the position z_1 according to (2.10);

3. compute the inverse Fourier transform of $\mathcal{Q}(w, z_1)$ to obtain the solution $q(t, z_1)$.

A modified version of these three steps constitutes the inverse scattering method to solve an IVP for the NLSE as we are going to explain in the next section.

2.3.2   The inverse scattering method for solving nonlinear partial differential equations

The inverse scattering method is a procedure to solve the following IVP for the NLSE

$$i\frac{\partial q(t,z)}{\partial z} = \frac{\partial^2 q(t,z)}{\partial t^2} + 2|q(t,z)|^2 q(t,z), \qquad q(t,z_0) = q_0, \qquad (2.11)$$

where q_0 is a known envelope of the signal of interest at some position $z = z_0$. As for the Fourier method, the inverse scattering method requires the following
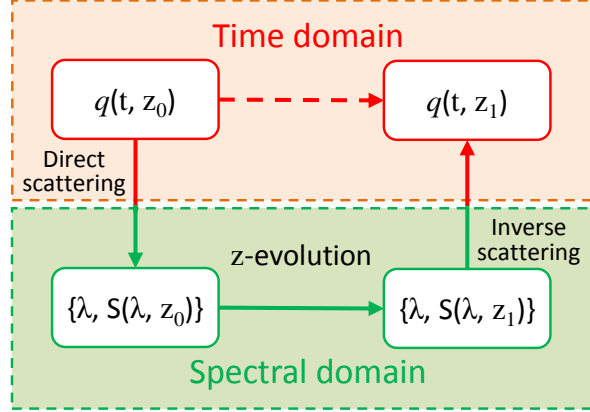
Figure 2.3: Scheme of the inverse scattering method for solving the IVP for the NLSE.

three steps: a transformation from the time domain to a spectral domain, an evolution equation for the spectrum, and an inverse transformation.

Although the method to solve the NLSE using the NFT is conceptually similar to the linear Fourier method presented in the previous section, the two transformations are rather different. To define the NFT it is first necessary to associate an auxiliary problem to the NLSE, represented by a pair of equations. The first equation gives the scattering problem or spectral problem. In the case of the NLSE, it is called the Zakharov-Shabat spectral problem (ZSP) after the name of the authors that first applied the inverse scattering method to the NLSE [25]. The scattering problem, which depends on the signal $q(t, z)$, can be solved to obtain the scattering data. The second equation provides a linear evolution equation for the scattering data. The relation between the scattering data and the signal can then be used to reconstruct the signal in a different point in space from the evolved scattering data [72]. This procedure, depicted in Figure 2.3, is very similar to the one presented in the previous section.

2.3.3 Inverse scattering auxiliary problem

The auxiliary problem for the NLSE is defined, in the Ablowitz-Kaup-Newell-Segur (AKNS) form [24], by the following pair of linear differential equations

$$\frac{\partial v}{\partial t} = \boldsymbol{P}v \tag{2.12a}$$

$$\frac{\partial v}{\partial z} = \boldsymbol{M}v \tag{2.12b}$$

where v is a complex auxiliary vector, and the matrices $\boldsymbol{P}$ and $\boldsymbol{M}$ are called the Lax pair. These matrices depends on the signal $q(t)$ and on a spectral parameter $\lambda \in \mathbb{C}$ (note that we dropped the space coordinate for brevity). Equation (2.12a) can equivalently be written, after simple algebra, as an eigenvalue problem

$$\boldsymbol{L}v = \lambda v \tag{2.13}$$

as was proposed in the original Lax formulation [77]. $\boldsymbol{L}$ is a linear operator and is called the Lax operator, and the λ belong to the spectrum of this operator.

If we impose the condition that λ are invariant upon spatial propagation, $\frac{\partial \lambda}{\partial z} = 0$, the compatibility condition, $\frac{\partial}{\partial t}\frac{\partial}{\partial z}v = \frac{\partial}{\partial z}\frac{\partial}{\partial t}v$, of the system (2.12) can be written in a form called *zero-curvature condition* [28]

$$\frac{\partial \boldsymbol{P}}{\partial z} - \frac{\partial \boldsymbol{M}}{\partial t} + [\boldsymbol{P}, \boldsymbol{M}] = 0, \tag{2.14}$$

where $[\boldsymbol{P}, \boldsymbol{M}] = \boldsymbol{P}\boldsymbol{M} - \boldsymbol{P}\boldsymbol{M}$ is the commutator of the two matrices. By properly choosing the matrices $\boldsymbol{P}$ and $\boldsymbol{M}$ we can make the compatibility condition (2.14) be exactly the NLSE (after algebraic simplification), thus relating the original problem to the spectral problem. Unfortunately, there is not an analytical method to derive the matrices and they need to be properly guessed [77]. For the NLSE the matrices $\boldsymbol{P}$ and $\boldsymbol{M}$ have been found by Zakharov and Shabat and they are given by

$$\boldsymbol{P} = \begin{pmatrix} -i\lambda & q \\ -q^* & i\lambda \end{pmatrix}, \quad \boldsymbol{M} = j \begin{pmatrix} -2i\lambda^2 + i|q|^2 & 2\lambda q + i\frac{\partial q}{\partial t} \\ -2\lambda q^* + i\frac{\partial q^*}{\partial t} & 2i\lambda^2 - i|q|^2 \end{pmatrix}, \tag{2.15}$$

where * denotes complex conjugation. The Lax pair of matrices $\boldsymbol{P}$ and $\boldsymbol{M}$, and the Lax operator $\boldsymbol{L}$ are given in Table 2.1, Table 2.2, and Table 2.3 for the different normalizations of the NLSE presented in Section 2.2.2.

Equation (2.12a) is the ZSP and is used to calculate the scattering data, while (2.12b) defines its evolution along the spatial coordinate, as (2.10) describes the propagation of the Fourier spectrum of the know solution $q_0(t)$.

The operation of finding the scattering data given the signal $q(t)$ is called direct scattering problem or direct NFT, while the reverse operation is called inverse scattering problem or inverse nonlinear Fourier transform (INFT).

2.3.4   Direct nonlinear Fourier transform

Assuming that the signal $q(t)$ is absolutely integrable, $q(t) \in L^1(\mathbb{R})$, and that it satisifes the vanishing boundaries conditions, i.e., $|q(t)| \to 0$ for $|t| \to \infty$, a possible set of solutions of (2.12), called Jost solutions, are [28]:

$$\phi^N(t,\lambda) \to \begin{pmatrix} 1 \\ 0 \end{pmatrix} e^{-i\lambda t}; \qquad \bar{\phi}^N(t,\lambda) \to \begin{pmatrix} 0 \\ 1 \end{pmatrix} e^{i\lambda t} \qquad t \to -\infty \qquad (2.16a)$$

$$\phi^P(t,\lambda) \to \begin{pmatrix} 0 \\ 1 \end{pmatrix} e^{i\lambda t}; \qquad \bar{\phi}^P(t,\lambda) \to \begin{pmatrix} 1 \\ 0 \end{pmatrix} e^{-i\lambda t} \qquad t \to +\infty \; . \qquad (2.16b)$$

If we compute the Wronskian, defined as $W(u,v) = uv - vu$, of the two solutions $\phi^N(t,\lambda)$ and $\bar{\phi}^N(t,\lambda)$ as $t \to -\infty$ we have

$$W(\phi^N(t,\lambda), \bar{\phi}^N(t,\lambda)) = 1 \qquad (2.17)$$

and in the same way for $\phi^P(t,\lambda)$ and $\bar{\phi}^P(t,\lambda)$ as $t \to +\infty$ we have

$$W(\phi^P(t,\lambda), \bar{\phi}^P(t,\lambda)) = -1. \qquad (2.18)$$

We conclude that the vectors of each pair are linearly independent of each other given that their Wronskian is not identically zero. For this reason $\{\phi^N(t,\lambda), \; \bar{\phi}^N(t,\lambda)\}$ and $\{\phi^P(t,\lambda), \; \bar{\phi}^P(t,\lambda)\}$ form two linearly dependent bases for the eigenspace associated to λ. We can write the solutions $\phi^N(t,\lambda)$ and $\bar{\phi}^N(t,\lambda)$ as a linear combination of the basis vectors $\{\phi^P(t,\lambda), \; \bar{\phi}^P(t,\lambda)\}$ as

$$\phi^N(t,\lambda) = \phi^P(t,\lambda)b(\lambda) + \bar{\phi}^P(t,\lambda)a(\lambda) \qquad (2.19a)$$
$$\bar{\phi}^N(t,\lambda) = \phi^P(t,\lambda)\bar{a}(\lambda) + \bar{\phi}^P(t,\lambda)\bar{b}(\lambda), \qquad (2.19b)$$

with coefficients $a(\lambda)$, $b(\lambda)$, $\bar{a}(\lambda)$ and $\bar{b}(\lambda)$. These coefficients are called *scattering coefficients* and are time invariant. In order to not overburden the notation, the explicit space dependence was omitted. As it will be shown in the following sections, from the knowledge of the scattering coefficients, it is possible to reconstruct the signal $q(t)$ uniquely. More specifically, only the coefficients $a(\lambda)$ and $b(\lambda)$ are required given that their barred version can be derived from them [28].

The fact that the scattering coefficients are time invariant, allows computing them at an arbitrary instant of time. For example, using (2.19a) and the

boundary Jost solutions (2.16), they can be computed at $t = +\infty$. At this instant both $\phi^P(t, \lambda)$ and $\bar{\phi}^P(t, \lambda)$ are known. Moreover, it is possible to propagate $\phi^N(t, \lambda)$ from $t = -\infty$, where it is known, to $t = +\infty$ by integrating (2.12a). Given the particular structure of the Jost solutions it results that the first two scattering coefficients are given by:

$$a(\lambda) = \lim_{t \to +\infty} \left[\phi_1^N(t, \lambda) \bar{\phi}_1^P(t, \lambda)^{-1} \right] \tag{2.20a}$$

$$b(\lambda) = \lim_{t \to +\infty} \left[\phi_2^N(t, \lambda) \phi_2^P(t, \lambda)^{-1} \right], \tag{2.20b}$$

where the subscript indicates the components of the Jost solution. Using (2.16) gives

$$a(\lambda) = \lim_{t \to +\infty} \phi_1^N(t, \lambda) e^{i\lambda t} \tag{2.21a}$$

$$b(\lambda) = \lim_{t \to +\infty} \phi_2^N(t, \lambda) e^{-i\lambda t}. \tag{2.21b}$$

When $\lambda \in \mathbb{R}$ the Jost solutions are bounded, so that the projection equations (2.19) are well-defined and so are the scattering coefficients. The spectral parameters $\lambda \in \mathbb{R}$ form the continuous spectrum of the Lax operator and are often called *nonlinear frequencies.*

When instead λ has non-zero imaginary part, either one of the Jost solutions $\{\phi^P(t, \lambda), \ \bar{\phi}^P(t, \lambda)\}$ diverge as $t \to +\infty$. If we consider $\lambda \in \mathbb{C}^+$ (upper half complex plane), in order to ensure that $\phi^N(t, \lambda)$ in (2.19a) is not divergent we need the condition $a(\lambda) = 0$. $a(\lambda)$ can be extended analytically over the upper half complex plane, and this fact guarantees that $a(\lambda)$ has a finite set of zeros that corresponds to the discrete eigenvalues of the problem (2.12a) [25, 68]. The condition $a(\lambda) = 0$ defines a discrete spectrum of N eigenvalues $\{\lambda_i, i = 1, \ldots, N\}$ of the Lax operator. If λ_i is an eigenvalue also its complex conjugate is an eigenvalue [28]. For this reason, considering only the eigenvalues in the upper half complex plane provides full knowledge on the spectrum of the Lax operator. The scattering coefficients corresponding to the discrete eigenvalues can be computed from (2.19a), which under the condition $a(\lambda) = 0$ is well-defined, and they results in

$$a(\lambda_i) = 0 \tag{2.22a}$$

$$b(\lambda_i) = \lim_{t \to +\infty} \phi_2^N(t, \lambda_i) e^{-i\lambda_i t}. \tag{2.22b}$$
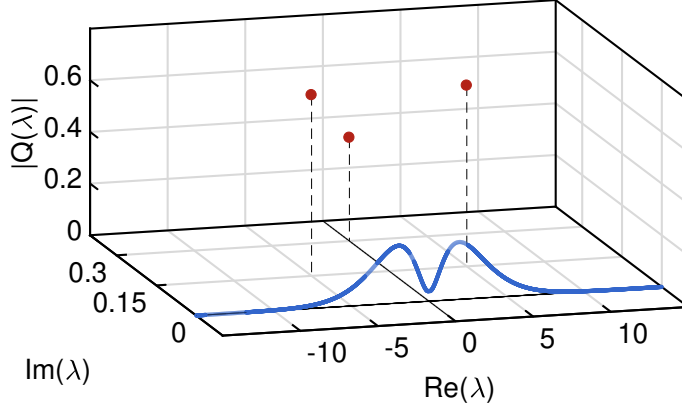
Figure 2.4: Absolute value of the continuous (blue) and discrete (red) spectral amplitudes corresponding to the nonlinear frequencies $\lambda \in \mathbb{R}$ and the discrete eigenvalues $\lambda_i \in \mathbb{C}^+, i = 1, 2, 3$.

Nonlinear spectrum The scattering data are often expressed in terms of continuous spectral amplitudes (also called spectral functions [28] or reflection coefficients [68]) as follows

$$Q_c(\lambda) = \frac{b(\lambda)}{a(\lambda)} \qquad \lambda \in \mathbb{R} \tag{2.23}$$

and discrete spectral amplitudes (also called norming constants [68])

$$Q_d(\lambda_i) = \frac{b(\lambda_i)}{a'(\lambda_i)} \qquad \lambda_i \in \mathbb{C}^+, i = 1, \dots, N \tag{2.24}$$

with $a'(\lambda_i) = \frac{da(\lambda)}{d\lambda}|_{\lambda=\lambda_i}$ such that $a(\lambda_i) = 0 \ \forall \ \lambda_i \in \mathbb{C}^+, i = 1, \dots, N$.

The continuous and discrete spectral parameters λ, together with their associated spectral amplitudes, form the *nonlinear spectrum* of the signal $q(t, z)$. The discrete nonlinear spectrum of the signal is associated with the non-dispersive solitonic components of the signal, while the continuous one with the dispersive (or radiative) waves. A representation of the nonlinear spectrum composed by both the continuous and discrete part of a signal is shown in Figure 2.4.

In a more strict mathematical sense though, the term *spectrum*, composed of a continuous and discrete part, is the set of λ that form the spetrum of the Lax operator $\boldsymbol{L}$ [25, 77], but in the recent NFT literature [29, 45, 71] the term
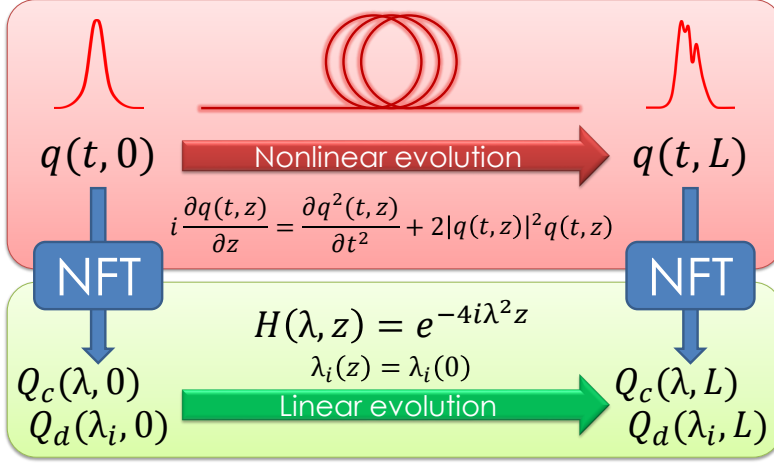
Figure 2.5: Nonlinear evolution of the signal $q(t, z)$ in the time domain and corresponding evolution of the associated nonlinear spectrum in the nonlinear domain.

assumed a broader meaning. This is justified though by the parallelism with the Fourier transform. Indeed, it can be proved that when the power of the signal $q(t, z)$ asymptotically approaches zero, the NFT continuous spectrum converges to the linear Fourier spectrum and the discrete spectrum vanishes [71]. This justifies also the term nonlinear frequencies used to refer to the continuous spectral parameters λ; these are related to the Fourier frequencies f by the relation $\lambda = -\pi f$ [71].

In the context of the NFDM systems, it is more convenient to work directly with the scattering coefficients $a(\lambda)$ and $b(\lambda)$ [57, 78]; hence, in the rest of the manuscript, we use the term *nonlinear spectrum* in an even broader sense to refer to the spectral parameters λ and the associated scattering data, being them either the spectral amplitudes or the scattering coefficients.

Spatial evolution The spatial evolution of the scattering coefficients can be derived from (2.12b) and results in [68]

$$a(\lambda, z) = a(\lambda, 0) \qquad\qquad \bar{a}(\lambda, z) = \bar{a}(\lambda, 0) \qquad\qquad (2.25a)$$

$$b(\lambda, z) = b(\lambda, 0)e^{-4i\lambda^2 z} \qquad \bar{b}(\lambda, z) = \bar{b}(\lambda, 0)e^{4i\lambda^2 z}. \qquad (2.25b)$$

The fact that the spatial evolution of the scattering coefficients is linear is a crucial property of the inverse scattering method because it reveals the

"hidden" linearity of the NLSE. Equation (2.25) plays the same role that (2.9) plays in the linear Fourier method, and it has a similar structure. From the evolution of the scattering coefficients we can also derive the spatial evolution for the spectral amplitudes, which is given by

$$Q_c(\lambda, z) = Q_c(\lambda, 0)e^{-4i\lambda^2 z} \qquad\qquad \lambda \in \mathbb{R} \qquad\qquad\qquad (2.26a)$$

$$Q_d(\lambda_i, z) = Q_d(\lambda_i, 0)e^{-4i\lambda_i^2 z} \qquad\qquad \lambda_i \in \mathbb{C}^+, i = 1, \ldots, N. \qquad (2.26b)$$

For convenience we can define the nonlinear domain transfer function of the channel modeled by the NLSE as

$$H(\lambda, z) = e^{-4i\lambda^2 z}. \qquad\qquad\qquad (2.27)$$

Figure 2.5 depicts the relation between the time domain signal and the nonlinear spectrum, and it shows their respective evolutions in space.

2.3.5   Inverse nonlinear Fourier transform

The last step required to completely define the inverse scattering method is to define the INFT in order to reconstruct a signal from its nonlinear spectrum. This operation can be performed using different approaches. When the nonlinear spectrum is purely continuous, solving the Gelfand-Levitan-Marchenko (GLM) integral equations is one of the most used approaches [71], whereas when the spectrum is purely discrete, the Darboux transformation (DT) is often employed [74]. Many other methods, such as solving the Riemann-Hilbert system or the Hirota bilinearization scheme, are also present in the literature [28]. In the general case where the spectrum is a mixture of continuous and discrete parts, combinations of some of the above methods are also possible [43].

The work presented in this thesis addresses systems where the information is encoded in the discrete nonlinear spectrum, focusing on the DT as INFT method. The INFT based on the DT for eigenvalue communications was proposed in [79]. The method consists in adding iteratively discrete eigenvalues to the nonlinear spectrum while simultaneously updating the signal in the time domain. The Darboux theorem is now reviewed, and then it is used in a procedure to perform the INFT.

Let v be a column vector solution of the ZSP (2.12a) for the signal $q(t)$ and the eigenvalue λ. In brief, the Darboux theorem [80] states that we can construct a new solution $\tilde{q}(t)$ of the NLSE, whose discrete nonlinear spectrum

is the the spectrum of $q(t)$ together with a new eigenvalue λ_0. Moreover, the theorem also provides the new solutions $\widetilde{v}$ of the ZSP (2.12a) associated to the new field $\widetilde{q}(t)$. More precisely the theorem states that a solution $\widetilde{v}$ of (2.12a) for λ and the modified field $\widetilde{q}(t)$, can be constructed using the DT, defined as follows

$$\widetilde{v} = (\lambda \mathbf{I}_2 - \mathbf{G}_0)\, v, \tag{2.28}$$

where $\mathbf{I}_2$ is the 2×2 identity matrix, $\mathbf{G}_0 = \mathbf{\Theta} \mathbf{M}_0 \mathbf{\Theta}^{-1}$ with

$$\mathbf{\Theta} = \begin{pmatrix} \bar{v}_1 & \bar{v}_2^* \\ \bar{v}_2 & -\bar{v}_1^* \end{pmatrix} \tag{2.29}$$

and where $\mathbf{M}_0 = \mathrm{diag}(\lambda_0,\ \lambda_0^*)$ and $\bar{v} = (\bar{v}_1,\ \bar{v}_2)^T$ is a solution of (2.12) for the seed signal $q(t)$ and the spectral parameter λ_0. The Darboux theorem provides also the new signal in the time domain $\widetilde{q}(t)$ as a function of the old signal $q(t)$, of the auxiliary solution $\bar{v}$, and of the spectral parameter λ_0

$$\widetilde{q}(t) = q(t) + 2i(\lambda_0^* - \lambda_0)\frac{\bar{v}_2^* \bar{v}_1}{|\bar{v}_1|^2 + |\bar{v}_2|^2}. \tag{2.30}$$

The spectral parameter λ_0 is an eigenvalue for $\widetilde{q}(t)$.

Using the Darboux theorem is possible to develop a recursive procedure, which, starting from the "vacuum" solution $q(t) = 0$, builds the signal associated to a discrete nonlinear spectrum containing an arbitrarily large number of discrete eigenvalues. The procedure is sketched in Figure 2.6 and a pseudocode is reported in Algorithm 1. At the step $i = 1, \ldots, N$ of the procedure, where N is the total number of eigenvalues, the time domain signal $q^{(i-1)}(t)$ is updated using (2.30) and the auxiliary solution $\bar{v}^{(i)}$. Moreover the auxiliary solutions $\bar{v}^{(k)}, k = i+1, \ldots, N$ are transformed according to (2.28). The generic auxiliary solution $\bar{v}^{(k)}$ that satisfies the ZSP for the eigenvalue λ_k reads: $\bar{v}^{(k)} = (A^{(k)}e^{-i\lambda_k t},\ B^{(k)}e^{i\lambda_k t})$ (being $\{A^{(k)},\ B^{(k)}\}$ some initialization constants). Hence after adding i eigenvalues the auxiliary solutions are modified according to the following chain of matrix multiplications

$$\begin{pmatrix} \widetilde{\bar{v}}_1^{(k)} \\ \widetilde{\bar{v}}_2^{(k)} \end{pmatrix} = (\lambda_k \mathbf{I}_2 - \mathbf{G}_{0i}) \ldots (\lambda_k \mathbf{I}_2 - \mathbf{G}_{01}) \begin{pmatrix} A^{(k)}e^{-i\lambda_k t} \\ B^{(k)}e^{i\lambda_k t} \end{pmatrix}, \tag{2.31}$$

where the $\mathbf{G}_{0i}$ matrices are evaluated as a function of the i-th auxiliary solution $\bar{v}^{(i)}$ evaluated after $i - 1$ DTs (see also the scheme depicted in Figure 2.6).
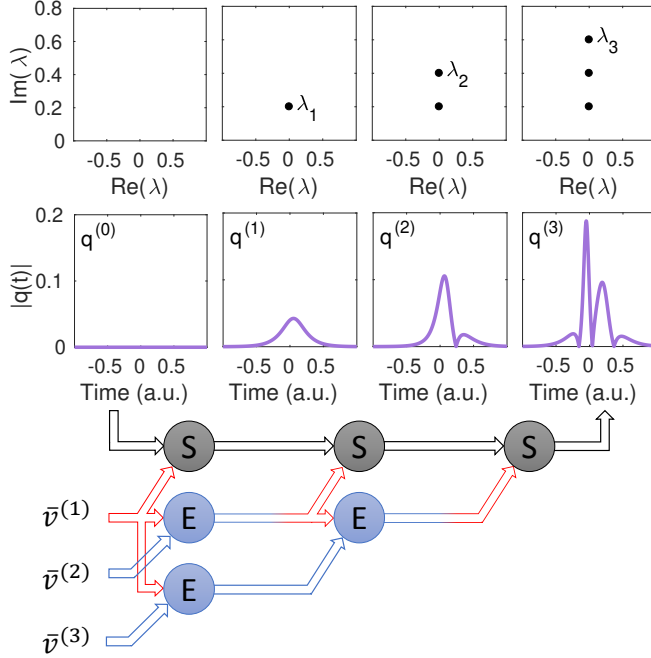
Figure 2.6: Schematic of the DT. The S-node is the signal update operation
corresponding to (2.30), and the E-node is the eigenvector up-
date operation corresponding to (2.28). At the step $i = 1, 2, 3$
the auxiliary solution $\bar{v}^{(i)}$ for $\lambda = \lambda_i$ (red arrow) modifies the
signal $q^{(i-1)}(t)$ and the auxiliary solutions $\bar{v}^{(k)}, k = i + 1, \ldots, 3$
(blue arrows).

The Darboux theorem states how to add eigenvalues to the spectrum of
the signal but says nothing about the spectral amplitudes. The spectral am-
plitudes associated to the eigenvalue $i = 1, \ldots, N$ are controlled by the initial-
ization constants $\{A^{(i)}, B^{(i)}\}$ through the following relation [81]

$$Q_d(\lambda_i) = (\lambda_i - \lambda_i^*) \prod_{k=1, k \neq i}^{N} \frac{\lambda_i - \lambda_k^*}{\lambda_i - \lambda_k} \times \frac{-B_i}{A_i}. \qquad (2.32)$$

By arbitrarily setting $A_i = 1$ for simplicity, the other initialization constant for
the eigenvalue λ_i can be obtained from an arbitrary chosen spectral amplitude

---

Algorithm 1 Inverse nonlinear Fourier transform by Darboux transformation

---

1: **procedure** $\text{INFT}(\lambda_1, \ldots, \lambda_N, b(\lambda_1), \ldots, b(\lambda_N))$

2:      $q(t) \leftarrow 0$ ▷ The signal is initialized to be identically zero

3:      **for** $i \leftarrow 1, \ldots, N$ **do**   ▷ Initialization of the N auxiliary solutions

4:          $A_i \leftarrow 1$

5:          $B_i \leftarrow -b(\lambda_i)$

6:          $\bar{v}^{(i)}(t) \leftarrow \left(A_i e^{-i\lambda_i t}, B_i e^{i\lambda_i t} \right)^T$

7:      **end for**

8:      **for** $i \leftarrow 1, \ldots, N$ **do**

9:          $q(t) \leftarrow q(t) + 2i(\lambda_i^* - \lambda_i) \dfrac{\bar{v}_2^{(i)}(t)^* \bar{v}_1^{(i)}(t)}{\left| \bar{v}_1^{(i)}(t) \right|^2 + \left| \bar{v}_2^{(i)}(t) \right|^2}$ ▷ Signal update

10:          $\boldsymbol{\Theta} \leftarrow \begin{pmatrix} \bar{v}_1^{(i)} & \bar{v}_2^{(i)*} \\ \bar{v}_2^{(i)} & -\bar{v}_1^{(i)*} \end{pmatrix}$

11:          $\mathbf{M}_0 \leftarrow \text{diag}(\lambda_i, \ \lambda_i^*)$

12:          $\mathbf{G}_0 \leftarrow \boldsymbol{\Theta} \mathbf{M}_0 \boldsymbol{\Theta}^{-1}$

13:          **for** $k \leftarrow i + 1, \ldots, N$ **do**

14:              $\bar{v}^{(k)}(t) \leftarrow (\lambda_k \mathbf{I}_2 - \mathbf{G}_0) \, \bar{v}^{(k)}(t)$ ▷ Auxiliary solution update

15:          **end for**

16:      **end for**

17:      **return** $q(t)$

18: **end procedure**

$Q_d(\lambda_i)$ as

$$B_i = -\frac{1}{\lambda_i - \lambda_i^*} \prod_{k=1, k \neq i}^{N} \frac{\lambda_i - \lambda_k}{\lambda_i - \lambda_k^*} \times Q_d(\lambda_i). \tag{2.33}$$

If instead of defining the nonlinear spectrum in terms of spectral amplitudes, we define it in terms of the scattering coefficient $b(\lambda_i)$, the relation with the initialization constants assumes the very simple form

$$A_i = 1, \qquad B_i = -b(\lambda_i). \tag{2.34}$$

The DT with the initialization conditions just presented defines a INFT procedure that properly builds time domain signals from an arbitrary discrete nonlinear spectrum.

2.3.6   Relation between the discrete spectrum and the signal in the time domain

In the previous sections the ZSP was introduced and it was shown how to use the direct NFT to solve it in order to compute the nonlinear spectrum. From that it is clear that the nonlinear spectrum has not an intuitive interpretation as opposed to the Fourier spectrum. The analytical relation between the nonlinear spectrum and the corresponding time domain signal is not available in general, but it is known for a few specific cases. It is worth analyzing one of these cases to grasp an intuition of how changing the nonlinear spectrum affects the time domain signal.

Considering the case of a nonlinear spectrum composed by a single eigenvalue λ_1 and null continuous spectrum, the complex envelope of the electric field of the signal can be written as a function of the nonlinear spectrum as follows [68]

$$
\begin{aligned}
q(t,0) =& 2\operatorname{Im}(\lambda_1)\operatorname{sech}\left(2\operatorname{Im}(\lambda_1)(t-t_1)\right) \\
&\times \exp\left(-i\left(2\operatorname{Re}(\lambda_1)t + \underline{/Q_d(\lambda_1)} + \pi/2\right)\right),
\end{aligned}
\tag{2.35}
$$

where

$$
t_1 = \frac{1}{2\operatorname{Im}\{\lambda_1\}}\log\left(\frac{|Q_d(\lambda_1)|}{2\operatorname{Im}\{\lambda_1\}}\right).
\tag{2.36}
$$

Few things can be noted from this relation:

- the amplitude of the signal, and so its power, is related to the imaginary part of the eigenvalue, while it is independent on the discrete spectral amplitude $Q_d(\lambda_1)$

- the time width of the pulse is inversely proportional to the imaginary part of the eigenvalue and so its bandwidth is proportional to it

- the phase of $q(t)$ is proportional to the phase of $Q_d(\lambda_1)$

- the pulse delay t_1 is proportional to the logarithm of the absolute value of the discrete spectral amplitude $Q_d(\lambda_1)$. If the spectral amplitude has a radius greater than $2\operatorname{Im}\{\lambda_1\}$ the soliton is retarded, and if it has a radius smaller than that it is advanced with respect a $\operatorname{sech}(t)$ pulse

- the real part of the eigenvalue represents the frequency of the soliton, which determines its propagation velocity in the optical fiber.
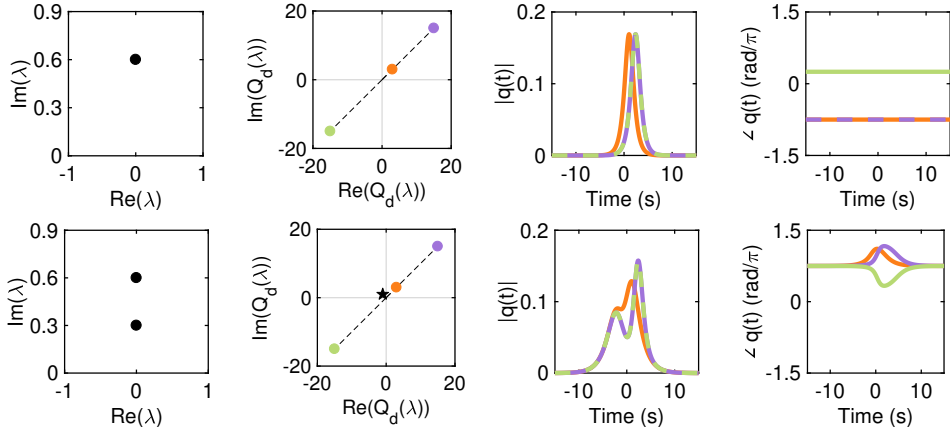
Figure 2.7: Example of nonlinear spectra composed of (**top**) one eigenvalue $\lambda_1 = i0.6$ and (**bottom**) two eigenvalues ($\lambda_1 = i0.3, \lambda_2 = i0.6$) for three different values of the spectral amplitude $Q_d(\lambda_1)$ and $Q_d(\lambda_2)$, respectively. The corresponding time domain signal in the normalized regime (in terms of absolute value and phase) is displayed on the right.

In Figure 2.7 (top) an example of single eigenvalue nonlinear spectrum and its corresponding time domain signal are shown for three different values of the spectral amplitude $Q_d(\lambda_1)$. Increasing the absolute value of $Q_d(\lambda_1)$ from 3 (orange) to 15 (violet) the signal is shifted to the right by $1.34\,\text{s}$. Rotating the phase of $Q_d(\lambda_1)$ by $\pi\,\text{rad}$ (green) rotates the phase of the signal by the same amount.

When the discrete nonlinear spectrum contains more than one eigenvalue the resulting time domain signal is, in general, a nonlinear combination of fundamental solitons through the ZSP, so that the roles played by the eigenvalues and the spectral amplitudes still apply to the components of the multi-soliton [25]. Though, when the components are mixed the relation between the nonlinear spectrum and time domain signal is less evident than the single eigenvalue case. For example, in Figure 2.7 (bottom) the relation is illustrated for a nonlinear spectrum with two eigenvalues. In this case changing the absolute value of $Q_d(\lambda)[2]$ from 3 (orange) to 15 (violet) shifts the corresponding solitonic component to the right as in the single eigenvalue case. Rotating the phase of $Q_d(\lambda)[2]$ by $\pi\,\text{rad}$ (green) does not change the phase of the whole signal, but only of a portion of it, and the rotation amount varies along the portion.

In the next chapter, the relation among the components of the nonlinear spectrum and the properties of the time domain signal is used to discuss some design aspects of the NFDM systems.

2.4   Nonlinear Fourier transform in the presence of loss and noise

As mentioned in Section 2.2, the channel model described by the scalar NLSE in (2.1) is a simplistic one and does not properly describe the real fiber-optic channels. Among the effects not considered, there are the optical fiber intrinsic loss and the noise. A more accurate model that accounts for these two effects is given by the following generalized version of the scalar NLSE

$$\frac{\partial E(\tau, \ell)}{\partial \ell} = -i\frac{\beta_2}{2}\frac{\partial^2 E(\tau, \ell)}{\partial \tau^2} + g(\ell)E(\tau, \ell) + i\gamma|E(\tau, \ell)|^2 E(\tau, \ell) + n(\tau, \ell). \quad (2.37)$$

The term $n(\tau, \ell)$ is the noise, and it is assumed to be zero-mean additive white Gaussian noise (AWGN). It is fully characterized by its spectral power density N_0, or equivalently by its autocorrelation function

$$\mathbb{E}[n(\tau, \ell)n^*(\tau, \ell)] = N_0\delta(\tau - \tau')\delta(\ell - \ell'), \quad (2.38)$$

where $\mathbb{E}[\cdot]$ is the expectation, and $\delta(\cdot)$ the Dirac delta-function. The term $g(\ell)$ is the gain-loss profile

$$g(\ell) = -\frac{\alpha}{2} + g'(\ell), \quad (2.39)$$

and it is given by a combination of the loss, characterized by the fiber-loss parameter α and the gain profile $g'(\ell)$, which depends on the amplification scheme used. We assume that the fiber link is divided in spans of length L_s with the same amplification scheme applied to each span.

By using advanced amplification techniques, such as ultra-long fiber lasers distributed Raman amplification [82], it is possible to obtain a flat gain profile over the entire link thus making $g(\ell) \simeq 1$. In this way it is possible to make (2.37) very close to the ideal lossless NLSE, but perturbed by noise. When EDFA amplification is used instead, we have $g(\ell) = -\frac{\alpha}{2}$ for $0 < \ell < L_s$, where L_s is the length of the fiber between two amplifiers.

The presence of the two new terms makes (2.37) not integrable so that the inverse scattering method does not provide exact analytical solutions anymore.

Nonetheless, if we could bring (2.37) to a form that resemble the lossless NLSE we could still define the NFT. If this approximate NFT behaves similarly to the ideal one, we could still use it to encode data and exploits its linearity properties. This is indeed possible and can be achieved by the following procedure [70].

Starting from (2.37) we perform the change of variable

$$\tilde{E}(\tau, \ell) \leftarrow E(\tau, \ell) G(\ell)^{\frac{1}{2}}, \tag{2.40}$$

where

$$G(\ell) = \exp\left(2 \int_0^\ell g(\ell') d\ell'\right). \tag{2.41}$$

In this way we obtain a NLSE in the same form of (2.1)

$$\frac{\partial \tilde{E}(\tau, \ell)}{\partial \ell} = -i\frac{\beta_2}{2}\frac{\partial^2 \tilde{E}(\tau, \ell)}{\partial \tau^2} + i\gamma(\ell)\left|\tilde{E}(\tau, \ell)\right|^2 \tilde{E}(\tau, \ell) + n(\tau, \ell), \tag{2.42}$$

with a space dependent nonlinear parameter

$$\gamma(\ell) = \gamma G(\ell). \tag{2.43}$$

By averaging this parameter over one span length as

$$\bar{\gamma} = \frac{1}{L_s} \int_0^{L_s} \gamma(\ell) d\ell, \tag{2.44}$$

we can write the lossless path-averaged (LPA) NLSE [70, 83] as

$$\frac{\partial \tilde{E}(\tau, \ell)}{\partial \ell} = -i\frac{\beta_2}{2}\frac{\partial^2 \tilde{E}(\tau, \ell)}{\partial \tau^2} + i\bar{\gamma}\left|\tilde{E}(\tau, \ell)\right|^2 \tilde{E}(\tau, \ell) + n(\tau, \ell). \tag{2.45}$$

The evolution equation with the modified nonlinear term can be considered the leading approximation of the lossy system when we account for the variable gain-loss profile along the optical fiber. The inverse scattering method can be used to solve this equation, but the obtained solutions are only an approximations of the real solutions of (2.37).

For and EDFA amplified system we have

$$\bar{\gamma} = \gamma\frac{G_a - 1}{\log(G_a)}, \qquad G_a = G(L_s) = e^{-\alpha L_s} \tag{2.46}$$

and in this case the LPA approximation precision decreases as the amplifiers spacing L_s is increased, being $\bar{\gamma}$ farther from the real γ of the fiber. In general,

in order to apply this approximation one should guarantee the condition $L_s \ll L_d$ where $L_d = (W^2|\beta_2|)^{-1}$ is the dispersion distance for the signal, and W is its bandwidth [29, 70].

In the following section, the behavior of the NFT is discussed in more detail for the case where the underlying channel is modeled by (2.37).

2.5 Accuracy of the nonlinear Fourier transform in the presence of loss and noise

The generalized channel model just presented is of particular interested because, compared to the ideal NLSE (2.1), it better describes the fiber links employing EDFA amplification, which constitute the majority of the deployed links.

Over this channel the NFT can only be defined by using the LPA approximation so that its behavior cannot be studied analytically. For this reason it is important to evaluate if the approximate NFT is "well-behaved" in practical cases. Indeed, this is the case, as proved by several numerical [48, 84] and experimental [34, 85] investigations.

This section presents the initial numerical results, based on [C3], of the behavior of the NFT spectrum over channels modeled by (2.37). The effect of some system parameters (launched signal power, fiber attenuation, and AWGN) on the NFT continuous spectrum are numerically analyzed in detail, and a comparison of how the same parameters influence the linear spectrum (discrete Fourier transform (DFT)), which is used as a reference, is given. In particular, a simple scenario of a single isolated Gaussian pulse propagating in a SMF is considered; the difference between its continuous nonlinear spectrum before and after the transmission is measured in terms of normalized mean squared error (NMSE).

The results show that the continuous nonlinear spectrum preserves itself better along the transmission link when compared to the DFT spectrum, regardless of the presence of non-idealities such as fiber loss and noise. This confirmed once more that the NFT is a promising technique in scenarios where the spectrum preservation is desirable, such as multi-channel systems using frequency-orthogonal channels.
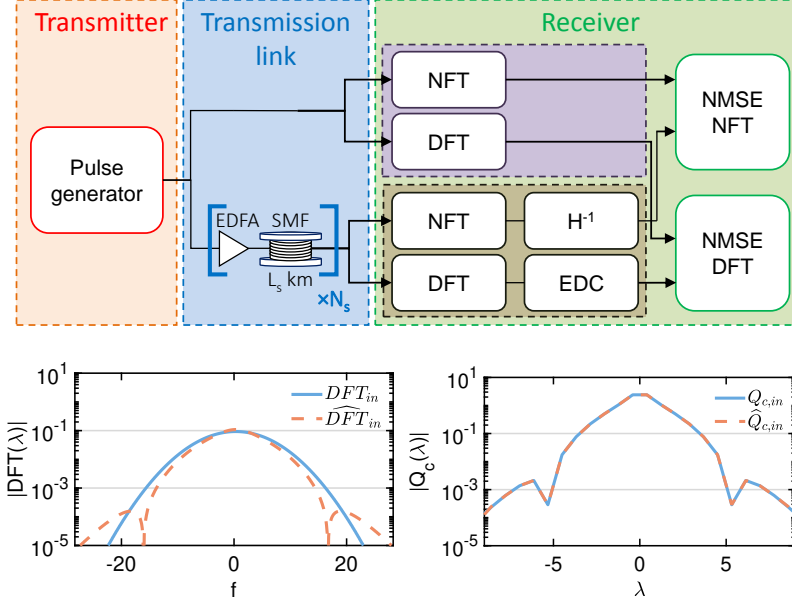
Figure 2.8: (**top**) Simulation setup implemented in MATLAB™ and VPI Transmission Maker™. (**bottom**) NFT and DFT spectra at input and output of the fiber lossless channel.

In the following, first the numerical setup is introduced and the metric used to carry out the investigation is defined, then the numerical results are presented.

2.5.1 Simulation setup

The numerical simulation setup is depicted in Figure 2.8 and has been performed using VPI Transmission Maker™ and the MATLAB™ simulation framework Robochameleon [86]. The transmitter generates a single Gaussian pulse with 50 ps full-width half-maximum (FWHM). The simulation time window is 8 ns and the simulation bandwidth is 2.56 THz. This choice guarantees that the pulse is well isolated in order to satisfy the vanishing boundary conditions for the NFT, and to minimize the truncation error. An ideal laser with a wavelength of 1550 nm is used. The input waveform E_{in} is transmitted over a dispersion uncompensated link of 1000 km (10×100 km) SMFs. The fiber has a dispersion parameter $D = 17$ ps/(nm km) and a nonlinear parameter

$\gamma = 1.27 \, \mathrm{W}^{-1} \, \mathrm{km}^{-1}$. The fiber-loss parameter is either set to $\alpha = 0 \, \mathrm{dB/km}$ (lossless, ideal case) or $\alpha = 0.2 \, \mathrm{dB/km}$ (typical value for SMF). For the lossy channel, perfect attenuation compensation has been achieved by using EDFAs after each span. EDFAs with no noise and with a noise figure of 3 dB are considered in two different scenarios. In the simulations where the noise is present, the results have been averaged over 30 realizations and the standard error is shown with error bars. The propagation in the fiber is simulated using the split-step Fourier method (SSFM) with an adaptive step size allowing for a maximum nonlinear phase rotation of 0.01 degrees, which was chosen to guarantee the convergence of the method. At the fiber output, an ideal coherent receiver is assumed to give access to the full signal field E_{out}.

The NFT continuous spectra $Q_{c,in}(\lambda)$ and $Q_{c,out}(\lambda)$ with $\lambda \in \mathbb{R}$, of E_{in} and E_{out}, respectively, are computed using the Ablowitz-Ladik method to solve the ZSP problem as described in [87]. When the channel is lossy and EDFA amplification is employed, the NFT is computed using the LPA method previously described. To compare input and output spectra, the channel inverse transfer function $H^{-1}(\lambda, z = 1) = e^{4i\lambda^2}$ is used to compensate for the channel propagation, to obtain $\widehat{Q}_{c,in}(\lambda) = e^{4i\lambda^2} Q_{c,out}(\lambda)$. The two spectra $Q_{c,in}(\lambda)$ and $\widehat{Q}_{c,in}(\lambda)$ are then compared using the NMSE as a metric

$$\mathrm{NMSE} = \frac{\displaystyle\int_\lambda |Q_{c,in}(\lambda) - \widehat{Q}_{c,in}(\lambda)|^2 d\lambda}{\displaystyle\int_\lambda |Q_{c,in}(\lambda)|^2 d\lambda}. \tag{2.47}$$

In order to benchmark the results, linear spectra are also calculated using standard DFT and the same NMSE metric is applied. In this case electrical dispersion compensation (EDC) is applied to the DFT of E_{out} as shown in Figure 2.8.

2.5.2 Results

To investigate the impact of the fiber losses on the NFT continuous spectrum, an ideal Gaussian pulse is transmitted over a noise-free channel considering two cases: a lossless channel or with fiber-loss parameter $\alpha = 0.2 \, \mathrm{dB/km}$.

In Figure 2.9 (a) the NMSE as a function of the launched signal power is shown. In the lossless case, the DFT NMSE increases exponentially with the power due to the impact of self-phase modulation (SPM). For power levels above $-18 \, \mathrm{dBm}$, the relative error is higher than 10% making the output spectrum diverge significantly from the input one. Note that SPM impairments

Figure 2.9: (**a**) NMSE between input and output (1000 km) continuous nonlinear spectrum and linear Fourier spectrum (DFT) as a function of the launched signal power for a noiseless transmission. Fiber attenuation of 0 dB/km (light red dashed lines) and 0.2 dB/km (light blue solid lines) are compared. (**b**) Percentage of energy in the continuous nonlinear spectrum.

are already so strong at this power, because the large guard time intervals used to account for the dispersive effects significantly decrease the average power, however, nonlinear effects depend on the pulse peak power which is 22 dB higher than the average in this setup. Above −9 dBm the error flattens out to NMSE = 4, i.e., the maximum NMSE between two spectra carrying the same energy. On the other hand, the NFT NMSE remains practically constant and below a value of 2×10^{-6} for powers up to −10 dBm, while for powers above this value it slightly increases, possibly due to the numerical precision required for the computation, as above −10 dBm most of the energy is transferred from the NFT continuous spectrum to the discrete one (Figure 2.9 (b)). Nevertheless, the NMSE stays below a value of 1×10^{-4}, confirming the theoretically expected higher tolerance of the NFT to nonlinear impairments.

When the fiber loss is taken into account and compensated for by noiseless amplification, the DFT matching improves compared to the lossless case as the effective nonlinearity is lowered by the presence of the loss. Such an

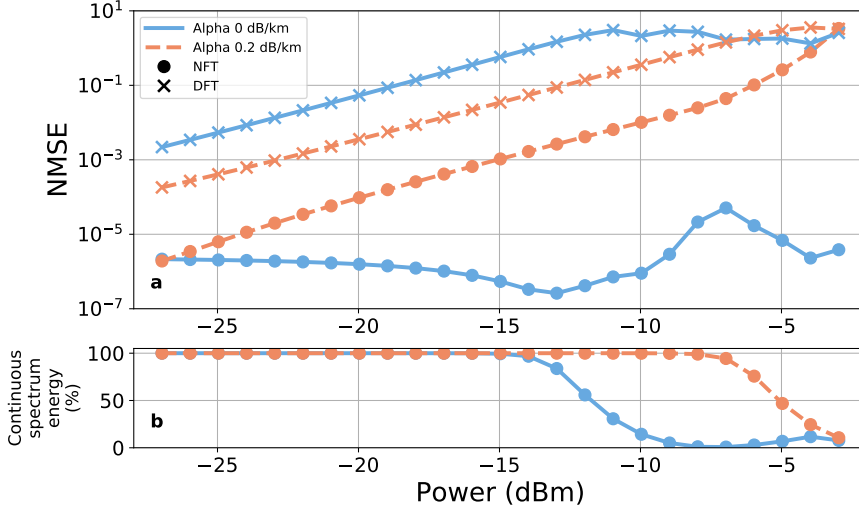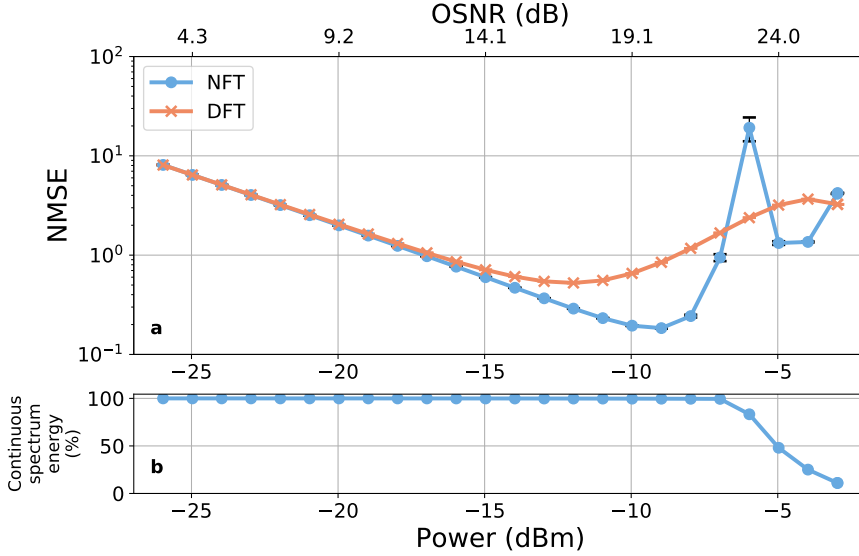**Figure 2.10:** (**a**) NMSE between input and output (1000 km) continuous nonlinear spectrum and linear Fourier spectrum (DFT) as a function of the launched signal power for a transmission over a fiber with loss of 0.2 dB/km and EDFA amplification with noise figure of 3 dB. (**b**) Percentage of energy in the continuous NFT spectrum .

improvement is not visible for the NFT that instead performs worse with respect to the lossless case due to the approximate equation used to compute the NFT when the channel is lossy and therefore non-integrable. The NMSE increments exponentially with the power, consistently with [48]. Nonetheless, the spectral mismatch between the NFT spectra is still lower than that of the linear spectrum, even in this non-ideal case.

In the last scenario considered, the impact of the power variations and the noise are evaluated simultaneously: the pulse has been transmitted over the lossy channel, and EDFAs with a noise figure of 3 dB have been used to compensate for the power loss. In Figure 2.10 (a) the dependency of the NMSE as a function of the launched signal power, and the corresponding optical signal-to-noise ratio (OSNR) at the receiver is shown.

In the linear regime, the spectral matching increases with the power (NMSE decreases) for both DFT and NFT. Once the power is increased beyond the lin-

ear transmission regime, the DFT NMSE worsens as the nonlinearity impacts the spectral matching. The behavior of the NFT is similar, but in this case, the tolerance to the nonlinearity is higher with the optimum signal launched power increased by 3 dB. For even higher power also the NFT NMSE starts worsening. This is believed to be caused by the use of the LPA approximation. Note that the peak for -6 dBm launched signal power corresponds to the point where the first discrete eigenvalue appears, i.e., the point where the NFT continuous spectrum energy is slightly different from the nonlinear spectrum total energy (Figure 2.10 (b)). Overall, the NFT provides an NMSE decreased by a factor of 2.85 compared to the DFT at the respective optimal launched signal powers, proving its potential for nonlinear transmission.

2.5.3   Conclusion

In this section the accuracy of the approximate channel model given by the LPA NLSE in the presence of fiber loss and noise has been evaluated in terms of distortion of the NFT continuous spectrum upon spatial propagation and using the linear DFT as a reference. The impact of the fiber loss on the NFT shows a worsening of the NMSE when higher launched signal powers are used. However, a lower spectral distortion in terms of NMSE between input and output spectra is reported for the NFT when compared to the DFT. Finally, when a lossy and noisy transmission is considered, an improved spectral matching can be achieved by the NFT. A decrement of the NMSE of almost three times, as well as an increment in the launched signal power by 3 dB compared to the DFT, are demonstrated. The results show that the even when using the LPA NLSE approximate channel model, it is possible to exploit the property of spectral invariance of the NFT.

2.6   Summary

In this chapter the fundamental concepts required to define an NFDM system have been introduced starting from the description of a generic coherent optical communication system and the fiber channel model given by the NLSE. The inverse scattering method used to solve the NLSE has been presented togheter with the concepts of auxiliary spectral problem and nonlinear spectrum. The three components of the inverse scattering method, the NFT, the INFT, and the spatial evolution equation of the scattering data were discussed in detail.

In the last part of the chapter, the generalized channel model described by the LPA NLSE, which accounts for the fiber loss has been introduced. A numerical analysis of the spectral distortion of the continuous nonlinear spectrum when this channel is used has also been presented to validate the channel model.

Normalized NLSE $(\beta_2 < 0$, focusing)	$iq_z - q_{tt} - 2|q|^2q = 0$
Change of variables	$q = \dfrac{E}{\sqrt{P}}, \qquad t = \dfrac{\tau}{T_0}, \qquad z = -\dfrac{\ell}{\mathcal{L}}$ T_0 free, $\qquad P = \dfrac{|\beta_2|}{\gamma T_0^2}, \qquad \mathcal{L} = \dfrac{2T_0^2}{|\beta_2|}$
L (operator)	$\begin{pmatrix} i\frac{\partial}{\partial t} & -iq \\ -iq^* & -i\frac{\partial}{\partial t} \end{pmatrix}$
P (matrix)	$\begin{pmatrix} -i\lambda & q \\ -q^* & i\lambda \end{pmatrix}$
M (matrix)	$\begin{pmatrix} 2i\lambda^2 - i|q|^2 & -2\lambda q - iq_t \\ 2\lambda q^* - iq_t^* & -2i\lambda^2 + i|q|^2 \end{pmatrix}$

Table 2.1: Normalized NLSE used in this thesis and in [28, 32, 42, 68, 69], corresponding change of variables, Lax operator $\boldsymbol{L}$, and Lax pair $\boldsymbol{P}, \boldsymbol{M}$. The standard simplified notation for the partial derivatives is used, and the explicit dependency on z and t is omitted.

Normalized NLSE $(\beta_2 < 0,\text{ focusing})$	$iq_z + \dfrac{1}{2}q_{tt} + |q|^2 q = 0$
Change of variables	$q = \dfrac{E}{\sqrt{P}}, \qquad t = \dfrac{\tau}{T_0}, \qquad z = \dfrac{\ell}{\mathcal{L}}$ $T_0 \text{ free}, \qquad P = \dfrac{|\beta_2|}{\gamma T_0^2}, \qquad \mathcal{L} = \dfrac{T_0^2}{|\beta_2|}$
L (operator)	$\begin{pmatrix} i\frac{\partial}{\partial t} & q \\ -q^* & -i\frac{\partial}{\partial t} \end{pmatrix}$
P (matrix)	$\begin{pmatrix} -i\lambda & iq \\ iq^* & i\lambda \end{pmatrix}$
M (matrix)	$\begin{pmatrix} i\lambda^2 + \frac{i}{2}|q|^2 & i\lambda q - \frac{1}{2}q_t \\ i\lambda q^* + \frac{1}{2}q_t^2 & i\lambda^2 - \frac{i}{2}|q|^2 \end{pmatrix}$

Table 2.2: Normalized NLSE used in [7, 23, 70–72], corresponding change of variables, Lax operator $\boldsymbol{L}$, and Lax pair $\boldsymbol{P}, \boldsymbol{M}$. The standard simplified notation for the partial derivatives is used, and the explicit dependency on z and t is omitted.

Normalized NLSE ($\beta_2 < 0$, focusing)	$iq_z + q_{tt} + 2|q|^2 q = 0$
Change of variables	$q = \dfrac{E}{\sqrt{P}}, \qquad t = \dfrac{\tau}{T_0}, \qquad z = \dfrac{\ell}{\mathcal{L}}$ T_0 free, $\qquad P = \dfrac{|\beta_2|}{\gamma T_0^2}, \qquad \mathcal{L} = \dfrac{2T_0^2}{|\beta_2|}$
L (operator)	$\begin{pmatrix} i\frac{\partial}{\partial t} & -iq \\ -iq^* & -i\frac{\partial}{\partial t} \end{pmatrix}$
P (matrix)	$\begin{pmatrix} -i\lambda & q \\ -q^* & i\lambda \end{pmatrix}$
M (matrix)	$\begin{pmatrix} -2i\lambda^2 + i|q|^2 & 2\lambda q + iq_t \\ -2\lambda q^* + iq_t^* & 2i\lambda^2 - i|q|^2 \end{pmatrix}$

Table 2.3: Normalized NLSE used in [24, 73, 74], corresponding change of variables, Lax operator $\boldsymbol{L}$, and Lax pair $\boldsymbol{P}, \boldsymbol{M}$. The standard simplified notation for the partial derivatives is used, and the explicit dependency on z and t is omitted.

CHAPTER 3

Nonlinear frequency division multiplexing

In this chapter a detailed description of the structure of an nonlinear frequency division multiplexing (NFDM) transmission system is given, with a particular focus on the case where only the discrete nonlinear spectrum is modulated. The aim is to provide an overview of NFDM, discussing some of the peculiar problems in building such systems, as well as providing a brief overview of the state-of-the-art methods proposed to overcome some of these limitations.

The name NFDM was first introduced in [28, 79] to reflect the conceptual similarity with orthogonal frequency-division multiplexing (OFDM). In an OFDM system, the information is encoded in multiple orthogonal subcarriers to avoid inter-symbol interference (ISI) and inter-channel interference over linear channels [88]. More specifically, the data bits are encoded on the Fourier coefficients corresponding to a discrete set of fixed frequencies (subcarriers) using standard modulation formats (e.g., phase-shift keying (PSK), quadrature amplitude modulation (QAM), etc.). Similarly, an NFDM system employs orthogonal degrees of freedom of a signal that can be modulated together without leading to mutual interference when propagated in the nonlinear fiber channel [28].

To better clarify this idea, it is first worth considering the situation where only the continuous nonlinear spectrum is used, so that the analogy with OFDM is one-to-one. In this case, the modulated quantities are the continuous spectral amplitudes $Q_c(\lambda)$ associated to a finite set of nonlinear frequencies $\{\lambda_1, \ldots, \lambda_K\}$ and chosen from the continuous set of $\lambda \in \mathbb{R}$. In the NFDM case, however, the "frequencies" λ can also assume complex values, in which case are referred to as discrete eigenvalues, thus allowing to modulate also the associated discrete spectral amplitudes $Q_d(\lambda_i)$. In this sense the NFDM scheme can be seen as an extension of OFDM, where more degrees of freedom are available for carrying data.

NFDM is only one of the possible *modulations in the nonlinear Fourier domain*, in the sense of a modulation where the information is encoded in the nonlinear domain [29]; however, as it was mentioned in the introduction, other types of modulations exists, e.g., eigenvalue position modulation [23, 30, 89] or nonlinear inverse synthesis (NIS) [90].

The two distinctive characteristics of NFDM are:

- to have a fixed number of λ, real or complex, at specific locations

- to have data encoded in either the spectral amplitudes $Q_c(\lambda), Q_d(\lambda_i)$ (or equivalently in the scattering coefficients $b(\lambda)$) corresponding to the set of λ chosen

In the rest of this chapter, the structure of a single channel NFDM system employing only the discrete spectrum is described. The focus is mainly on the digital signal processing (DSP) required for the implementation of the system. The NFDM transmitter is presented in Section 3.1. In particular, in Section 3.1.1 the bit mapper is described, and some constellation design aspects are discussed. Then in Section 3.1.2 some possible implementations of the inverse nonlinear Fourier transform (INFT), required to convert the symbols into a digital time domain signal, are presented. Next, in Section 3.1.3, the denormalization operation, required to match the normalized signal to the real fiber-channel, is explained. In Section 3.1.4 some problems caused by the distortion introduced by the transmitter components are discussed, and some solutions present in the literature are reviewed. In the second part of this chapter, the NFDM receiver is introduced in Section 3.2. First the operations performed on the time domain signal are described; these includes power rescaling (Section 3.2.1), signal filtering (Section 3.2.2), and clock recovery and time synchronization (Section 3.2.3). These operations prepare the signal for the nonlinear Fourier transform (NFT) block (Section 3.2.4), which computes the nonlinear spectrum. Finally the operations performed in the nonlinear domain are described; these are the phase estimation (Section 3.2.5), and symbol decision and data bit recovery (Section 3.2.6).

3.1 Transmitter

Figure 3.1 illustrate the structure of the NFDM transmitter together with the specific transmitter DSP chain. As it can be seen, the structure is the same of the generic coherent system presented in Section 2.1.
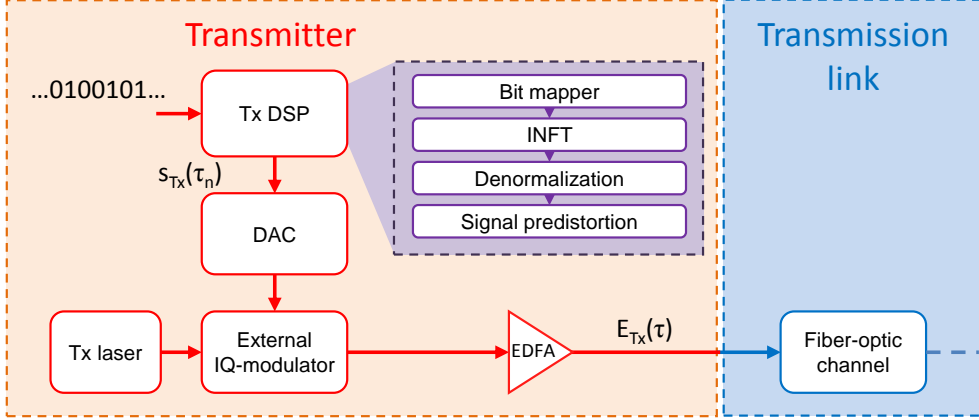
Figure 3.1: Block diagram of the NFDM transmitter.

The first block of the NFDM transmitter is the transmitter DSP, whose function is to convert a stream of data bits to a discrete-time signal $E_{Tx,i}(\tau_n)$. NFDM is a block transmission as OFDM, meaning that in the i-th symbol period $T_{s,i}$, the transmitter modulates a block of d bits onto a waveform $E_{Tx,i}(\tau_n)$. This waveform has a duration of T_s seconds, including the null guard bands required to satisfy the vanishing boundary conditions of the NFT. The generated waveforms are then concatenated to form the full signal $E_{Tx}(\tau_n) = \sum_{i=-\infty}^{+\infty} E_{Tx,i}(\tau_n)$. The digital-to-analog converter (DAC) converts this signal to its analog equivalent, which is then used to drive an external optical modulator. The modulator shapes a continuous wave laser to generate the continuous-time optical signal $E_{Tx}(\tau)$. The power of the waveform is regulated by an optical amplifier, and then the waveform is transmitted through the nonlinear channel.

In the following sections, all the blocks of the DSP chain are described in detail.

3.1.1 Bit mapper and constellation design

The purpose of the bit mapper is to map the binary digital data stream $\{b_l\}$ of period T_b to a sequence of symbols in the nonlinear domain. Most of the works in the literature employing discrete NFDM systems use different values of the discrete spectral amplitudes $Q_d(\lambda_i) = b(\lambda_i)/a'(\lambda_i)$ [34, 41] as symbol
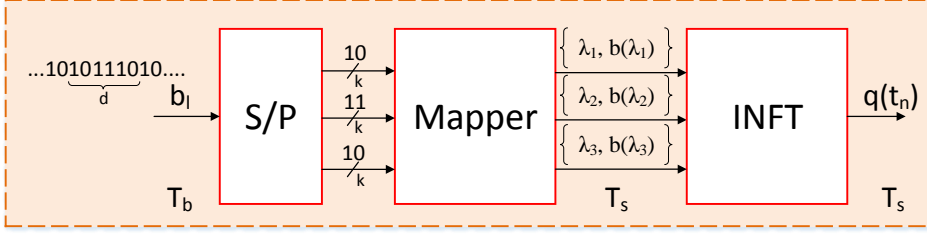
Figure 3.2: NFDM bit mapper and INFT block.

alphabet. Recently though, it was shown that it is better to encode the data directly on the $b(\lambda_i)$ scattering coefficient. This allows reducing the noise on the symbols caused by numerical errors [81] and by the noise component of $a'(\lambda_i)$ [57]. In this thesis this last approach is used, given the advantages it offers.

The architecture of the NFDM digital modulator is illustrated in Figure 3.2. A serial-to-parallel (S/P) converter partitions the data binary sequence in blocks of length d, each of which constitutes a single data frame. Each block is further subdivided in N sub-blocks of length $k = d/N$, where N is the number of eigenvalues λ_i used. Each of the k bits of the sub-block i are mapped to one of the $M = 2^k$ possible complex values of the scattering coefficient $b(\lambda_i)$, associated to the discrete eigenvalue $\lambda_i, i = 1, \ldots, N$, using for example the Grey mapping [67]. It was implicitly assumed that all the constellations have the same order M, even though this is not a constraint.

The set of eigenvalues and corresponding scattering coefficients output by the NFDM bit mapper constitute an NFDM-symbol of period T_s, which can be written as $\mathbf{s} = \{\lambda_1, \ldots, \lambda_N, b(\lambda_1), \ldots, b(\lambda_N)\}$. This symbol is passed to the INFT block that converts it to a waveform.

The choice of the number and location of the eigenvalues, and of the order M and shape of the $b(\lambda_i)$ constellations defines what in this thesis is referred to as the *modulation format* of the NFDM system. Given some system design constraints, such as available power and bandwidth, duration of the time domain signal, or desirable spectral efficiency, the choice of the modulation format is in general a complex problem in the NFDM case. This is due to the complicated relation between the nonlinear spectrum and the time domain waveform. In the following sections the problems of placing the eigenvalues

and deciding the constellations to use are discussed more in detail.

Eigenvalues placement   The position of the eigenvalues on the complex plane is an important aspect in the design of an NFDM system. Indeed, it influences the bandwidth and power of the time domain signal $q(t)$, as we discussed in Section 2.3.6, and it can also affect the symbol rate of the system.

In particular, the real part of the eigenvalue determines the frequency of the solitonic component of the time domain signal associated to that eigenvalue. From this we can infer that spreading the eigenvalues along the real axis direction gives rise to a time domain signal with an overall broader bandwidth and components traveling at different speeds. The different velocities of the components make the signal disperse as it propagates, with the consequence that the longer is the transmission distance, the larger needs to be the symbol period T_s including the guard bands (lower symbol rate). This is necessary to guarantee that at the receiver the signal corresponding to one NFDM-symbol fits completely into the processing window of duration T_s without overlapping with neighboring NFDM-symbols. To understand this we can look at the the power profile of a multi-soliton, corresponding to the nonlinear spectrum composed of the three eigenvalues $\{-0.2 + i0.45, i0.3, 0.2 + i0.45\}$, as a function of the propagation distance, shown in Figure 3.3 (b). At the transmitter the multi-soliton fits into the symbol period of duration $T_s = 1\,\text{ns}$. At the maximum transmission distance, the multi-solition breaks up into three separated fundamental solitons (Figure 3.3 (c)) and has a duration of $2\,\text{ns}$, such that only the central component falls into the receiver processing window of duration $1\,\text{ns}$. To deal with this effect the symbol rate has to be decreased to have a longer symbol period that accommodates the dispersed multi-soliton.

The imaginary part of the eigenvalues is proportional to the energy of the signal through the Parseval's identity for the NFT [28]. This tells us that adding an eigenvalue to the spectrum requires more and more energy as its imaginary part is increased.

To minimize the power consumption and the required bandwidth, the eigenvalues should be packed as close as possible over the complex plane. The minimum distance between the real and imaginary components of the eigenvalues is determined by the variance of the noise on the complex plane. This noise is in general non-Gaussian and uncorrelated in the real and imaginary axis directions, and its variance in both axes is proportional to the imaginary part of the eigenvalue [32, 40, 55, 91, 92]. For this reason to pack the eigenvalue as close as possible, subject to the noise variance, non-equally spaced
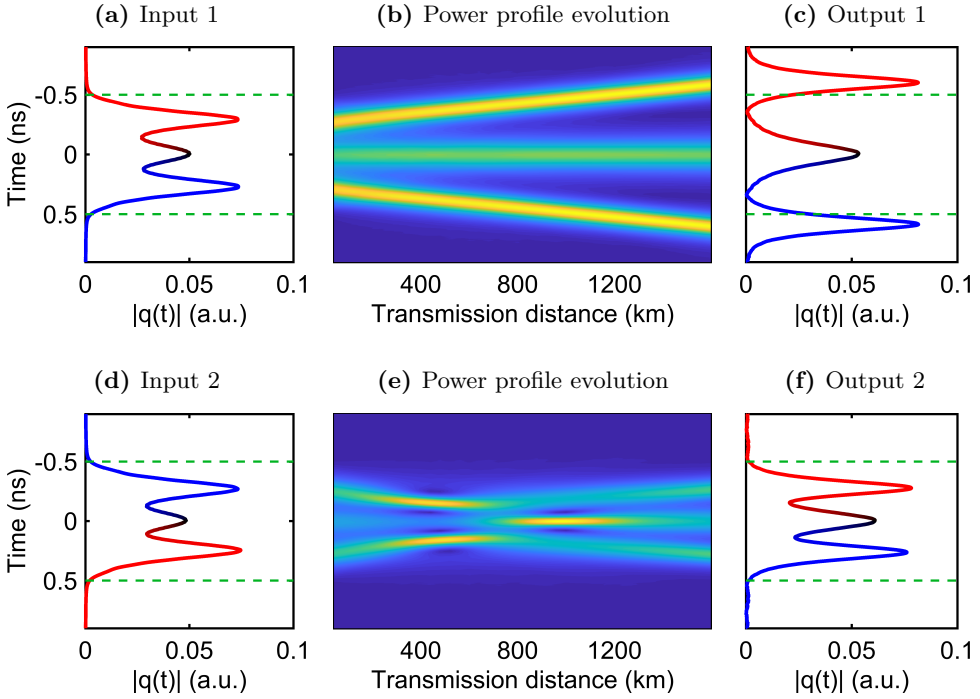
Figure 3.3: A multi-soliton whose nonlinear spectrum is composed of the eigenvalues $\{-0.2 + i0.45, i0.3, 0.2 + i0.45\}$ is considered in the two cases where the absolute value of $b(\lambda_i)$ is set to $\{20.54, 0.90, 0.03\}$ (Case 1) and $\{0.03, 0.90, 20.54\}$ (Case 2). The time profile of the multi-soliton at the input of the fiber is shown in (**a**) and (**b**), and the time profile at the output of the fiber is shown in (**c**) and (**f**) for the two cases, respectively. The processing window of the receiver, of duration $T_s = 1$ ns, is marked by green dashed lines.

placement of the eigenvalues should be used [93].

The problem of optimally placing the eigenvalues on the complex plane given some constraints is not solved yet, and further characterizations of the noise are required to help in getting closer to the solution of this problem.

Choice of the $b(\lambda_i)$ constellations   Another important design aspect of an NFDM system is the choice of the of constellations of the scattering coefficients

$b(\lambda_i)$ associated to different eigenvalues λ_i. As explained in Section 2.3.6, the absolute value of $b(\lambda_i)$ determines the position in time of the soliton component associated to the eigenvalue λ_i, and not its amplitude as one may erroneously think. For this reason the choice of PSK constellations is often made when the eigenvalues have zero real part [38].

In some cases, on the other hand, it is beneficial to choose constellations with different radii in order to separate temporally the solitonic components. One example is when jointly modulation of the continuous and discrete spectrum is performed. Indeed, in this case, the symbol period may be determined by the portion of the signal related to the continuous spectrum [43]. Another example is when multiple eigenvalues with non-zero real part are used [38].

To give a practical example of how the choice of the radii of the constellations $b(\lambda_i)$ can affect the properties of the system, we can consider again the example given in the previous section, where the multi-soliton with nonlinear spectrum composed of three eigenvalues $\{-0.2 + i0.45, i0.3, 0.2 + i0.45\}$ was propagated in the fiber. If the constellation radii are set to $\{0.03, 0.90, 20.54\}$, the multi-soliton "focuses" in the middle of the link where it is compressed in time. In this way its time duration at the maximum transmission distance is the same as the one at the transmitter. This is illustrated in Figure 3.3 (d-f). In this way the symbol period T_s does not need to be incremented to accommodate the dispersed signal, and the symbol rate of the system is not reduced. The design of the nonlinear spectrum given a constraint on the duration of the corresponding time domain signal is still an open problem. Recently, a solution was proposed for the continuous spectrum case [78], but a general solution for an arbitrary nonlinear spectrum is not yet available.

Another important aspect that determines the characteristics of the time domain signal $E_{Tx}(\tau)$, such as its peak-to-average power ratio (PAPR), is the phase rotation among the different constellations. The PAPR of $E_{Tx}(\tau)$ is defined as

$$\text{PAPR} = 10 \log \left(\frac{\max\left(|E_{Tx}(\tau)|^2\right)}{P_{Tx}} \right), \tag{3.1}$$

where $P_{Tx} = \frac{1}{T} \int_0^T |E_{Tx}(\tau)|^2 d\tau$ is the average power of the field, and T is its time duration. If we for example consider a 2-eigenvalues system with $b(\lambda_i)$ modulated with QPSK. If the relative angle θ_e between the two constellations is varied, we can see in Figure 3.4 how the resulting PAPR of the time domain signal changes significantly, achieving a desirable minimum when $\theta_e = \pi/4$. Similar results were reported and verified experimentally in [37, 94]. In the same work, it was also proposed to prune some of the symbols from the con-
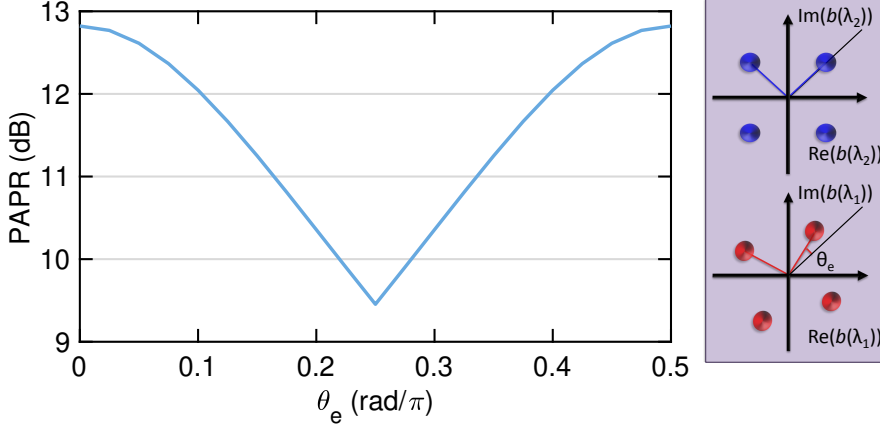
Figure 3.4: PAPR of the signal $q(t)$ as a function of the angle θ_e between the two $b(\lambda_i)$ QPSK constellations with unitary radius associated to the eigenvalues $\{\lambda_1 = i0.3, \lambda_2 = i0.6\}$ of the nonlinear spectrum.

stellation to minimize the overall PAPR of the signal, at the expense of the transmission rate. A similar approach was also proposed in [32] in order to increase the spectral efficiency of the system.

In summary, finding the optimal modulation format that maximizes the performance of a discrete NFDM system, while meeting a set of design constraints, is still an open problem. A thorough numerical investigation in this direction for a 2- and 3-soliton case was done in [95]. Further insights in the mathematical relation between the modulation format and the time domain signal properties will help solving this problem. The use of blind optimization techniques borrowed from the machine learning field could also improve the designing of such systems.

3.1.2   INFT

The NFDM-symbols output by the digital modulator are fed into the INFT block, which computes the corresponding discrete time domain signal $q(t_n)$ to be transmitted.

There are several algorithms that can be used to compute the INFT. In the specific case where the spectrum is purely discrete, the Riemann-Hilbert method, the Hirota bilinearization scheme, or the Darboux transformation (DT) can be used [79]. Alternative faster algorithms have also been introduced

[96], and recently also a fast implementation of the DT has been proposed [97]. This last one can achieve a computational complexity as low as $O(NK)$ when $N < K$, where K is the number of samples of the time domain signal and N is the number of eigenvalues.

3.1.3 Signal denormalization

The signal $q(t_n)$ produced by the INFT block is matched to the normalized channel described by (2.4). In order to create the actual signal $E_{Tx}(\tau_n)$ that will be transmitted over the real channel, the output of the INFT block needs to be denormalized according to (2.2). The shape of the signal in the normalized regime is set by the position of the eigenvalues λ_i and by their scattering coefficients $b(\lambda_i)$. Although, when the signal is denormalized, the free parameter T_0 can be tuned to "stretch" the signal and vary jointly its power and duration [39].

A peculiarity of the discrete NFDM system is that it is not possible to vary freely the power of the transmitted signal without affecting other system parameters, as it is instead possible in standard coherent systems. Indeed, the INFT block generates a signal that is properly matched to the channel, which means that the amplitude of the signal must satisfy a proper relation with the signal time duration and bandwidth.

Considering the basic soliton case, we know that the pulse peak amplitude and width must be linked for the soliton to maintain its shape during propagation. In particular, the lower the peak amplitude is, the larger must its duration be (with corresponding lower bandwidth). Similarly, multi-eigenvalues signals need to satisfy particular constrains on the power-duration relation.

If we assume that the symbol rate R_s of the system is fixed, the symbol period $T_s = 1/R_s$, i.e., the time slot where one NFDM-symbol waveform needs to fit, is fixed as well. By reducing T_0 the duration of the pulse can go from the extreme where the signal is narrow and isolated by null guard bands within the symbol period T_s (Figure 3.5 (b)), to the other extreme where its duration is so broad that part of the signal is effectively cropped because it exceeds the symbol period (Figure 3.5 (d)). In the first extreme the power of the signal is high and its bandwidth is broad, while in the second extreme the power and the bandwidth are both reduced. T_0 needs to be optimized properly in order minimize the occupied bandwidth while maintaining a power level high enough to contrast the noise, and at the same time make the guard bands large enough to avoid signal cropping and ISI among neighboring symbols at
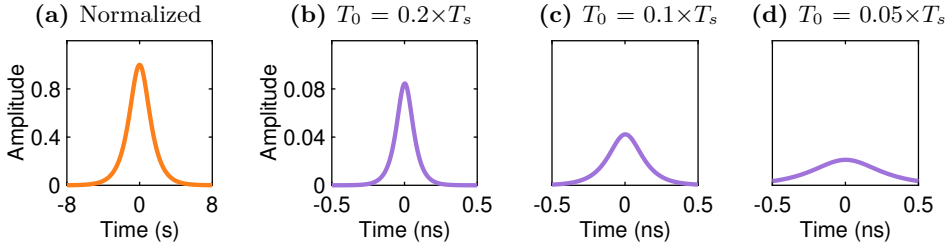
Figure 3.5: (**a**) Time profile of the signal $q(t)$ in the normalized domain. Its nonlinear spectrum is $\{\lambda_1 = i0.5,\ b(\lambda_1) = 1\}$. (**b-d**) Corresponding denormalized signal $E(\tau)$ for three different values of the free normalization parameter T_0 (given as a fraction of the symbol period T_s).

the receiver (Figure 3.5 (c)).

Depending on the design constraints of the system, we may want to fix other properties of the signal, such as its maximum power (and so its bandwidth), and optimize T_0 together with the symbol rate R_s.

In a real system the denormalization happens in two steps. The time denormalization is performed directly by the INFT block by using the symbol rate, the sampling frequency, and the T_0 parameter. Then the denormalization algorithm outputs the power P_{Tx} that the signal needs to have prior to entering the fiber channel in order to be properly matched to it (see the block diagram in Figure 3.1).

The impact of fluctuations in the transmitter launch power P_{Tx} on the performance of a discrete NFDM system has been investigated numerically [39] and experimentally [98]. The results show that even variations of a single dB in the power can lead to differences of one order of magnitude in the bit error rate (BER) of the system.

3.1.4 Transmitter transfer function pre-distortion

NFDM systems are very sensitive to the distortions of the transmitted signal given that the signal needs to be properly matched to the channel in order for the spectrum to propagate linearly in the nonlinear domain.

Distortions of the signal can be caused by linear and nonlinear effects, such as limited bandwidth and limited effective number of bits (ENOB) of the transmitter DAC, linear distortions introduced by the the electrical front-end, and
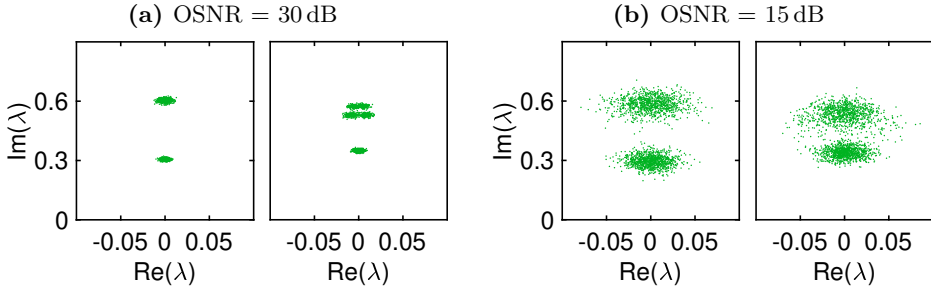
Figure 3.6: Eigenvalue constellations corresponding to two peak driving voltages of the MZM: $0.33 \times V_\pi$ and $1 \times V_\pi$, with V_π the half-wave voltage of the modulator. Two OSNR levels of the signal are considered: (**a**) OSNR = 30 dB and (**b**) OSNR = 15 dB.

nonlinear transfer function and limited extinction ratio of the Mach-Zehnder modulator (MZM). In Figure 3.6 for example, it is shown how the distortion of the transmitted signal due the nonlinear transfer function of the MZM increases the variance of the noise in the eigenvalue plane, reducing also the Gaussian characteristic of the noise. Considering the nonlinear spectrum composed of the two eigenvalues $\{\lambda_1 = i0.3, \lambda_2 = i0.6\}$, and a drive voltage of the MZM equal to its half-wave voltage V_π, we can see in Figure 3.6 (a) that the detected eigenvalues tend to split in multiple clusters and get closer to each other. When the optical signal-to-noise ratio (OSNR) is reduced, Figure 3.6 (b), the net effect is an increased noise variance and a smaller distance between the two clusters corresponding to the two reference eigenvalues.

Moreover, the waveforms corresponding to the discrete spectrum of the NFT may have a particular high PAPR, as mentioned already in a previous section, exacerbating even more some of these effects, as the DAC quantization error.

Digital pre-distortion techniques, as those reported in [99], can, for example, be used to compensate the MZM transfer function. More advanced adaptive techniques, able to compensate for linear and nonlinear distortions of the transmitter, have recently successfully used to improve the performance of a NFDM system with fully modulated spectrum [45].
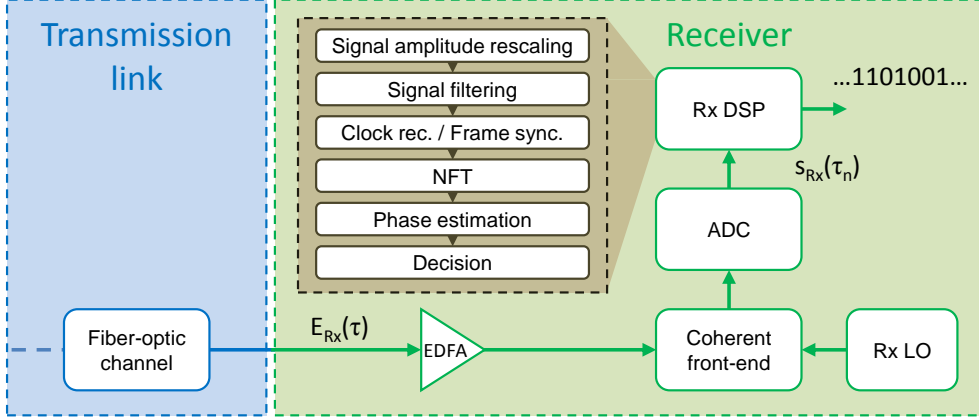
Figure 3.7: Block diagram of the NFDM receiver.

3.2 Receiver

The NFDM receiver is illustrated in Figure 3.7. The optical signal at the output of the fiber $E_{Rx}(\tau)$ is detected by the coherent front-end and digitized by the analog-to-digital converter (ADC). The digital waveform $E_{Rx}(\tau_n)$ is then processed by the receiver DSP chain in order to recover the transmitted data bits. To achieve this, the signal is first filtered and then synchronized to the processing window of the receiver. Then the signal is sliced in blocks of duration T_s, and each of these is processed by the NFT block to obtain the nonlinear spectrum. The inverse transfer function of the fiber channel $H(\lambda_i, L) = e^{4i\lambda_i^2 L/\mathcal{L}}$ is applied to the detected nonlinear spectrum to obtain the received NFDM-symbol $\mathbf{r} = \{\widehat{\lambda}_1, \ldots, \widehat{\lambda}_N, \widehat{b}(\widehat{\lambda}_1), \ldots, \widehat{b}(\widehat{\lambda}_N)\}$. The phase noise due to the linewidth of the transmitter laser and receiver local oscillator (LO), as well as the frequency offset between the two, is removed by a phase estimation block that operates in the nonlinear domain. Finally a symbol decisor takes a decision on the NFDM-symbols and recover the data bits.

In the following sections the various blocks that constitute the NFDM receiver DSP chain are described in details.

3.2.1   Signal amplitude rescaling

The receiver DSP of a standard coherent system generally operates with a normalized version of the digital signal, so that the processing is independent of the absolute amplitude of $E_{Rx}(\tau_n)$. This is not possible in an NFDM system. Indeed, the NFT uses the knowledge of the signal together with the specific channel parameters to properly compute the nonlinear spectrum. To this end it is necessary to precisely rescale the amplitude of the received digital signal $E_{Rx}(\tau_n)$.

In Section 3.1.3 we mentioned how the BER of the NFDM system is very sensitive to the launch power of the transmitted signal $E_{Tx}(\tau)$. The same is true for the power of $E_{Rx}(\tau_n)$. In this second case though, the power can be adjusted in the digital domain, making the problem less critical than the one at the transmitter.

The amplitude rescaling can be done by setting the power of $E_{Rx}(\tau_n)$ to the power P_{Tx} of the signal $E_{Tx}(\tau_n)$ generated at the transmitter by the INFT and denormalized. The first problem with this approach is that the received signal is noisy, and P_{Tx} does not account for the additional noise power (in one polarization) P_N. A better way to estimate the rescaling power, could be to use the OSNR information of the received optical signal to compute a new power $P_1 = P_{Tx} + P_N$ as follows

$$P_1 = P_{Tx}\left(1 + \frac{1}{2\,\mathrm{OSNR}} \times \frac{W}{B_{\mathrm{ref}}}\right), \tag{3.2}$$

where $B_{ref} = 12.5\,\mathrm{GHz}$ is the fixed reference noise bandwidth, and W the 99 % power bandwidth of the signal $E_{Rx}(\tau_n)$ [10].

In Figure 3.8 (a) the BER as a function of the OSNR is shown for the case where P_{Tx} and P_1 are used to rescale the received signal of a 2-eigenvalue NFDM system in a B2B configuration. The discrete nonlinear spectrum is composed of the two eigenvalues $\{\lambda_1 = i0.3, \lambda_2 = i0.6\}$, and $b(\lambda_i)$ scattering coefficients drawn from a QPSK constellation rotated by $\pi/4$ for $i = 1$, and from a conventional QPSK for $i = 2$. We can see that there is a performance gain in terms of required OSNR when P_1 is used. The OSNR gain in this case is $1\,\mathrm{dB}$ at the hard-decision forward error correction (HD-FEC) level. In Figure 3.8 (b) the BER performance is shown when a further power offset is added for the two cases where P_{Tx} and P_1 are used to rescale the signal, and for the fixed value of OSNR $= 10.5\,\mathrm{dB}$. This value of OSNR was chosen so that the performance when using P_1 are close to the HD-FEC threshold. P_{Tx} is $2\,\mathrm{dB}$ lower than the optimal value of power, and the corresponding BER is
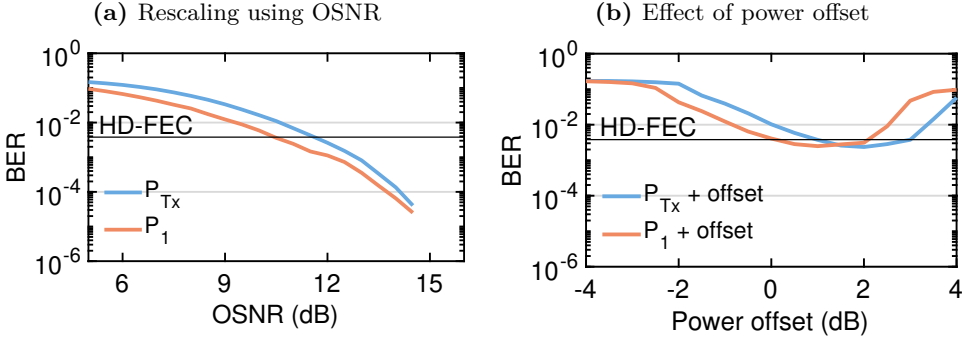
Figure 3.8: (**a**) BER as a function of the OSNR using the transmitted power P_{Tx} (light blue) and the power P_1 (orange) that uses the OSNR information according to (3.2). (**b**) BER as a function of an additional power offset to P_{Tx} and P_1.

3.9 times higher than the optimum. P_1 instead is only $1\,\mathrm{dB}$ lower, and the corresponding BER is just 1.6 times the optimal one. The fact that also P_1 does not match the optimal rescaling power could be expected given that in the presence of the noise, the nonlinear Schrödinger equation (NLSE) is not integrable, and so the theoretical prediction of the optimal rescaling power may not be exact.

In a practical system, where noise and losses are present, the best way to achieve the maximum performance of the system is to optimize the power rescaling value using, for example, training sequences.

3.2.2   Signal filtering

Filtering the signal at the receiver is required for removing the out-of-band noise. The matched filter is the optimal filter that maximizes the signal-to-noise ratio (SNR) for a linear system affected by additive white Gaussian noise (AWGN). In a fiber-optic communication system though, the channel is nonlinear, and the noise is in general not Gaussian. In this scenario the matched filter is not optimal anymore as shown in [100]. In the same work it was shown that filtering using a rectangular low pass filter is a better choice, when the optimal filter is unknown. The bandwidth of the filter must be large enough to contain the entire signal bandwidth but narrow enough to suppress the out-of-band noise.

(a) Bandwidth evolution
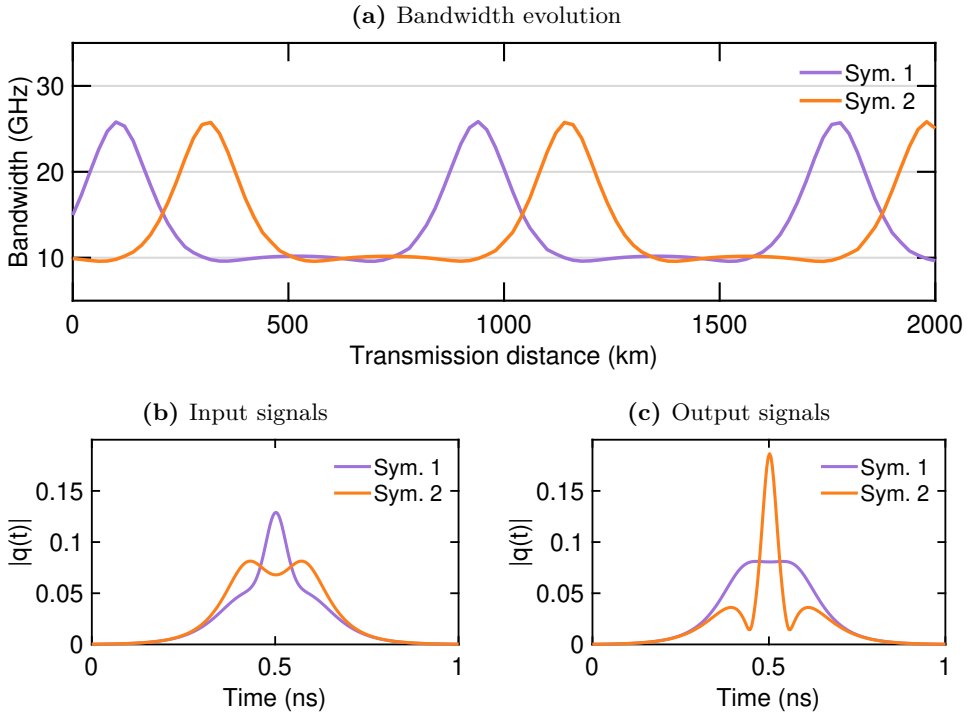
Figure 3.9: **(a)** Evolution of the bandwidth along the fiber for the Λ-shaped (violet) and M-shaped (orange) signals. Pulses at the input **(b)** and output **(c)** of the fiber channel.

In the case of a discrete NFDM system, where the optimal filter is unknown, using a rectangular filter seems a logical choice to start with. The only problem left is finding the optimal filter bandwidth. A peculiarity of a discrete NFDM system is that the waveforms associated to different NFDM symbols have different bandwidths. Moreover, the bandwidth of the NFDM signals varies during propagation in the fiber channel [39].

To show this we can consider an NFDM system with two eigenvalues $\{\lambda_1 = i0.3, \lambda_2 = i0.6\}$. If we set the value of the scattering coefficients $b(\lambda_i)$ associated to the two eigenvalues to $\{1, \exp(i1/4\pi)\}$ and $\{1, \exp(i3/4\pi)\}$ we obtain in the first case a Λ-shaped pulse, whose 99% power bandwidth at the input of the fiber channel is 1.5 times that of the M-shaped pulse obtained in the second case. The two pulses are shown in Figure 3.9 (b). The evolution

of the bandwidth of the two pulses as they are transmitted through $2000\,\mathrm{km}$ of lossless single-mode fiber (SMF) is shown in Figure 3.9 (a), and the two pulses at the output of the fiber are shown in Figure 3.9 (c). We can see that the bandwidth of the pulses at the output of the fiber channel can be higher than the one at the input. This should be taken into account in order to set the filter bandwidth to the maximum value of bandwidth that can occur for any of the pulses in the system.

Let us now consider a multi-user scenario where different parts of the nonlinear spectrum, such as set of eigenvalues with different real part, are assigned to different users [101]. In this scenario a filter is required to extract the portion of the nonlinear spectrum of a specific user. In this case using a rectangular filter to extract a single channel is not a good solution because part of the information may have leaked outside the filter bandwidth by phenomena such as four-wave mixing (FWM). In order to preserve the orthogonality of the different channels in the NFT sense, the only currently available possibility to demultiplex the channels is to digitally demultiplex in the nonlinear domain. This requires to perform a joint NFT of the signal corresponding to the whole linear spectrum and then extract the channel of interest. Clearly this approach is impractical given that it requires to process large chunks of spectrum at once, similarly to the multi-channel digital back-propagation (DBP) technique. The problem of how to extract a single NFDM channel in the optical domain is still open and probably the most important problem to solve to determine the success of NFDM systems in the future.

3.2.3   Clock recovery and frame synchronization

The NFDM system transmits the data in blocks so that proper frame synchronization is required in order to align the waveform corresponding to a single NFDM symbol to the processing window of the receiver. A synchronization scheme for NFDM could be realized by inserting pilot symbols at regular intervals among the data frames, as it is commonly done in OFDM [102]. In this section we are not going to discuss a particular implementation of the frame synchronization algorithm, but rather discuss some peculiar effects that can be observed on the nonlinear spectrum in the presence of sub-optimal synchronization.

One effect that can be seen when the signal is not properly synchronized, because it is retarder (advanced), is the shrinking (expansion) of the received $b(\lambda_i)$ constellations. Indeed, considering the case of the fundamental soliton,
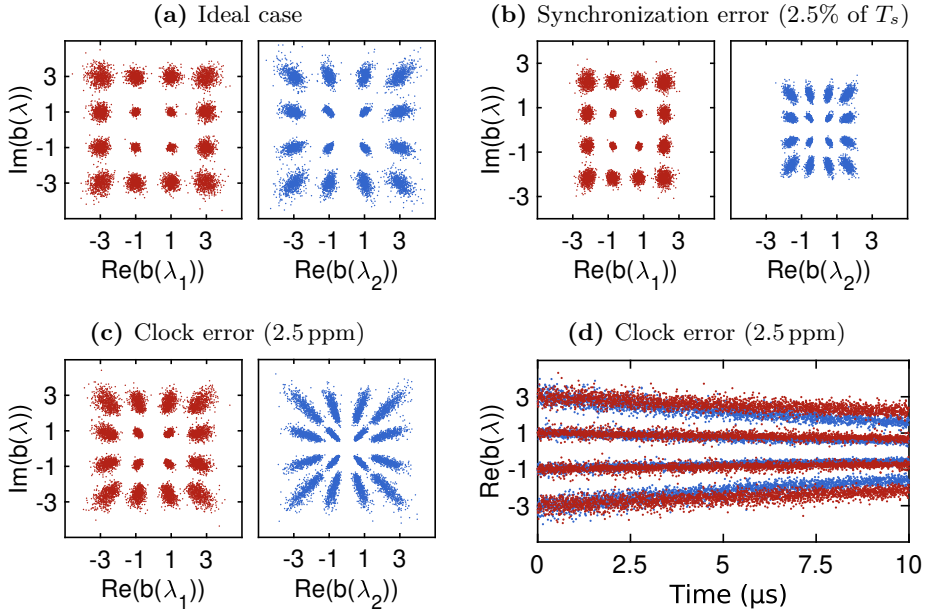
Figure 3.10: Effects of synchronization and clock errors in a 2-eigenvalues NFDM system with $b(\lambda_i)$ constellations modulated with 16-QAM. The constellations associated to the two eigenvalues $\{\lambda_1 = i0.3, \lambda_2 = i0.6\}$ are shown in three cases: (**a**) perfect frame synchronization and clock; (**b**) fixed frame synchronization error of 2.5% of the symbol period T_s; (**c**) ADC clock error of 2.5 ppm. (**d**) Time evolution of the real part of the constellations for the third case.

we know from the relation between the time domain signal and the nonlinear spectrum in (2.36) that the absolute value of the scattering coefficient $b(\lambda_i) = Q_d(\lambda_i)a'(\lambda_i)$ is a nonlinear function of the delay t_1 of the signal. This effect can also be seen when a multi-eigenvalue signal is considered. The two $b(\lambda_i)$ constellations in Figure 3.10 (a), corresponding to the two discrete eigenvalues $\{\lambda_1 = i0.3, \lambda_2 = i0.6\}$, shrink when the the signal has a synchronization error of 2.5% of the symbol period T_s, as shown in Figure 3.10 (b). This nonlinear scaling effect may not be particularly relevant when dealing with PSK constellations, but can be problematic for QAM.

The relation of the constellation radii with the timing delay of the signal can also be used to reveal clock errors. If the clock of the transmitter DAC

and the receiver ADC are not exactly the same, the NFDM pulse slowly drifts within the processing window causing a slow scaling of the constellations over time. In Figure 3.10 (c) the constellations distorted by a clock error of 25 parts-per-million (ppm) are shown, and the evolution over time of the real part of the constellations is shown in Figure 3.10 (d).

3.2.4   Computing the NFT

Once the signal $E_{Rx}(\tau, \ell)$ has been rescaled, filtered, and synchronized, it can finally be fed into the NFT block, which normalizes it using (2.2), that is

$$q = \frac{E}{\sqrt{P}}, \qquad t = \frac{\tau}{T_0}, \qquad z = -\frac{\ell}{\mathcal{L}}, \tag{3.3}$$

and computes the received NFDM-symbol $\mathbf{r} = \{\widehat{\lambda}_1, \dots, \widehat{\lambda}_N, \widehat{b}(\widehat{\lambda}_1), \dots, \widehat{b}(\widehat{\lambda}_N)\}$ of each section of duration T_s of the signal.

To operate, the NFT block needs to be able to compute the scattering coefficients $a(\lambda)$ and $b(\lambda)$ at an arbitrary point λ in the upper half complex plane $\mathbb{C}^+$. This can be done by using the equations (2.21a), here reported for convenience

$$a(\lambda) = \lim_{t \to +\infty} \phi_1^N(t, \lambda) e^{i\lambda t} \tag{3.4a}$$

$$b(\lambda) = \lim_{t \to +\infty} \phi_2^N(t, \lambda) e^{-i\lambda t}. \tag{3.4b}$$

The only unknown term in these equations is $\phi^N(+\infty, \lambda)$, which can be calculated by propagating the Jost solution $\phi^N(t, \lambda)$ from $t = -\infty$ to $t = +\infty$, as explained in Section 2.3.4. To perform this propagation the system of linear ordinary differential equations

$$\frac{\partial v}{\partial t} = \begin{pmatrix} -i\lambda & q \\ -q^* & i\lambda \end{pmatrix} v \tag{3.5}$$

needs to be integrated.

This integration can be performed using one of the many standard integration methods available in the literature, from the simple first-order Euler method, to more sophisticated methods, such as the fourth-order Runge-Kutta method, or the Ablowitz-Ladik discretization. A thorough overview of the numerical methods for computing the direct NFT can be found in [79]. A method

of particular interest for computing the scattering coefficients when the eigenvalues are complex is the trapezoidal discretization method. This was shown to be one of the algorithms that provides the best results in terms of numerical precision when the eigenvalues are complex [81]. This algorithm will be presented in detail in Section 4.3 in the context of the dual-polarization NFT.

By recalling the parallel between NFDM and OFDM, we know that the discrete eigenvalues of NFDM play the role of the linear frequencies of OFDM. In the OFDM case the receiver knows where the frequencies of the subcarriers are located, while the NFDM receiver needs to determine the position of the eigenvalues from the received time domain signal. Indeed, the presence of the channel impairments, such as fiber loss and noise, modifies the position of the eigenvalues along the propagation [91].

For this reason the NFT block determines the discrete spectrum of the signal in two steps: first it locates the discrete eigenvalues $\{\widehat{\lambda}_1, \ldots, \widehat{\lambda}_N\}$, and then it computes the corresponding scattering coefficients $\{\widehat{b}(\widehat{\lambda}_1), \ldots, \widehat{b}(\widehat{\lambda}_N)\}$.

By recalling that the discrete eigenvalues are located at the zeros of the function $a(\lambda)$ over the upper half complex plane, we can employ standard root searching methods, such as the Newton-Raphson method to find them [79]. This method starts from an initial guess of the root $\lambda^{(0)}$, computes $a(\lambda_0)$ by solving (3.5) for $\lambda^{(0)}$, and checks if the value of $a(\lambda^{(0)})$ found is zero; if this is the case, it means that $\lambda^{(0)}$ is an eigenvalue and the algorithm stops, otherwise the guess is updated according to the rule

$$\lambda^{(k+1)} = \lambda^{(k)} - \epsilon \frac{a(\lambda^{(k)})}{a'(\lambda^{(k)})}, \tag{3.6}$$

where ϵ is the step modifier, and the procedure is repeated. This method is well suited for the discrete NFDM system for two reasons: the number of transmitted eigenvalues is fixed for each symbol, and the reference location of the eigenvalues is known to the receiver, so that they can be used to initialize the algorithm. Other methods, such as the Fourier collocation method [79] can also be used to locate the eigenvalues. Both these methods may not be totally accurate in locating the eigenvalues when the processed signal is distorted by the channel impairments. It can happen that not all the eigenvalues are located, or that new spurious eigenvalues are found.

Once all the N eigenvalues have been located, where possible, the corresponding scattering coefficients $b(\widehat{\lambda}_i)$ can be computed using (3.4b).

The last operation performed by the NFT block is to apply the inverse transfer function of the channel $H(\lambda_i, L) = e^{4i\lambda_i^2 L/\mathcal{L}}$ to $b(\widehat{\lambda}_i)$ to compensate

for the propagation in the nonlinear channel as follows

$$\widehat{b}(\widehat{\lambda}_i) = e^{4i\lambda_i^2 L/\mathcal{L}} b(\widehat{\lambda}_i).$$ (3.7)

Finally, the received NFDM-symbol $\mathbf{r} = \{\widehat{\lambda}_1, \ldots, \widehat{\lambda}_N, \widehat{b}(\widehat{\lambda}_1), \ldots, \widehat{b}(\widehat{\lambda}_N)\}$ is passed forward to the next block of the DSP chain, which performs further processing in the nonlinear domain, before the symbol decisor retrieves the data bits.

3.2.5   Phase estimation

In standard coherent systems, carrier phase estimation is necessary to compensate for the rotation of the received constellation. This rotation is caused by the random frequency and phase oscillations of the carrier of the transmitted optical signal and of the LO of the coherent receiver. In an NFDM system the same rotation effect of the received $b(\lambda_i)$ constellations can be observed and needs to be compensated for.

If we consider again the signal-nonlinear spectrum relation for the fundamental soliton case given in (2.35), we can see that the phase of the time domain signal is proportional to the phase of $Q_d(\lambda_i)$ (and so to the one of $b(\lambda_i)$). This means that the phase noise affecting the signal translates to a phase noise on the $b(\lambda_i)$ symbols. In the NFDM case though, the time domain phase noise has also an impact on the amplitude of the $b(\lambda_i)$ symbols [39], and the phase noise on $b(\lambda_i)$ depends also on the noise on the eigenvalues λ_i [94].

To estimate the phase of the received $b(\lambda_i)$ symbols, standard algorithms such as Viterbi-Viterbi [103], or blind phase search (BPS) [104] have been proven to work when applied directly over the nonlinear domain constellation for the single eigenvalue case [39]. In our work [C2] we also used blind phase search successfully when multiple eigenvalues are present in the nonlinear spectrum. Nonetheless, these algorithms should be optimized for the NFDM case in the future. To further reduce the phase noise, novel equalization techniques in the nonlinear domain have also been proposed [57, 105].

3.2.6   Symbol decisor

The symbol decisor estimates what symbol $\mathbf{s}_m = \{\lambda_1, \ldots, \lambda_N, b(\lambda_1), \ldots, b(\lambda_N)\}$ was transmitted among the possible NFDM-symbols $\{\mathbf{s}_m, 1 < m < M^N\}$, where M is the constellation order and N the number of eigenvalues, based on the received NFDM-symbol $\mathbf{r} = \{\widehat{\lambda}_1, \ldots, \widehat{\lambda}_N, \widehat{b}(\widehat{\lambda}_1), \ldots, \widehat{b}(\widehat{\lambda}_N)\}$.
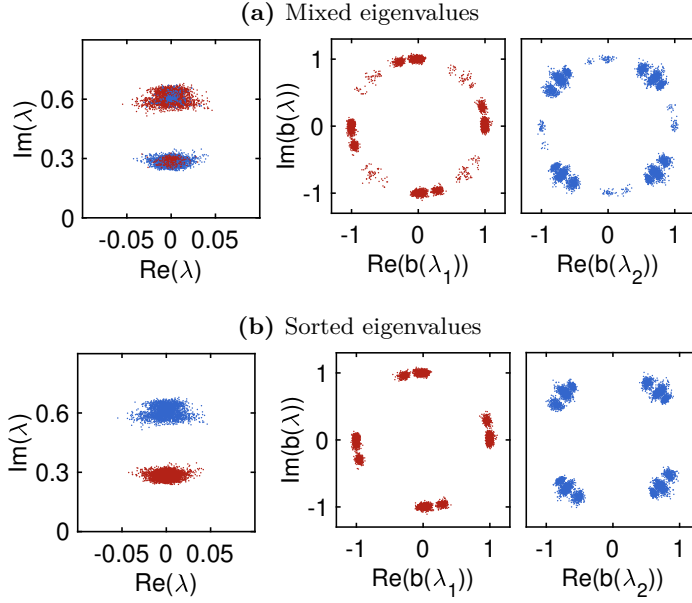
Figure 3.11: (**a**) Eigenvalue constellation: first (red) and second (blue) detected eigenvalue for each NFDM-symbol, and respective $b(\lambda_i), i = 1, 2$ scattering coefficients. (**b**) The same constellations after a decision has been taken on the eigenvalues, and both the eigenvalues and the scattering coefficients has been sorted.

The transmitted and received symbols are related by the transitional probability function of the channel $p(\mathbf{r}|\mathbf{s}_m)$ [67]. When the transmitted symbols are equiprobable, the optimal decision strategy is the maximum likelihood (ML) rule, defined as

$$\widehat{m} = \operatorname*{argmax}_{1 < m < M^N} p(\mathbf{r}|\mathbf{s}_m). \tag{3.8}$$

However, this detection scheme may be extremely complex to implement practically due to the lack of an analytical model to estimate the channel transition probability distribution $p(\mathbf{r}|\mathbf{s}_m)$. In the works presented in this thesis, a simpler detection scheme has been used. This scheme performs the decision independently on each $\widehat{b}(\widehat{\lambda}_i), i = 1, \ldots, N$ based on the minimum Euclidean distance criterion

$$\widehat{m}' = \operatorname*{argmin}_{1 < m' < M} d(\widehat{b}(\widehat{\lambda}_i), b_{m'}(\lambda_i)), \tag{3.9}$$

where $d(\cdot, \cdot)$ is the Euclidean distance in $\mathbb{C}$, and $C_{r,i} = \{b_{m'}(\lambda_i)\}, 1 < m' < M\}$ is the reference constellation for the i-th scattering coefficient. This rule is similar to the decision process used in OFDM systems. However, in the NFDM case some new problems that can arise need to be taken into account.

The first problem is that, as a consequence of the joint presence of the noise and of the fiber loss, some of the discrete eigenvalues can vanish, and some spurious one may appear. A second problem is that the NFDM receiver does not locate the eigenvalues following a specific order. This makes it difficult to associate each detected scattering coefficient $\widehat{b}(\widehat{\lambda}_i)$ to its reference constellation $C_{r,i}$, in order to take the decision. For example, this can happen when the Newton-Raphson method is used with an initial guess picked at random over a complex plane region surrounding the reference eigenvalues. To give an example of this problem, let us consider a 2-eigenvalue NFDM system with the two eigenvalues $\{\lambda_1 = i0.3, \lambda_2 = i0.6\}$, and $b(\lambda_i)$ scattering coefficients drawn from a QPSK constellation rotated by $\pi/4$ for $i = 1$, and from a conventional QPSK for $i = 2$. An example of received NFDM-symbols (eigenvalues and scattering coefficients) is shown in Figure 3.11 (a). The leftmost inset shows the detected eigenvalues: the first located one is depicted in red, while the second one in blue. The $\widehat{b}(\widehat{\lambda}_i)$ constellations associated with the first and second located eigenvalue are shown in the following two insets. We can clearly see that there is a mixing of the two $\widehat{b}(\widehat{\lambda}_i)$ constellations. Given that the reference constellations for $\widehat{b}(\widehat{\lambda}_1)$ and $\widehat{b}(\widehat{\lambda}_2)$ are different, it is necessary to properly sort the $\widehat{b}(\widehat{\lambda}_i)$ to assign them to the correct reference constellation before taking the decision.

The pseudo-code of the proposed symbol decisor is given in Algorithm 2. The algorithm tries to assign to each reference eigenvalue λ_i the closest detected one $\widehat{\lambda}_j$. Note that two detected eigenvalues may be both closer to the same reference one, but using the proposed algorithm they can be associated with two different reference eigenvalues. This is done because the NFDM receiver always expects to receive N eigenvalues, no more no less, so that the algorithm tries to minimize the reference eigenvalues without a match.

Once the decision has been taken over the eigenvalue space, $\widehat{b}(\widehat{\lambda}_i)$ can be associated with their reference constellations based on this decision. If the number of detected eigenvalues is less than N, the $\widehat{b}(\widehat{\lambda}_i)$ associated to the i-th missing eigenvalue is generated by drawing a random value from the reference constellations $C_{r,i}$. This allows taking the correct decision on average $1/M$ times when an eigenvalue is missing. At this point the decision can be taken according to the rule in (3.8). In Figure 3.11 (b) we can see the received eigenvalues and $\widehat{b}(\widehat{\lambda}_i)$ constellations after being sorted by the decisor block.

Algorithm 2 NFDM decisor

1: **procedure** DECISION
2:     $\Lambda \leftarrow [\lambda_1, \dots, \lambda_N]$ $\triangleright$ Array of N reference eigenvalues
3:     $\widehat{\Lambda} \leftarrow [\widehat{\lambda}_1, \dots, \widehat{\lambda}_S]$ $\triangleright$ Array of S found eigenvalues
4:     $B \leftarrow [\widehat{b}(\widehat{\lambda}_1), \dots, \widehat{b}(\widehat{\lambda}_S)]$ $\triangleright$ Array of $b(\lambda_i)$ scattering coefficients
5:     $C \leftarrow [C_{r,1}, \dots, C_{r,N}]$ $\triangleright$ Array of the reference $b(\lambda_i)$ constellations
6:
7:     $\widehat{\Lambda}' \leftarrow \widehat{\Lambda}$
8:     $\Lambda' \leftarrow \Lambda$
9:     $\widehat{\Lambda}_d \leftarrow [\,]$
10:    **while** Λ' is not empty **and** $\widehat{\Lambda}'$ is not empty **do**
11:        $\forall \, \widehat{\lambda}_j \in \widehat{\Lambda}'$ find closest $\lambda_i \in \Lambda'$
12:                          $\triangleright$ More than one $\widehat{\lambda}_j$ can be associated to one λ_i
13:        $\widehat{\Lambda}_d \leftarrow \widehat{\Lambda}_d \cup [\widehat{\lambda}_j$ that are the closest to the matched $\lambda_i \in \Lambda']$
14:        $\Lambda' \leftarrow \Lambda' \backslash [\lambda_i$ with at least one matching $\widehat{\lambda}_j \in \widehat{\Lambda}_d]$
15:        $\widehat{\Lambda}' \leftarrow \widehat{\Lambda}' \backslash \widehat{\Lambda}_d$
16:    **end while**
17:        $\triangleright$ At this point, each λ_i has either no match or a single matching $\widehat{\lambda}_j$
18:    $\forall \, \widehat{\lambda}_j \in \widehat{\Lambda}_d$ if $\widehat{\lambda}_j$ is the closest to λ_i, assign $\widehat{b}(\widehat{\lambda}_j)$ to the reference constellation $C_{r,i}$
19:    $\forall \, i$ such that $\lambda_i \in \Lambda \backslash \Lambda'$ assign to $\widehat{b}(\widehat{\lambda}_i)$ a random point from $C_{r,i}$
20:                          $\triangleright$ Fill the gaps, due to eigenvalues not found
21: **end procedure**

This decision method is only an example that can be used to deal with some of the particular problems of the NFDM system, but more advanced decision techniques should be investigated to optimize the BER performance of this type of systems.

3.3   Summary

In this chapter the structure of a discrete NFDM system has been described. In the first part the different components of the transmitter have been presented, and the design of the nonlinear spectrum constellation has been discussed It was mentioned how the placement of the eigenvalues and the choice of the $b(\lambda_i)$ constellations are critical aspects of the system. In the second part of the

chapter the components of the receiver have been described, elaborating on the peculiar effects on the received constellations arising from the synchronization problems, and the particular design of the symbol decisor for a discrete NFDM system. The operations of normalization and denormalization have also been discussed, and the effects on the BER performance of the system when the signal power is not correctly rescaled at the receiver have been analyzed with numerical simulations. This chapter only touched the issues of this type of systems, in the hope to give the reader a grasp of how NFDM system are different from standard linear coherent systems.

Dual-polarization nonlinear frequency division multiplexing

4.1 Introduction

A series of key challenges that need to be met in order to bring nonlinear Fourier transform (NFT)-based communication to exit the labs and operate in real-world infrastructures, has been described recently [29]. One of those challenges consists of endowing the eigenvalue communication approach with polarization division multiplexing, which allows information to be encoded on both orthogonal polarization components supported by single-mode fibers (SMFs). The description of the light propagation, accounting for its polarization dynamics, can, under specific conditions that apply to modern communications fiber link, be described by the Manakov equations [106]. In a milestone paper of nonlinear science, Manakov showed that those equations can be solved analytically by the inverse scattering transform (IST) [107]. Detailed investigations of the solutions of the Manakov equations, especially concerning soliton and multisoliton dynamics in the presence of noise and polarization mode dispersion (PMD) in optical communications, are present in the literature [108–113].

The NFT dual-polarization problem has never been tackled at the level to demonstrate a working communication system, and only few numerical works are present in the literature on this topic [65, 66].

In this chapter, which is based on [J1, C4], the mathematical framework underlying the dual-polarization NFT is presented together with a description of a dual-polarization nonlinear frequency division multiplexing (DP-NFDM) fiber-optic communication system. Then the results of the first experimental

demonstration of such a system are presented, showing a transmission up to 373.5 km at the hard-decision forward error correction (HD-FEC) bit error rate (BER) threshold of 3.8×10^{-3}. The information was encoded in the quadrature phase-shift keying (QPSK) modulated scattering coefficients associated with two eigenvalues belonging to the Manakov system (MS) discrete spectrum, for both orthogonal polarization components supported by a SMF.

The rest of this Chapter is structured as follows: Section 4.2 defines the NFT for the dual-polarization case, and it describes the mathematical tools needed to generate the waveforms associated with a desired nonlinear spectrum for both field polarizations. Section 4.3 presents a numerical method for computing the dual-polarization direct NFT. Section 4.4 discusses the details of a practical example of a DP-NFDM system. Finally, Section 4.5 presents a detailed account of the experimental transmission results, followed by a discussion of the results, and conclusions in Section 4.6.

4.2   Mathematical framework

This section first introduces the Manakov channel model and then extends the NFT theory presented in Section 2.3 to the dual-polarization case.

4.2.1   Channel model

The evolution of the slowly varying complex-valued envelopes of the electric field propagating in a SMF exhibiting random birefringence, and whose dispersion and nonlinear lengths are much larger than the birefringence correlation length, is described by the averaged Manakov equations [106, 114]

$$
\begin{cases}
\dfrac{\partial E_1(\tau, \ell)}{\partial \ell} = -i\dfrac{\beta_2}{2}\dfrac{\partial^2 E_1(\tau, \ell)}{\partial \tau^2} + i\dfrac{8\gamma}{9}\left(|E_1(\tau, \ell)|^2 + |E_2(\tau, \ell)|^2\right)E_1(\tau, \ell) \\[4mm]
\dfrac{\partial E_2(\tau, \ell)}{\partial \ell} = -i\dfrac{\beta_2}{2}\dfrac{\partial^2 E_2(\tau, \ell)}{\partial \tau^2} + i\dfrac{8\gamma}{9}\left(|E_1(\tau, \ell)|^2 + |E_2(\tau, \ell)|^2\right)E_2(\tau, \ell)
\end{cases}
$$

$$(4.1)$$

where τ and ℓ represent the time and space coordinates, $E_j(\tau, \ell)$, $j = 1, 2$ are the amplitudes of the two electric field polarizations, β_2 is the group velocity dispersion (GVD), and γ is the nonlinear parameter.

The normalized MS [68, 69, 107] for the anomalous dispersion regime

$(\beta_2 < 0)$ is

$$\begin{cases} i\dfrac{\partial q_1(t,z)}{\partial z} = \dfrac{\partial^2 q_1(t,z)}{\partial t^2} + 2\left(|q_1(t,z)|^2 + |q_1(t,z)|^2\right) q_1(t,z) \\ i\dfrac{\partial q_2(t,z)}{\partial z} = \dfrac{\partial^2 q_2(t,z)}{\partial t^2} + 2\left(|q_1(t,z)|^2 + |q_2(t,z)|^2\right) q_2(t,z) \end{cases} \qquad (4.2)$$

with z and t the normalized space and time variables, respectively, and is derived from (4.1) through the change of variables

$$q_j = \frac{E_j}{\sqrt{P}}, \qquad t = \frac{\tau}{T_0}, \qquad z = -\frac{\ell}{\mathcal{L}}, \qquad (4.3)$$

with $P = |\beta_2|/(\frac{8}{9}\gamma T_0^2)$, $\mathcal{L} = 2T_0^2/|\beta_2|$ and T_0 is the free normalization parameter.

As for the case of the nonlinear Schrödinger equation (NLSE), the presence of the fiber loss makes the MS not integrable. The lossless path-averaged (LPA) approximation presented in Section 2.4 can be applied to the MS to obtain an equivalent lossless propagation equation over which it is possible to define the dual-polarization NFT. The same conditions and limitations of the model in Section 2.4 apply for this case.

4.2.2 Inverse scattering auxiliary problem

In order to compute the NFT of a signal $q_{1,2}(t)$, it is first necessary to associate an auxiliary problem to the MS (4.2) that for the Manakov case we can call the Manakov-Zakharov-Shabat spectral problem (MZSP). The MZSP is defined by the following system of linear ordinary differential equations

$$\frac{\partial v}{\partial t} = (\lambda \mathbf{A} + \mathbf{B}) v \qquad (4.4a)$$

$$\frac{\partial v}{\partial z} = \left(-2\lambda^2 \mathbf{A} - 2\lambda \mathbf{B} + \mathbf{C}\right) v \qquad (4.4b)$$

being

$$\mathbf{A} = \begin{pmatrix} -i & 0 & 0 \\ 0 & i & 0 \\ 0 & 0 & i \end{pmatrix} \quad \mathbf{B} = \begin{pmatrix} 0 & q_1 & q_2 \\ -q_1^* & 0 & 0 \\ -q_2^* & 0 & 0 \end{pmatrix}$$

$$\mathbf{C} = \begin{pmatrix} i(|q_1|^2 + |q_2|^2) & i\frac{\partial q_1}{\partial z} & i\frac{\partial q_2}{\partial z} \\ i\frac{\partial q_1^*}{\partial z} & -q_1^* q_1 & -iq_1^* q_2 \\ i\frac{\partial q_2^*}{\partial z} & -iq_2^* q_1 & -iq_2^* q_2 \end{pmatrix}$$

and v is a solution and λ is an eigenvalue.

4.2.3   Direct NFT

Assuming the vanishing boundary conditions for the signal, $|q_{1,2}(t)| \to 0$ for $t \to |\infty|$, a possible set of canonical Jost solutions to (4.4a) are [68]:

$$\phi^N(t,\lambda) \to \begin{pmatrix} 1 \\ 0 \\ 0 \end{pmatrix} e^{-i\lambda t}; \quad \bar{\phi}^N(t,\lambda) \to \begin{pmatrix} 0 & 0 \\ 1 & 0 \\ 0 & 1 \end{pmatrix} e^{i\lambda t} \quad t \to -\infty \qquad (4.5a)$$

$$\phi^P(t,\lambda) \to \begin{pmatrix} 0 & 0 \\ 1 & 0 \\ 0 & 1 \end{pmatrix} e^{i\lambda t}; \quad \bar{\phi}^P(t,\lambda) \to \begin{pmatrix} 1 \\ 0 \\ 0 \end{pmatrix} e^{-i\lambda t} \quad t \to +\infty \; . \qquad (4.5b)$$

$\{\phi^P(t,\lambda),\, \bar{\phi}^P(t,\lambda)\}$ and $\{\phi^N(t,\lambda),\, \bar{\phi}^N(t,\lambda)\}$ are two bases for the eigenspace associate to λ. $\phi^N(t,\lambda)$ and $\bar{\phi}^N(t,\lambda)$ can be expressed as a linear combination of the basis vectors $\{\phi^P(t,\lambda),\, \bar{\phi}^P(t,\lambda)\}$ as

$$\phi^N(t,\lambda) = \phi^P(t,\lambda)b(\lambda) + \bar{\phi}^P(t,\lambda)a(\lambda) \qquad (4.6a)$$

$$\bar{\phi}^N(t,\lambda) = \phi^P(t,\lambda)\bar{a}(\lambda) + \bar{\phi}^P(t,\lambda)\bar{b}(\lambda) \qquad (4.6b)$$

with scattering coefficients $a(\lambda)$, $b(\lambda)$, $\bar{a}(\lambda)$ and $\bar{b}(\lambda)$, where $a(\lambda)$ is a scalar, $\bar{a}(\lambda)$ is a 2×2 matrix, $b(\lambda)$ is a two entries column vector and $\bar{b}(\lambda)$ is a two entries row vector.

   Analogously to the case of the NLSE, we can define the NFT continuous and discrete spectral amplitudes for the MS as:

$$Q_c(\lambda) = b(\lambda)a(\lambda)^{-1} \qquad\qquad \lambda \in \mathbb{R} \qquad (4.7a)$$

$$Q_d(\lambda_i) = b(\lambda_i)a'(\lambda_i)^{-1} \qquad\qquad \lambda_i \in \mathbb{C}^+, i = 1,\dots,N \qquad (4.7b)$$

and $a'(\lambda_i) = \frac{\mathrm{d}a(\lambda)}{\mathrm{d}\lambda}|_{\lambda=\lambda_i} \; \forall \; \lambda_i \in \mathbb{C}^+, i = 1,\dots,N$, where N is the number of discrete eigenvalues, such that $a(\lambda_i) = 0$.

   The scattering coefficients are time independent and their spatial evolution is given by [68]:

$$a(\lambda,z) = a(\lambda,0) \qquad\qquad \bar{a}(\lambda,z) = \bar{a}(\lambda,0) \qquad (4.8a)$$

$$b(\lambda,z) = b(\lambda,0)e^{-4i\lambda^2 z} \qquad\qquad \bar{b}(\lambda,z) = \bar{b}(\lambda,0)e^{4i\lambda^2 z}. \qquad (4.8b)$$

In order to not overburden the notation, the explicit space dependence is dropped, as it was done in the beginning of this section.

The scattering coefficients can be computed using the Jost solutions and the projection equation (4.6a) following the same procedure explained in Section 2.3.4 for the NLSE case. The scattering coefficients as a function of the components of the Jost solutions are

$$a(\lambda) = \lim_{t \to +\infty} \left[\phi_1^N(t, \lambda) \bar{\phi}_1^P(t, \lambda)^{-1} \right] \tag{4.9a}$$

$$b_1(\lambda) = \lim_{t \to +\infty} \left[\phi_2^N(t, \lambda) \phi_{2,1}^P(t, \lambda)^{-1} \right] \tag{4.9b}$$

$$b_2(\lambda) = \lim_{t \to +\infty} \left[\phi_3^N(t, \lambda) \phi_{3,2}^P(t, \lambda)^{-1} \right] \tag{4.9c}$$

and using (4.5) and (4.6a) finally result in

$$a(\lambda) = \lim_{t \to +\infty} \left[\phi_1^N(t, \lambda) e^{i\lambda t} \right] \tag{4.10a}$$

$$b(\lambda) = \begin{pmatrix} b_1(\lambda) \\ b_2(\lambda) \end{pmatrix} = \lim_{t \to +\infty} \left[\begin{pmatrix} \phi_2^N(t, \lambda) \\ \phi_3^N(t, \lambda) \end{pmatrix} e^{-i\lambda t} \right] . \tag{4.10b}$$

It should be noted that, compared to the NLSE case, there is an additional scattering coefficient $b_2(\lambda)$ that can be used to encode information, potentially doubling the system transmission rate.

4.2.4 Inverse NFT

This section describes the inverse nonlinear Fourier transform (INFT) computed using the Darboux transformation (DT) for the MS derived by Wright [115], which extends the procedure presented in Section 2.3.5 for the NLSE case.

Let v be a column vector solution of the MZSP spectral problem (4.4a) associated with the MS for the signal $q_{1,2}(t)$ and the eigenvalue λ, then according to [115] a new solution of (4.4a), $\widetilde{v}$, is given by the following equation:

$$\widetilde{v} = (\lambda \mathbf{I}_3 - \mathbf{G}_0) v, \tag{4.11}$$

where $\mathbf{I}_3$ is the 3×3 identity matrix, $\mathbf{G}_0 = \mathbf{\Theta} \mathbf{M}_0 \mathbf{\Theta}^{-1}$ with

$$\mathbf{\Theta} = \begin{pmatrix} \bar{v}_1 & \bar{v}_2^* & \bar{v}_3^* \\ \bar{v}_2 & -\bar{v}_1^* & 0 \\ \bar{v}_3 & 0 & -\bar{v}_1^* \end{pmatrix}, \tag{4.12}$$

where the matrix $\mathbf{M}_0 = \text{diag}(\lambda_0, \lambda_0^*, \lambda_0^*)$, and $\bar{v} = (\bar{v}_1, \bar{v}_2, \bar{v}_3)^T$ is a solution of (4.4a) for the seed signal $q_{1,2}(t)$ and the spectral parameter λ_0. The DT gives the new signal waveforms in time domain for both polarizations $\tilde{q}_j(t)$, $j = 1, 2$ as a function of the old signal components $q_j(t)$, of the auxiliary solution $\bar{v}$, and of the new eigenvalue λ_0 we want to add to the nonlinear spectrum:

$$\tilde{q}_j(t) = q_j(t) + 2i(\lambda_0^* - \lambda_0)\frac{u_j^*}{1 + \sum_{s=1}^{2} |u_s|^2} \quad (j = 1, 2), \qquad (4.13)$$

where $u_j = \bar{v}_{j+1}/\bar{v}_1$. When one of the components of $q_{1,2}(t)$ is null, (4.13) reduces to the single polarization DT in (2.30).

The iterative procedure to generate the dual-polarization time domain signal associated with an arbitrary discrete nonlinear spectrum, starting from the "vacuum" solution $q_j(t) = 0$, $j = 1, 2$, is the same as the one presented in Section 2.3.5, whose pseudo-code is given in Algorithm 1. The procedure can be adapted to the dual-polarization case by replacing the signal update and the auxiliary solution update equations with those in (4.13) and (4.11), respectively. The initialization constants $\{A^{(k)}, B^{(k)}, C^{(k)}\}$ of the auxiliary solution $\bar{v}^{(k)} = (A^{(k)}e^{-i\lambda_k t}, B^{(k)}e^{i\lambda_k t}, C^{(k)}e^{i\lambda_k t})^T$ need to be set to $\{1, -b_1(\lambda_k), -b_2(\lambda_k)\}$, where $b_1(\lambda_k)$ and $b_2(\lambda_k)$ are the scattering coefficients that we want to associate to the eigenvalue λ_k for the two polarization components.

4.3 Numerical methods

This section reports the derivation of an algorithm based on the so-called trapezoidal discretization method. It allows computing the scattering coefficients from time domain signals in the MS with small numerical errors.

In Section 4.2.3 it was explained that, in order to compute the scattering coefficients $a(\lambda)$ and $b_{1,2}(\lambda)$, the Jost solution $\phi^N(t, \lambda)$ needs to be propagated from $t = -\infty$ to $t = +\infty$ by integrating (4.4a). Among the many integration methods available, from the simple Newton integration to the more complex Runge-Kutta method, it has been shown in [81] that the trapezoidal integration is one of the algorithms that provide the best results in term of numerical precision in the NFT context for the NLSE case. Moreover, in the same work, an improvement to the trapezoidal integration method was proposed. The method is called forward-backward, and it allows to increase the precision of the computation of the discrete scattering coefficients for the complex discrete eigenvalues. In Section 4.3.1, the proposed algorithm is extended to the

dual-polarization MZSP. In Section 4.3.2 the concept of trapezoidal integration is reviewed, and following the same procedure used in [81], the algorithm required to compute the direct NFT for the dual-polarization case is derived.

4.3.1   The trapezoidal discretization method

The initial value problem (IVP)

$$\frac{\mathrm{d}\psi(t)}{\mathrm{d}t} = \mathbf{A}(t)\psi(t), \quad \psi(T_1) = \psi_0 \tag{4.14}$$

where $\mathbf{A}(t)$ is a $n \times n$ matrix, admits the closed solution

$$\psi(t) = \exp\left(\int_{T_1}^{t} \mathbf{A}(\tau)d\tau\right)\psi_0 \tag{4.15}$$

if the matrix commutes with itself $\mathbf{A}(t_i)\mathbf{A}(t_j) = \mathbf{A}(t_j)\mathbf{A}(t_i)$ for any given t_i, t_j [81]. If $\mathbf{A}(t)$ does not satisfy the commutation property, it is possible to compute an approximate solution to (4.14) by proceeding as follows. First the time axis $[T1, T2]$ is discretized in N sections of length $h = (T_2 - T_1)/N$, and the the time instants $t_0 = T_1$, $t_N = T_2$, $t_n = T_1 + nh$, $1 \leq n < N$ are defined. Then $\mathbf{A}(t)$ is approximated with the piecewise constant matrix $\tilde{\mathbf{A}}(\tau)$, defined as

$$\tilde{\mathbf{A}}(t) = \begin{cases} \mathbf{A}(T_1) & T_1 \leq t < T_1 + h/2 \\ \mathbf{A}(t_n) & T_1 + nh - h/2 \leq t < T_1 + nh + h/2, \text{ and } 1 \leq n < N \\ \mathbf{A}(T_2) & T_2 - h/2 \leq t < T_2 \end{cases}$$

$$\tag{4.16}$$

for which the commutation property is valid within each specified time interval, so there exists a solution

$$\psi(t_{n+1}) = \exp\left(\int_{t_n}^{t_{n+1}} \tilde{\mathbf{A}}(\tau)d\tau\right)\psi(t_n), \quad 0 \leq n \leq N. \tag{4.17}$$

Iterating of the full time interval we can compute the solution at the instant T_2 starting from the initial solution ψ_0 at the instant T_1 as follows

$$\psi(T_2) = \prod_{n=N}^{0} \exp\left(\int_{t_n}^{t_{n+1}} \tilde{\mathbf{A}}(\tau)d\tau\right)\psi_0$$

$$= \exp\left(\frac{h}{2}\mathbf{A}(t_N)\right) \prod_{n=N-1}^{1} \exp\left(h\mathbf{A}(t_n)\right) \exp\left(\frac{h}{2}\mathbf{A}(t_0)\right)\psi_0 + R_e$$

being R_e the truncation error due to the piecewise approximation.

As explained in Section 4.2.3, in order to compute the direct NFT, it is necessary to solve the IVP for the time evolution equation of the MZSP

$$\frac{\partial v(t)}{\partial t} = \mathbf{P}(t)v(t)$$

$$= \begin{pmatrix} -i\lambda & q_1(t) & q_2(t) \\ -q_1^*(t) & i\lambda & 0 \\ -q_2^*(t) & 0 & i\lambda \end{pmatrix} v(t), \tag{4.18}$$

with initial condition $v(-\infty) = \phi^N(t, \lambda)|_{t=-\infty}$. Given the assumption that the signal must have a finite and symmetric support, so that $|q_j(t)| = 0$, $j = 1, 2$ for $t \notin [-T_0, T_0]$, we want to find the value of $v(t)$ at $t = T_0$ in order to compute the scattering coefficients $a(\lambda)$ and $b_{1,2}(\lambda)$.

To do this, it is first convenient to perform a change of variable and define the new vector ψ as follows

$$\psi = \begin{pmatrix} \psi_1 \\ \psi_2 \\ \psi_3 \end{pmatrix} = \begin{pmatrix} v_1 e^{i\lambda t} \\ v_2 e^{-i\lambda t} \\ v_3 e^{-i\lambda t} \end{pmatrix}. \tag{4.19}$$

The transformed IVP becomes

$$\frac{\partial \psi(t)}{\partial t} = \mathbf{F}(t)\psi(t)$$

$$= \begin{pmatrix} 0 & q_1(t)e^{2i\lambda t} & q_2(t)e^{2i\lambda t} \\ -q_1(t)^* e^{-2i\lambda t} & 0 & 0 \\ -q_2(t)^* e^{-2i\lambda t} & 0 & 0 \end{pmatrix} \psi(t), \tag{4.20}$$

with initial condition ψ_0, while the Jost solution becomes $\psi^N(-T_0) = (1, 0, 0)^T$. The scattering coefficients can be computed from the transformed vector as

$$a(\lambda) = \lim_{t \to \infty} \psi_1^N(t) \tag{4.21a}$$

$$b_1(\lambda) = \lim_{t \to \infty} \psi_2^N(t) \tag{4.21b}$$

$$b_2(\lambda) = \lim_{t \to \infty} \psi_3^N(t). \tag{4.21c}$$

Given that $\mathbf{F}(t)$ does not commute with itself for two arbitrary time instants, it is not possible to express the solution of (4.20) as a matrix exponential

in the form of (4.17). Nonetheless, as explained before, we can consider the discretized version of $\mathbf{F}(t)$, defined as in (4.16) with $T_1 = -T_0$ and $T_2 = T_0$

$$\tilde{\mathbf{F}}(t_n, \lambda) = \begin{pmatrix} 0 & q_1 e^{2i\lambda t_n} & q_2 e^{2i\lambda t_n} \\ -q_1^* e^{-2i\lambda t_n} & 0 & 0 \\ -q_2^* e^{-2i\lambda t_n} & 0 & 0 \end{pmatrix}. \tag{4.22}$$

Performing the eigenvalue decomposition and computing the exponential of this matrix we obtain

$$\mathbf{G}_n = e^{\mathbf{F}(t_n, \lambda)h} \tag{4.23}$$

$$= \begin{pmatrix} cos(ph) & \frac{q_1 e^{2i\lambda t_n} sin(ph)}{p} & \frac{q_2 e^{2i\lambda t_n} sin(ph)}{p} \\ -\frac{q_1^* e^{-2i\lambda t_n} sin(ph)}{p} & \frac{|q_2|^2 + |q_1|^2 cos(ph)}{p^2} & \frac{q_2 q_1^* (cos(ph)-1)}{p^2} \\ -\frac{q_2^* e^{-2i\lambda t_n} sin(ph)}{p} & \frac{q_1 q_2^* (cos(ph)-1)}{p^2} & \frac{|q_1|^2 + |q_2|^2 cos(ph)}{p^2} \end{pmatrix},$$

with $p = \sqrt{|q_1|^2 + |q_2|^2}$. It should be noted that $\mathbf{G}_n$ reduces to the NLSE case [81] if either q_1 or q_2 are identically zero. Now, we can calculate the $a(\lambda)$ and $b_{1,2}(\lambda)$ scattering coefficients starting from $\psi^N(-T_0)$ and using the rule in (4.18) as follows

$$\begin{pmatrix} a_N(\lambda) \\ b_{1N}(\lambda) \\ b_{2N}(\lambda) \end{pmatrix} = \mathbf{G}_N^{\frac{1}{2}} \mathbf{G}_{N-1} ... \mathbf{G}_2 \mathbf{G}_1 \mathbf{G}_0^{\frac{1}{2}} \begin{pmatrix} 1 \\ 0 \\ 0 \end{pmatrix}. \tag{4.24}$$

The presented algorithm can be used to compute both the continuous and the discrete nonlinear spectrum of the dual-polarization signal $q_{1,2}(t)$ with increased precision compared to other numerical methods as the forward Euler or the Crank-Nicolson [81]. If the nonlinear spectrum is purely discrete, the forward-backward trapezoidal method presented in the next section can be used to further increase the numerical precision in the computation of $b_{1,2}(\lambda_i)$.

4.3.2   Forward-backward method

As stated in [81], the forward-backward method can increase the numerical precision of the trapezoidal method when computing the $b_{1,2}(\lambda_i)$ for the case of complex discrete eigenvalues $\lambda_i \in \mathbb{C}^+$. Indeed, the coefficients $b_{1,2}(\lambda_i)$ are related to the second and third component of $\psi(t)$ which at every integration

step changes proportionally to $q(t)e^{2i\lambda_i t}$, as it can be seen from (4.20). Being the imaginary part of the eigenvalue strictly positive, when $T_0 \gg 1$, small errors in the estimation of λ_i can lead to big integration errors due to the real part of the exponential term.

If λ_i is a discrete eigenvalue, by definition $a(\lambda_i) = 0$, so that the projection in (4.6a) reduces to

$$\phi^N(t, \lambda_i) = \phi^P(t, \lambda_i) b(\lambda_i). \tag{4.25}$$

Since $b_{1,2}(\lambda_i)$ are time-invariant, they can be computed at any instant of time by solving the equation above. It is convenient to compute them at a time instant where the numerical error is small, for instance around $t_m = 0$.

To do this we can propagate the Jost solution $\phi^N(t, \lambda_i)$ forward from $-T_0$ to t_m, and the Jost solution $\phi^P(t, \lambda_i)$ backward from T_0 to t_m in the following way

$$w(t_m) = \mathbf{L}_N \begin{pmatrix} 1 \\ 0 \\ 0 \end{pmatrix} \tag{4.26a}$$

$$u(t_m) = \mathbf{R}_N^{-1} \begin{pmatrix} 0 & 0 \\ 1 & 0 \\ 0 & 1 \end{pmatrix} \tag{4.26b}$$

being $\mathbf{R}_N = \mathbf{G}_N^{\frac{1}{2}} \mathbf{G}_{N-1}...\mathbf{G}_{m+1}$ and $\mathbf{L}_N = \mathbf{G}_m...\mathbf{G}_2 \mathbf{G}_1 \mathbf{G}_0^{\frac{1}{2}}$ with $m = \lfloor cN \rfloor$ and $0 < c < 1$. From (4.25) we obtain simply that

$$\begin{pmatrix} w_1(t_m) \\ w_2(t_m) \\ w_3(t_m) \end{pmatrix} = \begin{pmatrix} u_{11}(t_m) & u_{12}(t_m) \\ u_{21}(t_m) & u_{22}(t_m) \\ u_{31}(t_m) & u_{32}(t_m) \end{pmatrix} \begin{pmatrix} b_1 \\ b_2 \end{pmatrix}, \tag{4.27}$$

which is a consistent overdetermined system of equations that can be easily solved.

4.4   Dual-polarization nonlinear frequency division multiplexing system

The general structure of a DP-NFDM system using the discrete spectrum is very similar to the single polarization one described in Chapter 3. This section presents a DP-NFDM system by describing the particular setup used in the

experiment from which the results in [J1, C2] were obtained. In this system the scattering coefficients associated to two discrete eigenvalues are modulated. Both the digital signal processing (DSP) and the experimental setup of this system is presented, and also the selection of the constellations of the $b_{1,2}(\lambda_i)$ scattering coefficients is discussed.

4.4.1 Constellations selection

The constellations of the scattering coefficients $b(\lambda_i)$ were chosen to reduce the peak-to-average power ratio (PAPR) of the time domain signal $E(\tau, \ell)$. The PAPR is defined as

$$\text{PAPR} = 10 \log \left(\frac{\max \left(|E_1|^2 + |E_2|^2 \right)}{P} \right), \qquad (4.28)$$

where $P = \frac{1}{T} \int_0^T \left(|E_1|^2 + |E_2|^2 \right) d\tau$ is the average power of the field, T is its time duration, and the index $i = 1, 2$ indicates the two field polarizations. The reason for this is that a signal with high PAPR has lower signal-to-quantization-noise ratio due to the limited resolution of the digital-to-analog converter (DAC) [116]. The signal is also more susceptible to distortion by the devices with a nonlinear characteristic such as Mach-Zehnder modulators (MZMs) and electrical amplifiers [88, 117]. It should be noted that practically is the PAPR of the single real or imaginary component of each polarization field that determines the degree of distortion, given that each of these components are converted by an individual DAC and drive a single branch of a MZM. The PAPR defined in (4.28) can be considered a worst case PAPR, and it has been used in order to optimize a single value instead of four thus reducing the complexity of the optimization procedure.

The time domain signal shape, bandwidth, duration, and power depend on the particular choice of the eigenvalues and the scattering coefficients $\{\lambda_1, \lambda_2, b_{1,2}(\lambda_1), b_{1,2}(\lambda_2)\}$. These parameters should be jointly optimized in order to minimize the PAPR while satisfying system-specific design constraints. In this experiment the constraint was to keep the duration of the signal smaller than the processing time-window, of a duration of one symbol period $T_s = 1\,\text{ns}$, to avoid cropping the signal. However, this optimization would have been computationally demanding given the large dimensionality of the parameters space $\mathbb{C}^6$.
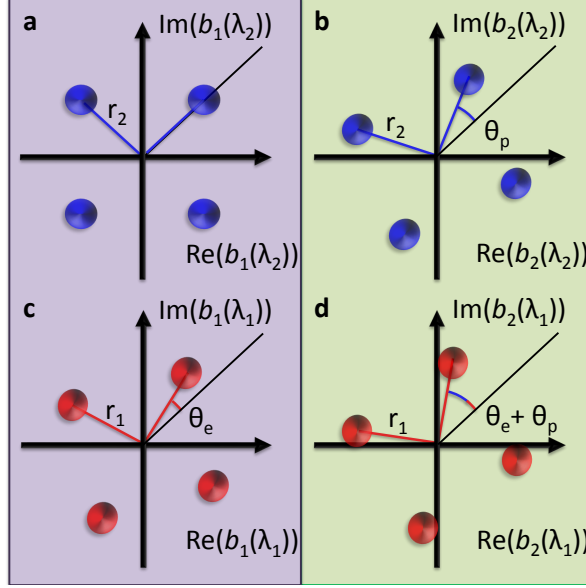
Figure 4.1: Representation of the constellations of the scattering coefficients
$b_{1,2}(\lambda_i)$, $i = 1, 2$ associated with the eigenvalue $\lambda_1 = i0.3$ (**c,d**)
and $\lambda_2 = i0.6$ (**a,b**) and with the first (**a,c**) and second (**b,d**)
polarization of the signal. The optimization angles θ_e and θ_p,
and the radii r_1 and r_2 are also shown.

For this reason some accuracy was sacrificed in order to simplify the opti-
mization procedure that nonetheless allowed reducing the PAPR of the signal
to a level that enabled to transmit over several hundreds of km.

Starting from a reference QPSK constellation $C_r = \exp\left(i\left(k\frac{\pi}{2} + \frac{\pi}{4}\right)\right)$ with
$k = 0, 1, 2, 3$, the set of constellations associated to the scattering coefficients
$\{b_1(\lambda_i), b_2(\lambda_i)\}, i = 1, 2$ corresponding to the eigenvalues $\{\lambda_1 = i0.3, \lambda_2 = i0.6\}$
was constructed as follows

$$\begin{pmatrix} C_{1,1} & C_{1,2} \\ C_{2,1} & C_{2,2} \end{pmatrix} = \begin{pmatrix} C_r r_1 \exp(i\theta_e) & C_r r_1 \exp(i\theta_e)\exp(i\theta_p) \\ C_r r_2 & C_r r_2 \exp(i\theta_p) \end{pmatrix}, \qquad (4.29)$$

where $C_{i,j}$ is the constellation associated to the eigenvalue i and the polariza-
tion j, r_i is the radius of the constellations associated to the eigenvalue λ_i, θ_e
is the relative rotation angle between the constellations associated to the two
different eigenvalues, and θ_p is the relative rotation angle between the constel-
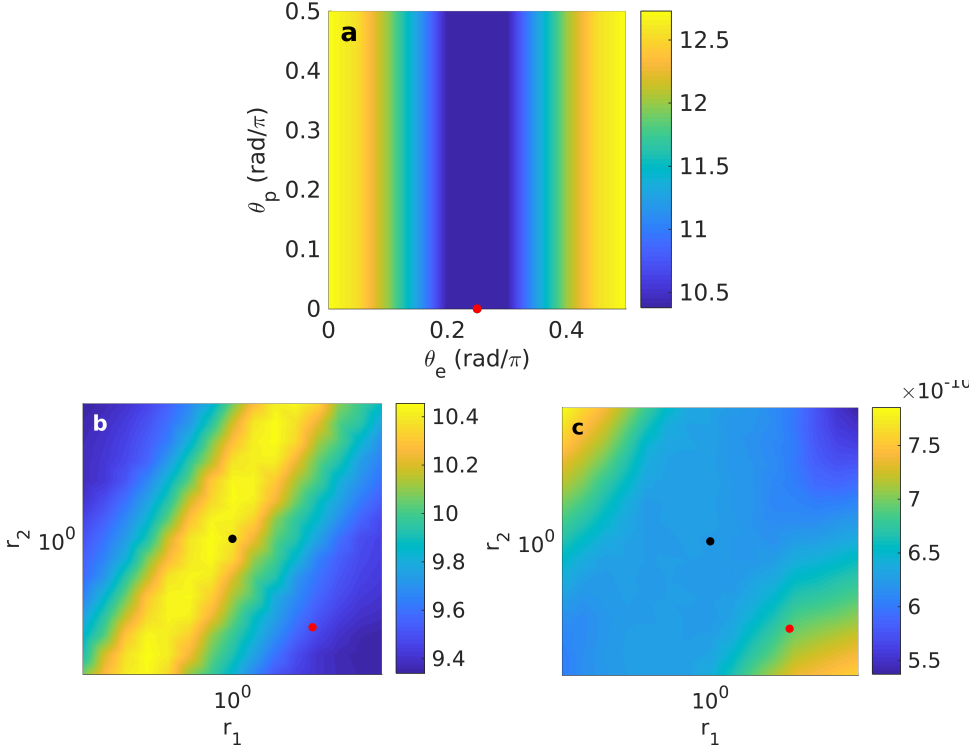
Figure 4.2: (**a**) PAPR (dB) of the signal as a function of the relative rotation angle θ_e between the constellations associated to the two different eigenvalues and the relative rotation angle θ_p between the constellations associated to the two different polarizations . The red point marks the values $(\theta_e = \pi/4, \theta_p = 0)$ found after the first step of the optimization (PAPR = 10.38 dB). (**b**) PAPR (dB) and (**c**) time duration (s) of the signal containing 99 % of its power as a function of the radii r_i of the constellations associated to the eigenvalue $\lambda_i, i = 1, 2$. The black point marks the radii used in the first step of the optimization ($r_1 = 1, r_2 = 1$), while the red one marks the optimized values ($r_1 = 5, r_2 = 0.14$) used in the experiment (PAPR = 9.49 dB).

lations associated to the two different polarizations. The four constellation diagrams are represented in Figure 4.1.

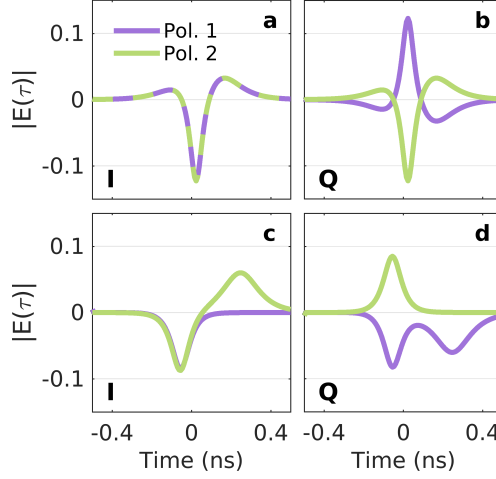The PAPR of the signal was optimized in two steps. First the two an-

Figure 4.3: (**a**) I and (**b**) Q components of one symbol of the signal when all the four constellations are equal to the reference constellation C_r (PAPR = 12.73). (**c**) I and (**d**) Q components corresponding to the constellations used in the experiment (PAPR = 9.49). The violet (Polarization 1) and green (Polarization 2) curves indicates the components associated to the two polarizations.

gles (θ_e, θ_p) were optimized by sweeping their values between 0 and π while having $r_1 = r_2 = 1$. The optimum value of PAPR found is 10.38 dB for $(\theta_e = \pi/4, \theta_p = 0)$, which is lower by 2.35 dB compared to the worst case where all four constellations are equal (PAPR = 12.73 dB) as shown in Figure 4.2 (a). Note that the optimal value $\theta_e = \pi/2$ found confirms the results in Section 3.1.1 and in others previous experimental works on the single polarization case [94, 118]. The PAPR seems to be independent on θ_p. To further reduce the PAPR, the two radii (r_1, r_2) were then optimized. By varying the radii of the constellations associated to the two eigenvalues, it is possible to partially separate the time domain signal components associated to the two eigenvalues. This allows reducing the PAPR at the cost of a longer time duration of the signal, as shown in Figure 4.2 (b-c). By choosing the set of radii $(r_1 = 5, r_2 = 0.14)$, the PAPR results finally in 9.49 dB, while the time duration of the signal containing 99% of its power is still within the symbol period T_s of 1 ns. In Figure 4.3 the in-phase (I) and quadrature (Q) components of one symbol of the time domain signal are shown before and after the optimization of the PAPR.
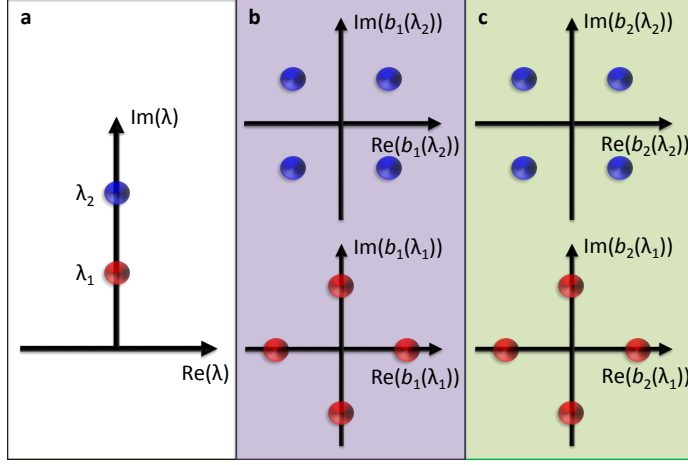
Figure 4.4: Ideal normalized constellations are illustrated schematically: in
(**a**) the discrete eigenvalues $\lambda_1 = i0.3$ and $\lambda_2 = i0.6$ are depicted.
The scattering coefficients $b_{1,2}(\lambda_i)$, $i = 1, 2$, associated with the
two orthogonal polarization components of the signal, are shown
in (**b**) and (**c**), respectively. Polarization 1 and Polarization 2
on a violet and green background, respectively. The scattering
coefficients associated with λ_1 are chosen from a QPSK constel-
lation of radius 5 and rotated by $\pi/4$ while those associated with
λ_2 from a QPSK constellation and radius 0.14.

4.4.2 Transmitter and receiver digital signal processing

At the transmitter the data bits are mapped to the scattering coefficients pairs
$\{b_1(\lambda_i), b_2(\lambda_i)\}$ for $i = 1, 2$ where the eigenvalues $\{\lambda_1 = i0.3, \lambda_2 = i0.6\}$ are
used for each symbol. We refer to this set of coefficients, and equivalently to
the associated time domain waveform, as a DP-NFDM symbol. The scattering
coefficients associated with the first eigenvalue can assume values drawn from
a QPSK constellation of radius 5 and rotated by $\pi/4$ while those associated
with the second eigenvalue are drawn from a QPSK constellation of radius
0.14, as shown in Figure 4.4. The waveform associated to each DP-NFDM
symbol is generated using the DT described in Section 4.2.4, followed by the
denormalization in (4.3) with normalization parameter $T_0 = 47\,\mathrm{ps}$. This choice
of T_0 allows fitting the waveform within the symbol period $T_s = 1\,\mathrm{ns}$ ($1\,\mathrm{GBd}$)
with enough time guard bands among successive DP-NFDM symbols, thus
satisfying the vanishing boundary conditions required to correctly compute

the NFT. The power P_{Tx} of the digital signal thus obtained is later used to set the power of the corresponding transmitted optical signal.

The channel is assumed to be a link of SMFs with erbium-doped fiber amplifier (EDFA) lumped amplification as in the experiment. In order to take into account the presence of the losses, the LPA approximation is used in the normalization and denormalization steps of the waveform before computing the NFT and after computing the INFT, respectively.

At the receiver, the digital signal output by the digital storage oscillo-scope (DSO) is first rescaled so that its power is P_{Tx} (the power of the trans-mitted optical signal). Then an ideal rectangular filter with a bandwidth equal to the 99% power bandwidth of the signal is used to filter the out-of-band noise. At this point, cross-correlation-based frame synchronization using training se-quences is performed in order to optimally align the DP-NFDM symbol to the processing time-window of duration $T_s = 1\,\text{ns}$. For each DP-NFDM symbol, first the eigenvalues are located using the Newton-Raphson search method employing the one-directional trapezoidal method, and then the coefficients $b_{1,2}(\lambda_i)$ are computed on the found eigenvalues using the forward-backward trapezoidal method. The homodyne configuration of the receiver allows not having a frequency offset between the transmitter laser and the coherent re-ceiver local oscillator (LO), but given the non-zero combined linewidth of the two lasers (~1kHz) their coherence length is limited to about $90\,\text{km}$. This implies that the received constellations are affected by phase noise when the transmission distance exceeds the coherence length of the laser, causing errors in the detection of the symbols. The phase noise is removed by applying the blind phase search (BPS) algorithm [119] in the NFT domain to each con-stellation individually. Finally, the scattering coefficients are rotated back to remove the phase factor acquired during the transmission (given in (4.8b)), and the decision on the symbols is taken using a minimum Euclidean dis-tance decisor, as the one presented in Section 3.2.6, which operates over the scattering coefficients space.

4.4.3   Experimental setup

The experimental setup and the block diagrams of the DSP are depicted in Figure 4.5. At the transmitter a fiber laser (FL) with sub-kHz linewidth is modulated using an integrated dual-polarization I/Q modulator driven by an arbitrary waveform generator (AWG) with $20\,\text{GHz}$ analog bandwidth and $64\,\text{GSa/s}$. Before uploading it to the AWG, the signal generated by the INFT
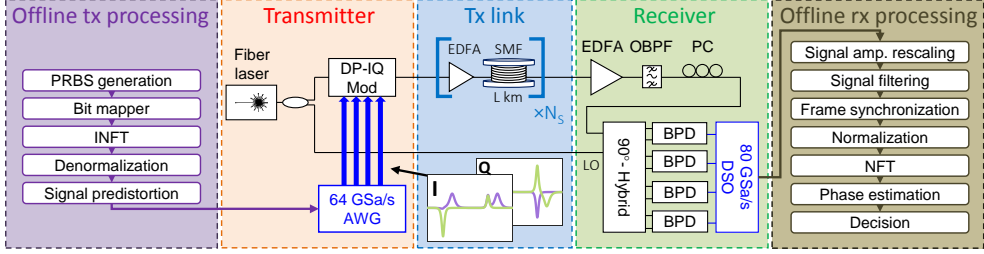
Figure 4.5: Experimental setup with transmitter and receiver DSP chains. Abbreviations not defined in the main text: BPD.

is pre-distorted using the ideal inverse transfer function of the MZM ($\mathrm{asin}(\cdot)$). This pre-distortion is required in order to have a good trade-off between signal-to-noise ratio (SNR) at the output of the MZM and signal distortions caused by its nonlinear transfer function. Nonetheless, given the still high PAPR of the optimized waveform considered (see Section 4.4.1), this pre-distortion is not optimal and advanced methods can be employed to improve further the quality of the transmitted signal [45]. The channel is a fiber link composed of up to nine spans of SMF with dispersion parameter $D = 17.5\,\mathrm{ps/(nm\,km)}$, nonlinear parameter $\gamma = 1.25\,\mathrm{W}^{-1}\,\mathrm{km}^{-1}$, fiber-loss parameter $\alpha = 0.195\,\mathrm{dB/km}$, and PMD coefficient $< 0.1\,\mathrm{ps\,km}^{-1/2}$. Two different span lengths $L_s = 41.5\,\mathrm{km}$ and $L_s = 83\,\mathrm{km}$ were employed. Considering these channel parameters, the complex baseband signal generated by the INFT with LPA and denormalized has the following properties: 99% of its power contained within a bandwidth W of 12.7 GHz, a PAPR of 9.49 dB and an average power P_{Tx} of 5.30 dBm and 7.70 dBm for the span lengths $L_s = 41.5\,\mathrm{km}$ and $L_s = 83\,\mathrm{km}$, respectively. Given these channel and signal parameters we have that the soliton period, defined as $(\pi/2)L_d$, with $L_d = (W|\beta_2|)^{-1}$ the dispersion length [29, 70], is 436 km. Being this much larger than the typical birefringence correlation length, which is on a scale of few tens of meters [114], guarantees the applicability of the Manakov averaged model.

In order to properly match the transmitted signal to the channel, the gain of the EDFA at the transmitter is tuned in such a way to set the power of the optical signal to P_{Tx}. The optical signal is then transmitted through the channel.

At the receiver, the signal was first sent through a 0.9 nm optical band pass filter (OBPF), and then a polarization controller (PC) was used to manually
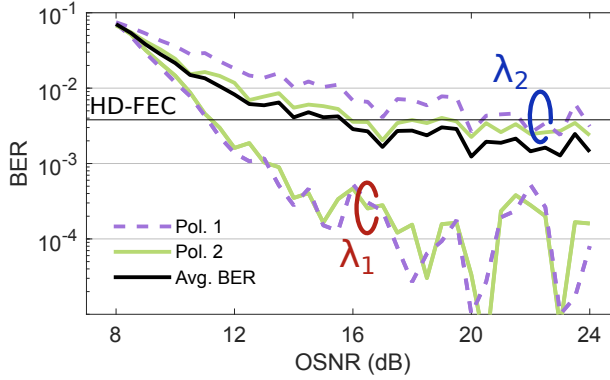
Figure 4.6: System performance in terms of BER as a function of the OSNR in a back-to-back configuration. The BER of the individual constellations are shown by the violet (Polarization 1) and green (Polarization 2) curves and are grouped per eigenvalue ($\lambda_1 = i0.3, \lambda_2 = i0.6$). The black curve represents the average BER over the four constellations.

align the polarization of the signal to the optical front-end. The use of the PC was required to avoid using of polarization tracking algorithms for the NFT signals, which were not available at the time of the experiment. In the future it could be possible to use modulation independent polarization tracking algorithms, as an example using independent components analysis [120]. The signal is then detected by using a standard coherent receiver (33 GHz analog bandwidth, 80 GSa/s), in a homodyne configuration where the transmitter laser is used as LO. The acquired digital signal consisting of five blocks of 10^5 DP-NFDM symbols is then fed to the receiver DSP chain described previously.

4.5   Experimental results

The system was initially tested in a back-to-back (B2B) configuration, where the transmitter output has been directly connected to the receiver, in order to obtain the best performance achievable by the system in the sole presence of the intrinsic transceiver distortions (e.g. transmitter front-end distortions, detectors noise, etc.) and added additive white Gaussian noise (AWGN) as commonly done for linear coherent system. The optical signal-to-noise ra-
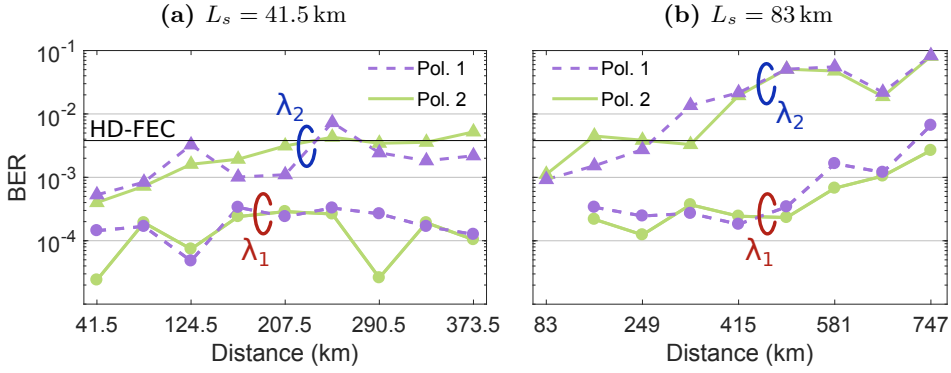
Figure 4.7: System performance in terms of BER as a function of the transmission distance for the four individual constellations for span lengths of $L_s = 41.5\,\text{km}$ (**a**) and $L_s = 83\,\text{km}$ (**b**). The violet (Polarization 1) and green (Polarization 2) curves are grouped per eigenvalue ($\lambda_1 = i0.3,\ \lambda_2 = i0.6$).

tio (OSNR) was swept by varying the noise power added to the signal at the receiver input. The adopted metric for measuring the performances allows a direct comparison with standard coherent transmission systems. The OSNR range considered is the region of interest where the system performance is around the HD-FEC threshold. The measured average BER is shown in Figure 4.6. A visible effect is the fact that the BER is not the same for the four different constellations, but it is worse for the two constellations associated with the eigenvalue with the largest imaginary part. This effect can be related to the dependency of the noise variance of both the eigenvalues and the corresponding scattering coefficient on the imaginary part of the eigenvalues themselves [32, 40, 55, 91, 92].

In order to demonstrate a fiber transmission with the proposed system, we transmitted over a link of N_s spans of SMF with span length $L_s = 41.5\,\text{km}$ and $L_s = 83\,\text{km}$. The maximum available OSNR at the transmitter is $35\,\text{dB}$. The performance in terms of BER as a function of the transmission distance is shown in Figure 4.7 (a-b) for the four constellations. The difference in the performance in the two eigenvalues appears in this case too. This can also be seen from the constellation plots after $373.5\,\text{km}$ in Figure 4.8, where the two constellations associated with λ_2 are sensibly more degraded than those related to λ_1, which are still well defined. Similar performance can instead be
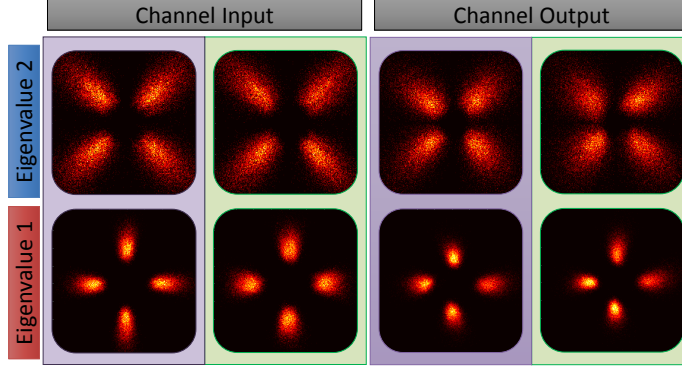
Figure 4.8: The four experimental constellations of the scattering coefficients $b_{1,2}(\lambda_i)$, $i = 1, 2$ associated with the two eigenvalues ($\lambda_1 = i0.3$, $\lambda_2 = i0.6$) are shown at the transmitter side (left) and after $373.5\,\mathrm{km}$ transmission with $41.5\,\mathrm{km}$ spans (right). Polarization 1 and Polarization 2 on a violet and green background, respectively.

Figure 4.9: (**a,f**) distribution of the imaginary part of the received eigenvalues (reference eigenvalues ($\lambda_1 = i0.3, \lambda_2 = i0.6$)), and phase noise distribution of the scattering coefficients $b_{1,2}(\lambda_i)$, for the transmission distances of (**b-e**) $373.5\,\mathrm{km}$ and (**g-l**) $332\,\mathrm{km}$ using spans of $41.5\,\mathrm{km}$ and $83\,\mathrm{km}$, respectively.

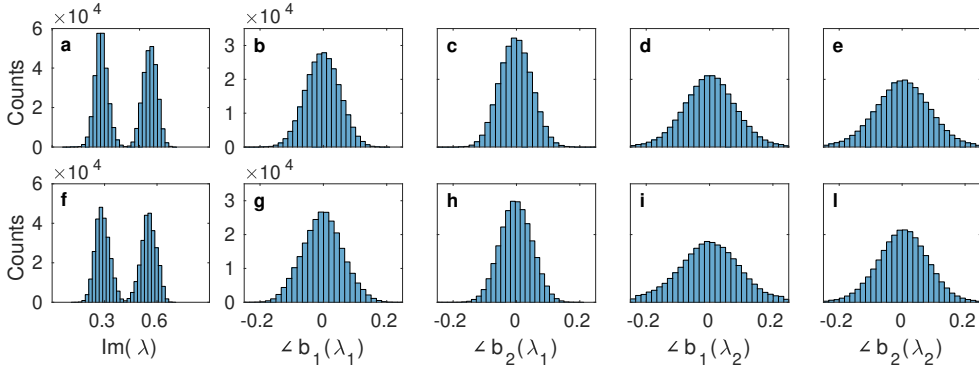| Spectral parameter	Noise variance	
	41.5 km case	80.5 km case
$Im(\lambda_1)$	1.54×10^{-3}	18.06×10^{-3}
$Im(\lambda_2)$	1.70×10^{-3}	20.39×10^{-3}
$\angle b_1(\lambda_1)$	27.77×10^{-3}	39.00×10^{-3}
$\angle b_2(\lambda_1)$	24.86×10^{-3}	24.62×10^{-3}
$\angle b_1(\lambda_2)$	65.05×10^{-3}	88.40×10^{-3}
$\angle b_2(\lambda_2)$	72.45×10^{-3}	61.52×10^{-3}

Table 4.1: Variance of the imaginary part of the eigenvalues ($\lambda_1 = i0.3, \lambda_2 = i0.6$) and of the phase of the corresponding scattering coefficients $b(\lambda_i)$ for the transmission distances of 373.5 km and 332 km when spans of 41.5 km and 83 km are used, respectively. Each variance value has been computed over 250 000 symbols.

seen in the two different polarizations of the same eigenvalue.

An analysis of the noise distribution on the eigenvalues and scattering coefficients $b_{1,2}(\lambda_i)$ has been done for the transmission distances of 373.5 km and 332 km performed in the experiment when spans of 41.5 km and 83 km were used, respectively. In Figure 4.9 the histograms of the received eigenvalues (a,f) and scattering coefficients (b-e, g-l) are shown. The variances of the imaginary part of the received eigenvalues and those of the phase of the scattering coefficients are reported in Table 4.1. It is observed that in both cases the variance of the imaginary part of the eigenvalue $\lambda_2 = i0.6$ is about 10% higher than the one of $\lambda_1 = i0.3$. The proportionality of the noise variance on the imaginary part of the eigenvalue is consistent with the predictions made by the model in [91] for the single eigenvalue case. The variance of the phase of the scattering coefficients $b_1(\lambda_2)$ and $b_2(\lambda_2)$ associated to λ_2 are 2.34 and 2.91 times those of the scattering coefficients $b_1(\lambda_1)$ and $b_2(\lambda_1)$, respectively for the 41.5 km case, and 2.27 and 2.50 for the 83 km case.

Finally in Figure 4.10 the average BER for the two span lengths used in the test is compared in order to check the impact of the LPA approximation. As explained in Section 2.4, worse performances are expected when longer spans are used. The BER curve for the 41.5 km span contains two outlier points at 124.5 km and 249 km that are slightly worse than the general trend of the curve. This is believed to be caused by instabilities in the setup when the related experimental traces were acquired, in particular, an incorrect alignment of
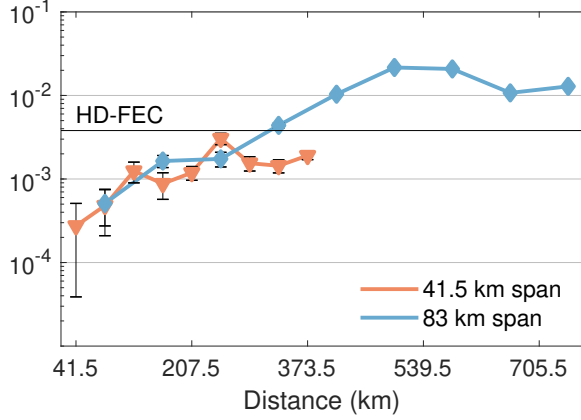
Figure 4.10: Comparison of the average BER as a function of the transmission distance between links of 41.5 km and 83 km. The error bars represent the standard deviation over five processed blocks of 10^5 DP-NFDM-symbols.

the polarization to the receiver due to a drift in the polarization state of the received signal. Besides these two points, the rest of the 41.5 km curve lies under the one for the 83 km spans, confirming that the use of longer spans adds a slight degradation in the performance of the system. From the 83 km spans curve we can also note that the BER decreases towards the end of the link. This unusual behavior may be explained by the fact that the bandwidth of the signal varies along the link as explained in Section 3.2.2, which, combined with a sub-optimal receiver (limited analog-to-digital converter (ADC) resolution, numerical accuracy of NFT algorithms) may lead to a non-monotonic BER curve due to particularly bad BER conditions of the signal at specific distances; in this case towards the middle of the link. maximum reach of the system achieved with BER under the HD-FEC threshold is 373.5 km using 41.5 km spans and 249 km with spans of 83 km.

It should be noted that in the experimental setup, the PMD effect was not compensated for. However, for the transmission lengths and PMD values of the standard SMF employed, the accumulated differential group delay is negligible if compared with the pulse duration [7]. The impact of PMD is therefore not expected to have had a major impact on the results shown. New approaches have been developed to compensate for PMD effects in linear transmission systems [121], and a recent work has shown in simulation that

for a DP-NFDM system employing the continuous spectrum, PMD effects could be compensated in the nonlinear domain by using a linear equalizer [66]. Similar techniques may be applied to discrete DP-NFDM systems.

4.6   Summary

In this chapter the theory that describes the dual-polarization NFT has been presented. The direct and inverse transformations between the time domain and the nonlinear domain have been described concentrating on the case of a purely discrete nonlinear spectrum. A numerical method, based on the trapezoidal discretization method, to solve the direct NFT has been proposed. Moreover, the structure of a DP-NFDM optical communication system employing two orthogonal modes of polarization was described for the specific case of a discrete nonlinear spectrum with two eigenvalues. The proposed system was then demonstrated experimentally for the first time, showing a transmission of eight bits of information per DP-NFDM symbol, with transmission distances up to $373.5\,\mathrm{km}$.

CHAPTER 5

Conclusion

The increasing global data traffic is currently pushing linear single-mode fiber (SMF) coherent optical communication systems to their limits. Communication technologies based on the nonlinear Fourier transform (NFT) have recently emerged as possible candidates to tackle the nonlinearity problem by designing systems that integrate the nonlinearities in their operation.

This thesis presented a review of the nonlinear frequency division multiplexing (NFDM) modulation scheme based on the NFT and extended it to the dual-polarization case. Both the mathematical tools necessary to define dual-polarization nonlinear frequency division multiplexing (DP-NFDM) and a practical experimental demonstration of transmission have been given. These results could allow doubling the transmission rate of NFDM systems, and thus are a key step in the advance of this technology.

A summary of the results and an outlook on the possible future research directions are given in the following sections.

5.1   Summary

Chapter 2 reviewed the inverse scattering method based on the ideal channel model given by the integrable nonlinear Schrödinger equation (NLSE). Given the limited ability of the NLSE to model real SMFs, the generalized NLSE that accounts for the fiber loss and the noise has also been introduced. A numerical analysis of the behavior of the NFT continuous spectrum over this non-integrable channel has been done to investigate the impact of the two non-ideal terms. The analysis compared the amount of distortion, in terms of normalized mean squared error (NMSE), of the NFT continuous spectrum to that of the linear Fourier spectrum of a Gaussian pulse. The results have shown that the NFT continuous spectrum is distorted by nonlinearities as the launch power is increased, as opposed to the case where the channel is modeled by the integrable NLSE. Nonetheless, when compared to the Fourier spectrum, the NFT continuous spectrum was less distorted in terms of the

measured NMSE between input and output spectra. The NMSE was indeed 2.85 times lower for the NFT at the optimal launched power, which was $3\,\mathrm{dB}$ higher than the one of the linear Fourier spectrum. This shows that the NFT can be used over channels that do not satisfy all the conditions of the integrable NLSE still providing advantages over linear communication schemes employing the linear spectrum of the signal.

Chapter 3 described in detail an NFDM system using the discrete nonlinear spectrum for encoding information. The aim was to give an overview of the properties of such a system, based on the state-of-the-art literature. For each digital signal processing (DSP) block of the NFDM transceiver, the particular design challenges were discussed. Among the topics mentioned, the design of the nonlinear spectrum constellations is an interesting open problem. Some examples of optimization of the constellations to minimize the peak-to-average power ratio (PAPR) and duration of the time domain signal have been given. Then, the signal amplitude rescaling operation of the signal at the receiver was described. The impact of the power offset on the BER performance of the system was evaluated through numerical simulations. It was shown that in the presence of noise the optimal rescaling power does not match with the theoretical one. In the specific case considered of a 2-eigenvalue NFDM system, it was possible to obtain a gain in optical signal-to-noise ratio (OSNR) of $1\,\mathrm{dB}$ by rescaling the power of the signal using the information on the OSNR. Finally, the specific implementation of the symbol decisor used in this thesis was described. The decisor accounts for the effects peculiar to the discrete NFDM system, such as the disappearance of some eigenvalues and the problem of sorting the $b(\lambda_i)$ scattering coefficients to match them to the correct reference constellations. The chapter covered some of the main design aspects of an NFDM system, giving the reader an overview of this technology, and showing the differences with respect a standard linear coherent system.

Chapter 4 presented the novel concept of DP-NFDM. At first the mathematical theory of the inverse scattering for solving the Manakov system (MS) was revised. This theory defines the forward and inverse NFT transformations that can be used to encode and decode data in the nonlinear spectrum. The structure of a DP-NFDM was described for a specific system employing two discrete eigenvalues and quadrature phase-shift keying (QPSK) modulated $b(\lambda_i)$ scattering coefficients. Following the discussion on the design of the constellations in Chapter 3, the constellations of this system were designed to reduce the PAPR of the time domain signal of the system, which was found a limiting factor of the bit error rate (BER) performance. Through the optimization procedure used, the PAPR was reduced by $2.35\,\mathrm{dB}$. The proposed

DP-NFDM system was then demonstrated experimentally for the first time. It was possible to transmit 8 Gb/s up to 373.5 km with BER lower than the hard-decision forward error correction (HD-FEC) threshold. Although more research work needs to be done in this direction, by demonstrating the possibility of using dual polarization NFT-based channels, this thesis successfully met one of the key challenges that were explicitly highlighted in a recent review of this research field [29] as necessary steps in order to bring eigenvalue communication from a pioneering stage to be a working infrastructure for optical communications in the real world. Furthermore, the demonstration of the polarization division multiplexing is a significant step forward towards a fair comparison of the NFT-based channels with the currently used linear ones where polarization division multiplexing is an established practice.

5.2   Outlook

The results presented in this thesis demonstrated the feasibility of dual-polarization NFT-based communication, which enables exploiting the second polarization supported by the SMFs. Although this is a significant step forward in the evolution of NFT-based optical communication systems that can potentially double the transmission rate, the throughput and the spectral efficiencies of the demonstrated system were very limited.

A short term research may first address some of the limitations of the presented system. For example, the lack of DSP algorithms to track the state of polarization of the two components of the optical signal is a critical missing building block that needs to be implemented to make the system complete. Moreover, the demonstrated system was limited in the modulation of only the discrete nonlinear spectrum. To benefit from all the degrees of freedom of the nonlinear spectrum, the DP-NFDM needs to be equipped with a transformation able to generate a time domain signal from an arbitrary spectrum. This is likely possible by combining the Darboux transformation (DT) with the inverse nonlinear Fourier transform (INFT) for the continuous spectrum, recently proposed in [66], similarly to what has been done for the single polarization case in [43]. Investigations of the impact of the polarization mode dispersion (PMD) on the performance of the DP-NFDM systems are also necessary to verify that this is not a limiting factor in general.

On a longer term, one of the crucial problems of NFDM systems, which is still unanswered, is to demonstrate the possibility of creating a nonlinear add-drop multiplexer (ADM) able to extract an NFDM channel without altering

the nonlinear spectrum of the neighboring channels. As for now this is only possible by digitally demodulating and remodulating the nonlinear spectrum, which unfortunately does not seem anywhere near a practical solution given the limited speed of the electronics components. Moreover, further fundamental models that describe the impact of the fiber loss and the noise, which makes the Manakov system not integrable, on the evolution of the nonlinear spectrum are essential in order to properly design DP-NFDM receivers able to mitigate the impact of these non-ideal effects.

Despite the potentiality of DP-NFDM to be a technology that can offer advantages in terms of nonlinearity resilience, solutions to the problems mentioned above need to be found before it can compete with the technologically mature linear coherent systems.

Bibliography

[1] Cisco, "Cisco visual networking index: Forecast and methodology, 2016–2021," *CISCO White paper*, 2017.

[2] G. P. Agrawal, *Fiber-optic communication systems*, 4th ed. John Wiley & Sons, 2012.

[3] M. Seimetz, *High-order modulation for optical fiber transmission*. Springer, 2009.

[4] Ciena. (2013). Coherent optical turns 5: Here's how it was made, [Online]. Available: `http://www.ciena.com/insights/articles/Coherent-optical-turns-5-Heres-how-it-was-made-prx.html`.

[5] E. Agrell, M. Karlsson, A. R. Chraplyvy, D. J. Richardson, P. M. Krummrich, P. Winzer, K. Roberts, J. K. Fischer, S. J. Savory, B. J. Eggleton, M. Secondini, F. R. Kschischang, A. Lord, J. Prat, I. Tomkos, J. E. Bowers, S. Srinivasan, M. Brandt-Pearce, and N. Gisin, "Roadmap of optical communications," *Journal of Optics*, vol. 18, no. 6, 2016.

[6] C. Shannon, "A mathematical theory of communication," *The Bell System Technical Journal*, vol. 27, no. 3, pp. 379–423, 1948.

[7] G. P. Agrawal, *Nonlinear Fiber Optics*, 5th ed. Academic Press, 2012.

[8] P. Poggiolini, "The GN model of non-linear propagation in uncompensated coherent optical systems," *Journal of Lightwave Technology*, vol. 30, no. 24, pp. 3857–3879, 2012.

[9] P. P. Mitra and J. B. Stark, "Nonlinear limits to the information capacity of optical fiber communications," *Nature*, vol. 411, pp. 1027–1030, 2001.

[10] R. J. Essiambre, P. J. Kramer, G. J. Foschini, and B. Goebel, "Capacity limits of optical fiber networks," *Journal of Lightwave Technology*, vol. 28, pp. 662–701, 2010.

[11] A. Mecozzi and R.-J. Essiambre, "Nonlinear shannon limit in pseu-
      dolinear coherent systems," *Journal of Lightwave Technology*, vol. 30,
      no. 12, pp. 2011–2024, 2012.

[12] E. Ip and J. Kahn, "Compensation of dispersion and nonlinear impair-
      ments using digital backpropagation," *Journal of Lightwave Technology*,
      vol. 26, pp. 3416–3425, 2008.

[13] R. Dar and P. J. Winzer, "Nonlinear interference mitigation: Methods
      and potential gain," *Journal of Lightwave Technology*, vol. 35, no. 4,
      pp. 903–930, 2017.

[14] I. Sackey, F. Da Ros, J. K. Fischer, T. Richter, M. Jazayerifar, C.
      Peucheret, K. Petermann, and C. Schubert, "Kerr nonlinearity miti-
      gation: Mid-link spectral inversion versus digital backpropagation in
      5× 28-GBd pdm 16-QAM signal transmission," *Journal of Lightwave
      Technology*, vol. 33, no. 9, pp. 1821–1827, 2015.

[15] A. D. Ellis, M. Tan, M. A. Iqbal, M. A. Z. Al-Khateeb, V. Gordienko,
      G. S. Mondaca, S. Fabbri, M. F. C. Stephens, M. E. McCarthy, A. Per-
      entos, I. D. Phillips, D. Lavery, G. Liga, R. Maher, P. Harper, N. Doran,
      S. K. Turitsyn, S. Sygletos, and P. Bayvel, "4 Tb/s transmission reach
      enhancement using 10×400 Gb/s super-channels and polarization in-
      sensitive dual band optical phase conjugation," *Journal of Lightwave
      Technology*, vol. 34, no. 8, pp. 1717–1723, April 2016.

[16] X. Liu, "Twin-wave-based optical transmission with enhanced linear
      and nonlinear performances," *Journal of Lightwave Technology*, vol. 33,
      no. 5, pp. 1037–1043, 2015.

[17] D. Richardson, J. Fini, and L. Nelson, "Space-division multiplexing in
      optical fibres," *Nature Photonics*, vol. 7, no. 5, pp. 354–362, 2013.

[18] B. Puttnam, R. Luís, W. Klaus, J. Sakaguchi, J.-M. D. Mendinueta, Y.
      Awaji, N. Wada, Y. Tamura, T. Hayashi, M. Hirano, *et al.*, "2.15 Pb/s
      transmission using a 22 core homogeneous single-mode multi-core fiber
      and wideband optical comb," in *Proc. of the European Conference on
      Optical Communication (ECOC)*, 2015.

[19] A. Yi, L. Yan, Y. Pan, L. Jiang, Z. Chen, W. Pan, and B. Luo, "Trans-
      mission of multi-dimensional signals for next generation optical commu-
      nication systems," *Optics Communications*, vol. 408, pp. 42–52, 2018.

[20] A. Hasegawa and F. Tappert, "Transmission of stationary nonlinear optical pulses in dispersive dielectric fibers. I. Anomalous dispersion," *Applied Physics Letters*, vol. 23, no. 3, pp. 142–144, 1973.

[21] M. Nakazawa, E. Yamada, H. Kubota, and K. Suzuki, "10 Gbit/s soliton data transmission over one million kilometres," *Electronics Letters*, vol. 27, no. 14, pp. 1270–1272, 1991.

[22] L. Mollenauer and K. Smith, "Demonstration of soliton transmission over more than 4000 km in fiber with loss periodically compensated by Raman gain," *Optics letters*, vol. 13, no. 8, pp. 675–677, 1988.

[23] A. Hasegawa and T. Nyu, "Eigenvalue communication," *Journal of Lightwave Technology*, vol. 11, pp. 395–399, 1993.

[24] M. J. Ablowitz, D. J. Kaup, A. C. Newell, and H. Segur, "The inverse scattering transform-Fourier analysis for nonlinear problems," *Studies in Applied Mathematics*, vol. 53, no. 4, pp. 249–315, 1974.

[25] A. Shabat and V. Zakharov, "Exact theory of two-dimensional self-focusing and one-dimensional self-modulation of waves in nonlinear media," *Soviet physics JETP*, vol. 34, no. 1, p. 62, 1972.

[26] A. Hasegawa and M. Matsumoto, "Optical solitons in fibers," in *Optical Solitons in Fibers*, Springer, 2003, pp. 41–59.

[27] H. Terauchi and A. Maruta, "Eigenvalue modulated optical transmission system based on digital coherent technology," in *Proc. of the OptoElectronics and Communications Conference held jointly with 2013 International Conference on Photonics in Switching (OECC/PS)*, 2013, pp. 1–2.

[28] M. I. Yousefi and F. R. Kschischang, "Information transmission using the nonlinear Fourier transform, part I: Mathematical tools," *IEEE Transactions on Information Theory*, vol. 60, no. 7, pp. 4312–4328, Jul. 2014.

[29] S. K. Turitsyn, J. E. Prilepsky, S. T. Le, S. Wahls, L. L. Frumin, M. Kamalian, and S. A. Derevyanko, "Nonlinear Fourier transform for optical data processing and transmission: Advances and perspectives," *Optica*, vol. 4, no. 3, pp. 207–322, 2017.

[30] Z. Dong, S. Hari, T. Gui, K. Zhong, M. Yousefi, C. Lu, P.-K. A. Wai, F. Kschischang, and A. Lau, "Nonlinear frequency division multiplexed transmissions based on NFT," *IEEE Photonics Technology Letters*, vol. PP, no. 99, 2015.

[31] T. Gui, Z. Dong, C. Lu, and A. P. T. Lau, "The impact of receiver iq imbalance on multi-soliton NFDM transmissions with OOK modulation," in *Proc. of the Asia Communications and Photonics Conference*, 2015, paper ASu3F3.

[32] S. Hari, M. I. Yousefi, and F. R. Kschischang, "Multieigenvalue communication," *Journal of Lightwave Technology*, vol. 34, no. 13, pp. 3110–3117, 2016.

[33] V. Aref, Z. Dong, and H. Buelow, "Design aspects of multi-soliton pulses for optical fiber transmission," in *Proc. of the IEEE Photonics Conference (IPC)*, 2016, pp. 224–225.

[34] S. T. Le and H. Buelow, "64× 0.5 gbaud nonlinear frequency division multiplexed transmissions with high order modulation formats," *Journal of Lightwave Technology*, vol. 35, no. 17, pp. 3692–3698, 2017.

[35] I. Tavakkolnia and M. Safari, "Signaling on the continuous spectrum of nonlinear optical fiber," *Optics Express*, vol. 25, no. 16, pp. 18 685–18 702, August 2017.

[36] X. Yangzhang, M. Yousefi, A. Alvarado, D. Lavery, and P. Bayvel, "Nonlinear frequency-division multiplexing in the focusing regime," in *Proc. of the Optical Fiber Communication Conference (OFC)*, 2017, paper Tu3D.1.

[37] V. Aref, H. Bülow, K. Schuh, and W. Idler, "Experimental demonstration of nonlinear frequency division multiplexed transmission," in *Proc. of the European Conference on Optical Communication (ECOC)*, 2015, paper Tu.1.1.2.

[38] H. Buelow, V. Aref, and W. Idler, "Transmission of waveforms determined by 7 eigenvalues with PSK-modulated spectral amplitudes," in *Proc. of the European Conference on Optical Communication (ECOC)*, 2016, paper Tu.3.E.2.

[39] T. Gui, Z. Dong, C. Lu, P.-K. A. Wai, and A. P. T. Lau, "Phase modulation on nonlinear discrete spectrum for nonlinear frequency division multiplexed transmissions," in *Proc. of the Optical Fiber Communications Conference and Exhibition (OFC)*, 2016, paper W3A.2.

[40] S. Hari and F. R. Kschischang, "Bi-directional algorithm for computing discrete spectral amplitudes in the NFT," *Journal of Lightwave Technology*, vol. 34, no. 15, pp. 3529–3537, 2016.

[41] A. Geisler and C. G. Schaeffer, "Experimental nonlinear frequency division multiplexed transmission using eigenvalues with symmetric real part," in *Proc. of the European Conference on Optical Communication (ECOC)*, 2016, paper Th.2.P2.SC5.56.

[42] I. Tavakkolnia and M. Safari, "Signalling over nonlinear fibre-optic channels by utilizing both solitonic and radiative spectra," in *Proc. of the European Conference on Networks and Communications (EuCNC)*, 2015, pp. 103–107.

[43] V. Aref, S. T. Le, and H. Buelow, "Demonstration of fully nonlinear spectrum modulated system in the highly nonlinear optical transmission regime," in *Proc. of the European Conference on Optical Communication (ECOC)*, 2016, paper post-deadline Th.3.B.2.

[44] S. T. Le, V. Aref, and H. Buelow, "High speed pre-compensated nonlinear frequency-division multiplexed transmissions," *Journal of Lightwave Technology*, vol. PP, 2017.

[45] S. T. Le, V. Aref, and H. Buelow, "Nonlinear signal multiplexing for communication beyond the Kerr nonlinearity limit," *Nature Photonics*, vol. 2, no. July, pp. 1–8, 2017.

[46] J. E. Prilepsky, S. A. Derevyanko, K. J. Blow, I. Gabitov, and S. K. Turitsyn, "Nonlinear inverse synthesis and eigenvalue division multiplexing in optical fiber channels," *Physical Review Letters*, vol. 113, p. 013 901, 2014.

[47] S. T. Le, I. D. Phillips, Prilepsky, P. Harper, A. D. Ellis, and S. K. Turitsyn, "Demonstration of nonlinear inverse synthesis transmission over transoceanic distances," *Journal of Lightwave Technology*, vol. 34, pp. 2459–2466, 2016.

[48] S. T. Le, J. E. Prilepsky, and S. K. Turitsyn, "Nonlinear inverse synthesis technique for optical links with lumped amplification," *Optics express*, vol. 23, no. 7, pp. 8317–8328, 2015.

[49] E. G. Turitsyna and S. K. Turitsyn, "Digital signal processing based on inverse scattering transform," *Optics letters*, vol. 38, no. 20, pp. 4186–4188, 2013.

[50] S. Wahls, S. T. Le, J. E. Prilepsk, H. V. Poor, and S. K. Turitsyn, "Digital backpropagation in the nonlinear Fourier domain," in *International Workshop on Signal Processing Advances in Wireless Communications (SPAWC)*, 2015, pp. 445–449.

[51] S. Wahls, "Fiber-optic communication using fast nonlinear Fourier transforms," in *Proc. of the Optical Fiber Communication Conference (OFC)*, 2016, paper W3A.1.

[52] M. Kamalian, J. E. Prilepsky, S. T. Le, and S. K. Turitsyn, "Periodic nonlinear Fourier transform based transmissions with high order QAM formats," in *Proc. of the European Conference on Optical Communication (ECOC)*, 2016.

[53] M. Kamalian, J. E. Prilepsky, S. T. Le, and S. K. Turitsyn, "Periodic nonlinear Fourier transform for fiber-optic communications, Part I: theory and numerical methods," *Optics express*, vol. 24, no. 16, pp. 18 353–18 369, 2016.

[54] M. Kamalian, J. E. Prilepsky, S. T. Le, and S. K. Turitsyn, "Periodic nonlinear Fourier transform for fiber-optic communications, Part II: eigenvalue communication," *Optics express*, vol. 24, no. 16, pp. 18 370–18 381, 2016.

[55] Q. Zhang and T. H. Chan, "Noise models in the nonlinear spectral domain for optical fibre communications," *arXiv:1702.06226*, 2017.

[56] S. Wahls, "Second order statistics of the scattering vector defining the DT nonlinear Fourier transform," in *Proc. of the International ITG Conference on Systems, Communications and Coding (SCC)*, 2017, pp. 1–6.

[57] T. Gui, T. H. Chan, C. Lu, A. P. T. Lau, and P. K. A. Wai, "Alternative decoding methods for optical communications based on nonlinear Fourier transform," *Journal of Lightwave Technology*, vol. 35, no. 9, pp. 1542–1550, May 2017.

[58] S. Civelli, E. Forestieri, and M. Secondini, "Why noise and dispersion may seriously hamper nonlinear frequency-division multiplexing," *arXiv:1705.06779*, 2017.

[59] S. A. Derevyanko, J. E. Prilepsky, and S. K. Turitsyn, "Capacity estimates for optical transmission based on the nonlinear Fourier transform," *Nature communications*, vol. 7, p. 12 710, 2016.

[60] I. Tavakkolnia and M. Safari, "Capacity analysis of signaling on the continuous spectrum of nonlinear optical fibers," *Journal of Lightwave Technology*, vol. 35, no. 11, pp. 2086–2097, 2017.

[61] Q. Zhang and T. H. Chan, "Achievable rates of soliton communication systems," in *International Symposium on Information Theory (ISIT)*, 2016, pp. 605–609.

[62] N. A. Shevchenko, J. E. Prilepsky, S. A. Derevyanko, A. Alvarado, P. Bayvel, and S. K. Turitsyn, "A lower bound on the per soliton capacity of the nonlinear optical fibre channel," in *Information Theory Workshop-Fall (ITW)*, 2015, pp. 104–108.

[63] M. I. Yousefi, G. Kramer, and F. R. Kschischang, "Upper bound on the capacity of the nonlinear schrödinger channel," in *Canadian Workshop on Information Theory (CWIT)*, 2015, pp. 22–26.

[64] S. Sugavanam, M. Kamalian, J. Peng, J. E. Prilepsky, and S. K. Turitsyn, "Experimentally characterized nonlinear fourier transform of a mode-locked fibre laser," in *European Quantum Electronics Conference*, 2017, paper EF.2.6.

[65] A. Maruta and Y. Matsuda, "Polarization division multiplexed optical eigenvalue modulation," in *Proc. of the International Conference on Photonics in Switching (PS)*, 2015, pp. 265–267.

[66] J.-W. Goossens, M. I. Yousefi, Y. Jaouën, and H. Hafermann, "Polarization division multiplexing based on the nonlinear Fourier transform," *Optics Express*, vol. 25, no. 22, pp. 26 437–26 452, October 2017.

[67] J. G. Proakis, *Digital communications*, 5th ed. McGraw-Hill, 2012.

[68] M. J. Ablowitz, B. Prinari, and A. D. Trubatch, "Integrable nonlinear Schrödinger systems and their soliton dynamics," *Dynamics of PDE*, vol. 1, no. 3, pp. 239–299, 2004.

[69] R. G. Docksey and J. N. Elgin, "Closure of the Manakov system," *SIAM Journal on Mathematical Analysis*, vol. 32, no. 1, p. 54, 2000.

[70] A. Hasegawa and Y. Kodama, *Solitons in optical communications*, 7th ed. Oxford University Press, USA, 1995.

[71] J. E. Prilepsky, S. A. Derevyanko, and S. K. Turitsyn, "Nonlinear spectral management: Linearization of the lossless fiber channel," *Optics express*, vol. 21, no. 20, pp. 24 344–24 367, 2013.

[72] S. Desbruslais, "Inverse scattering transform for soliton transmission analysis," *Optical Fiber Technology*, vol. 2, no. 4, pp. 319–342, 1996.

[73] J. Yang, *Nonlinear Waves in Integrable and Nonintegrable Systems*. SIAM, 2010.

[74]   H. Bülow, "Experimental demonstration of optical signal detection us-
       ing nonlinear Fourier transform," *Journal of Lightwave Technology*,
       vol. 33, pp. 1433–1439, 2015.

[75]   F. Calogero, N. Ercolani, H. Flaschka, V. Marchenko, A. Mikhailov, A.
       Newell, E. Schulman, A. Shabat, E. Siggia, V. Sokolov, *et al.*, *What is
       integrability?* Springer Science & Business Media, 2012.

[76]   N. J. Hitchin, G. B. Segal, and R. S. Ward, *Integrable systems: Twistors,
       loop groups, and Riemann surfaces.* Oxford University Press, 2013.

[77]   P. D. Lax, "Integrals of nonlinear equations of evolution and solitary
       waves," *Communications on pure and applied mathematics*, vol. 21,
       no. 5, pp. 467–490, 1968.

[78]   S. Wahls, "Generation of Time-Limited Signals in the Nonlinear Fourier
       Domain via b-Modulation," in *Proc. of the European Conference on
       Optical Communications (ECOC)*, paper W.3.C.6.

[79]   M. I. Yousefi and F. R. Kschischang, "Information transmission using
       the nonlinear Fourier transform, part III: Spectrum modulation," *IEEE
       Transactions on Information Theory*, vol. 60, no. 7, pp. 4346–4369,
       2014.

[80]   V. B. Matveev and M. A. Salle, *Darboux transformations and solitons.*
       Springer-Verlag, 1991.

[81]   V. Aref, "Control and detection of discrete spectral amplitudes in non-
       linear Fourier spectrum," *arXiv:1605.06328*, 2016.

[82]   J. D. Ania-Castanón, T. J. Ellingham, R. Ibbotson, X. Chen, L. Zhang,
       and S. K. Turitsyn, "Ultralong Raman fiber lasers as virtually lossless
       optical media," *Physical Review Letters*, vol. 96, no. 2, p. 023 902, 2006.

[83]   A. Hasegawa and Y. Kodama, "Guiding-center soliton in optical fibers,"
       Optics Letters, vol. 15, no. 24, pp. 1443–1445, 1990.

[84]   S. Le, J. Prilepsky, M. Kamalian, P. Rosa, M. Tan, J. Ania-Castañón,
       P. Harper, and S. K. Turitsyn, "Modified nonlinear inverse synthesis
       for optical links with distributed Raman amplification," in *Proc. of the
       European Conference on Optical Communication (ECOC)*, 2015, paper
       Tu.1.1.3.

[85]   V. Aref and H. Buelow, "Design of 2-soliton spectral phase modulated
       pulses over lumped amplified link," in *Proc. of the European Conference
       on Optical Communication (ECOC)*, 2016.

[86]   DTU Fotonik DSP group. (2018). Robochameleon: Optical communication systems simulation framework, [Online]. Available: `http://dtu-dsp.github.io/Robochameleon/`.

[87]   M. I. Yousefi and F. R. Kschischang, "Information transmission using the nonlinear Fourier transform, part II: Numerical methods," *IEEE Transactions on Information Theory*, vol. 60, no. 7, pp. 4329–4345, 2014.

[88]   J. Armstrong, "OFDM for optical communications," *Journal of lightwave technology*, vol. 27, no. 3, pp. 189–204, 2009.

[89]   S. Hari, F. Kschischang, and M. Yousefi, "Multi-eigenvalue communication via the nonlinear Fourier transform," in *Biennial Symposium on Communications (QBSC)*, 2014, pp. 92–95.

[90]   J. E. Prilepsky, S. A. Derevyanko, K. J. Blow, I. Gabitov, and S. K. Turitsyn, "Nonlinear inverse synthesis and eigenvalue division multiplexing in optical fiber channels," *Physical Review Letters*, vol. 113, no. 1, p. 013 901, 2014.

[91]   Q. Zhang and T. H. Chan, "A Gaussian noise model of spectral amplitudes in soliton communication systems," in *International Workshop on Signal Processing Advances in Wireless Communications (SPAWC)*, 2015, pp. 455–459.

[92]   Q. Zhang and T. H. Chan, "A spectral domain noise model for optical fibre channels," in *International Symposium on Information Theory (ISIT)*, 2015, pp. 1660–1664.

[93]   V. Vaibhav and S. Wahls, "Multipoint newton-type nonlinear Fourier transform for detecting multi-solitons," in *Proc. of the Optical Fiber Communications Conference and Exhibition (OFC)*, 2016, paper W2A.34.

[94]   H. Bülow, V. Aref, K. Schuh, and W. Idler, "Experimental nonlinear frequency domain equalization of QPSK modulated 2-eigenvalue soliton," in *Proc. of the Optical Fiber Communications Conference and Exhibition (OFC)*, 2016, paper Tu2A.3.

[95]   A. Span, V. Aref, H. Bülow, and S. T. Brink, "On time-bandwidth product of multi-soliton pulses," in *Proc of the IEEE International Symposium on Information Theory (ISIT)*, 2017, pp. 61–65.

[96]   S. Wahls and H. V. Poor, "Fast inverse nonlinear Fourier transform for generating multi-solitons in optical fiber," in *International Symposium on Information Theory (ISIT)*, 2015, pp. 1676–1680.

[97] V. Vaibhav and S. Wahls, "Introducing the fast inverse NFT," in *Proc. of the Optical Fiber Communication Conference (OFC)*, 2017, paper Tu3D.2.

[98] A. Geisler and C. G. Schaeffer, "Influence of input power mismatch on time domain detection of solitonic components," in *Proc. of the ITG-Symposium on Photonic Networks*, 2017, pp. 1–4.

[99] A. Napoli, M. M. Mezghanni, S. Calabro, R. Palmer, G. Saathoff, and B. Spinnler, "Digital predistortion techniques for finite extinction ratio IQ Mach–Zehnder modulators," *Journal of Lightwave Technology*, vol. 35, no. 19, pp. 4289–4296, 2017.

[100] G. Liga, A. Alvarado, E. Agrell, M. Secondini, R. I. Killey, and P. Bayvel, "Optimum detection in presence of nonlinear distortions with memory," in *Proc. of the European Conference on Optical Communication (ECOC)*, 2015, paper P.4.13.

[101] M. I. Yousefi and X. Yangzhang, "Linear and nonlinear frequency-division multiplexing," in *Proc. of the European Conference on Optical Communication (ECOC)*, 2016.

[102] D. Qian, M.-F. Huang, E. Ip, Y.-K. Huang, Y. Shao, J. Hu, and T. Wang, "101.7-tb/s (370× 294-gb/s) PDM-128QAM-OFDM transmission over 3× 55-km SSMF using pilot-based phase noise mitigation," in *National Fiber Optic Engineers Conference*, 2011, PDPB5.

[103] A. J. Viterbi and A. M. Viterbi, "Nonlinear estimation of PSK-modulated carrier phase with application to burst digital transmission," in *The Foundations of the Digital Wireless World: Selected Works of AJ Viterbi*, World Scientific, 2010, pp. 31–39.

[104] T. Pfau, S. Hoffmann, and R. Noé, "Hardware-efficient coherent digital receiver concept with feedforward carrier recovery for *m*-QAM constellations," *Journal of Lightwave Technology*, vol. 27, no. 8, pp. 989–999, 2009.

[105] V. Aref, H. Buelow, and K. Schuh, "On spectral phase estimation of noisy solitonic transmission," in *Proc. of the Optical Fiber Communications Conference and Exhibition (OFC)*, 2016, paper W3A.3.

[106] P. K. Wai, C. R. Menyuk, and H. H. Chen, "Stability of solitons in randomly varying birefringent fibers.," *Optics letters*, vol. 16, no. 16, pp. 1231–3, 1991.

[107] S. V. Manakov, "On the theory of two-dimensional stationary self-focusing of electromagnetic waves," *Soviet Physics JETP*, vol. 38, no. 2, pp. 248–253, 1974.

[108] J. Yang, "Multisoliton perturbation theory for the Manakov equations and its applications to nonlinear optics," *Physical Review E*, vol. 59, no. 2, p. 2393, 1999.

[109] T. Lakoba and D. Kaup, "Perturbation theory for the manakov soliton and its applications to pulse propagation in randomly birefringent fibers," *Physical Review E*, vol. 56, no. 5, p. 6147, 1997.

[110] C. Xie, M. Karlsson, P. A. Andrekson, H. Sunnerud, and J. Li, "Influences of polarization-mode dispersion on soliton transmission systems," *IEEE Journal of selected topics in quantum electronics*, vol. 8, no. 3, pp. 575–590, 2002.

[111] Y. Chen and H. Haus, "Manakov solitons and polarization mode dispersion," *Chaos: An Interdisciplinary Journal of Nonlinear Science*, vol. 10, no. 3, pp. 529–538, 2000.

[112] T. P. Horikis and J. N. Elgin, "Nonlinear optics in a birefringent optical fiber," *Physical Review E*, vol. 69, no. 1, p. 016 603, 2004.

[113] S. A. Derevyanko, J. E. Prilepsky, and D. A. Yakushev, "Statistics of a noise-driven Manakov soliton," *Journal of Physics A: Mathematical and General*, vol. 39, no. 6, p. 1297, 2006.

[114] C. R. Menyuk and B. S. Marks, "Interaction of polarization mode dispersion and nonlinearity in optical fiber transmission systems," *Journal of Lightwave Technology*, vol. 24, no. 7, p. 2806, 2006.

[115] O. C. Wright, "The Darboux transformation of some Manakov systems," *Applied Mathematics Letters*, vol. 16, no. 5, pp. 647–652, 2003.

[116] N. Benvenuto and M. Zorzi, *Principles of communications Networks and Systems*. John Wiley & Sons, 2011.

[117] D. Le Khoa, N. T. Tu, N. T. H. Thu, and N. H. Phuong, "Peak-to-average power ratio reduction in long haul coherent optical OFDM systems," in *Recent Advances in Electrical Engineering and Related Sciences (AETA)*, Springer, 2014, pp. 221–228.

[118] V. Aref, H. Bülow, K. Schuh, and W. Idler, "Experimental demonstration of nonlinear frequency division multiplexed transmission," in *Proc. of the European Conference on Optical Communication (ECOC)*, 2015, paper Tu.1.1.2.

[119] T. Pfau, S. Hoffmann, and R. Noé, "Hardware-efficient coherent digital receiver concept with feedforward carrier recovery for MQAM constellations," *Journal of Lightwave Technology*, vol. 27, no. 8, pp. 989–999, April 2009.

[120] N. Nabavi and T. J. Hall, "Demultiplexing by independent component analysis in coherent optical transmission: The polarization channel alignment problem," in *Proc. of Photonics North*, 2015.

[121] K. Kikuchi, "Analyses of wavelength-and polarization-division multiplexed transmission characteristics of optical quadrature-amplitude-modulation signals," *Optics express*, vol. 19, no. 19, pp. 17 985–17 995, 2011.